Search for the Lepton Flavour Violating Decay in $\Upsilon(3S) \rightarrow e^{\pm}\mu^{\mp}$

by

Nafisa Tasneem
Master of Science, Kyungpook National University 2004
Graduate Certificate in Learning and Teaching in Higher Education,
University of Victoria 2014

A Dissertation Submitted in Partial Fulfillment of the
Requirements for the Degree of

DOCTOR OF PHILOSOPHY

in the Department of Physics and Astronomy

Search for the Lepton Flavour Violating Decay in $\Upsilon(3S) \rightarrow e^{\pm}\mu^{\mp}$

by

Nafisa Tasneem
Master of Science, Kyungpook National University 2004
Graduate Certificate in Learning and Teaching in Higher Education,
University of Victoria 2014

Supervisory Committee

Dr. J. Michael Roney, Supervisor,
(Department of Physics and Astronomy)

Dr. R. V. Kowalewski, Departmental Member,
(Department of Physics and Astronomy)

Dr. Alexandre Brolo, Committee Member,
(Department of Chemistry)

ABSTRACT

Charged lepton flavour violating processes are highly suppressed in the standard model, but they are predicted to be enhanced in several new physics extensions including supersymmetry and models with leptoquarks or compositeness. Data collected with the BaBar detector at the SLAC PEP-II e^+e^- asymmetric collider at a centre-of-mass energy of 10.36 GeV were used to search for electron-muon flavor violation in $\Upsilon(3S) \to e^{\pm}\mu^{\pm}$ decays. The search was conducted using a data sample in which 118 million $\Upsilon(3S)$ mesons were produced, corresponding to an integrated luminosity of 27 fb^{-1}. There is no evidence of a signal in the $\Upsilon(3S)$ data and we report our results as upper limits on $\mathcal{B}(\Upsilon(3S) \to e^{\pm}\mu^{\mp}) < 3.6 \times 10^{-7}$at 90% CL.

Contents

List of Tables

List of Figures

ACKNOWLEDGEMENTS

This thesis summarizes my work from the last couple of years. This work would not have been possible without the help of many people. A lot of support came from the people that worked with directly, but also from people I met during those years and with which I shared my life.

At first, I must thank my advisor, Prof. M. Roney, who gave me the opportunity to do this work, to join the BABAR UVic group, to allow visit at SLAC frequently. He should be also credited with helping improve my skills not only as a physicist, but even in the everyday working life. Through him, I was introduced to the people of BABAR group. I would like to thank everyone for their kind support and advices.

Then I have to thank all the people from the BABAR Collaboration and especially from Tau/QED analysis working group. A special mention is for Physics Analysis Coordinator Dr. Fabio Anulli, Deputy Coordinator Dr. Frank Porter and Physics Coordinator Emeritus Dr. Abi Soffer who provided contributions for this work by providing their valuable comments on my research. Another mention is for all the people who reviewed this work, from the first stages until the final steps before publication and also the people who acted as referees for this thesis. Another mention is for the people working for SLAC administration specially Computing Coordinator Tina Cartaro; their support was always essential. The last mention is for the people working for UVic BaBar group Dr. Hossain Ahmed, Dr. Gregory King, Beaulieu, Alexandre, Dr. Ian Nugent. I would also like to thank BaBar's internal Review Committee members Dr. Banerjee Swagato, Dr. Muller David Robert, and Dr. Robertson Steven H.(Chair). Their seamless effort made this analysis well supported.

Regarding the people I have met and share my time during those years from around the world including my family members and friends, who may not directly involved in this work, but their support was invaluable. I would say only that everyone I met along the way, they are going to change me, either for good or bad, but their legacy is what I am right now. I hope I will get the appropiate time and mood sometime to say thanks!.

Nafisa Tasneem

DEDICATION

To my beloved husband Dr. Hossain Ahmed and our two lovely daughters Ispeeta Ahmed and Wafeeqa Ahmed!

Chapter 1

Introduction

The Standard Model (SM) of fundamental interactions has proven to be one of most precisely verified physical theories of all times. Even though the SM has had years of experimental success, it is not the ultimate theory of everything. For example, it does not incorporate gravity, has no explanation for Dark Matter, and can not explain why the universe is composed of only matter and no antimatter.

One of the fundamental sets of particles in nature are the leptons which come in three flavours: electron, muon, or tau. For some reason, we generally only see reactions that conserve lepton flavour: when an electron (e^-) is created it must be accompanied by either its antiparticle, the positron (e^+), or the antiparticle of an electron-type neutrino ($\bar{\nu_e}$). Similarly for muon and tau leptons, which are heavier versions of the electron. This observation is inserted in the SM and called lepton flavour conservation. This general rule is violated when neutrinos mix with each other, a phenomenon which had been established early in the 21st century [1], [2] and which has been included in a new version of the SM. But to observe the violation of the rule for charged leptons would require a serious violation of the SM that is not easily accomodated, which clearly suggested that new physics would be required.

So when an $\Upsilon(3S)$ or $\Upsilon(2S)$ meson particle (which is made of a b-quark and anti-b-quark pair) decays, the SM says that it can go into an electron-positron pair (e^+e^-), or a pair of oppositely charge muons ($\mu^+\mu^-$), or tau leptons ($\tau^+\tau^-$). But it cannot decay into an electron and muon ($e^+\mu^-$), or muon and tau ($\mu^+\tau^-$) or electron and tau ($e^+\tau^-$). BaBar published several papers reporting on searches for some of those forbidden decays specifically $\Upsilon(3S) \to e\tau$ and $\Upsilon(3S) \to \mu\tau$. As it turns out, the experiment finds no evidence for anything that cannot be understood within the SM framework. However, BaBar did set impressive new limits as described in the

Table A.1.

Table 1.1: CLEO and BaBar results on different decay modes of $\Upsilon(3S)$.

Experiments	**Measurements**	**Results**	**CL** (%)
CLEO [3]	$BF(\Upsilon(1S) \to \mu^{\pm}\tau^{\pm})$	$< 6 \times 10^{-6}$	95
CLEO [3]	$BF(\Upsilon(2S) \to \mu^{\pm}\tau^{\pm})$	$< 14.4 \times 10^{-6}$	95
CLEO [3]	$BF(\Upsilon(3S) \to \mu^{\pm}\tau^{\pm})$	$< 20.3 \times 10^{-6}$	95
BaBar [4]	$BF(\Upsilon(3S) \to e^{\pm}\tau^{\pm})$	$< 5 \times 10^{-6}$	90
BaBar [4]	$BF(\Upsilon(3S) \to \mu^{\pm}\tau^{\pm})$	$< 4.1 \times 10^{-6}$	90

Evidence for such new physics can be seen in the direct production and observation of new particles, by increasing the beam energy above the production threshold, but also by looking for the effects of these new particles in loop diagrams, by precision measurements performed at high luminosity machines. This places strict constraints on certain types of theories that predict such lepton flavour violating (LFV) processes. For example, in a theory that introduces a new particle that, through quantum loops, induces these forbidden decays, the mass scale of the new particle must be above around 1000 GeV, which is the same sort of mass scale probed in a different and complementary manner at the LHC.

In this thesis, the BaBar detector at SLAC is used to search for the lepton flavour violating process in the decays of $\Upsilon(3S) \to e^{\pm}\mu^{\mp}$ collected at a center of mass energy $\sqrt{s} = 10.3552$ GeV in the PEP-II storage ring. Key experimental measurements are shown in the Table 1.2 regarding $e^{\pm}\mu^{\mp}$ search in vector bosons. However, no experimental branching fraction has yet published for the the decay $\Upsilon(3S) \to e^{\pm}\mu^{\mp}$.

Table 1.2: A sample of the most stringent experimental limits on vector boson decay to $e^{\pm}\mu^{\mp}$.

Measurements	**Results**	**CL** (%)
$BR(\phi \to e^{\pm}\mu^{\mp})$ [5]	$< 2.0 \times 10^{-6}$	90
$BR(J/\Psi \to e^{\pm}\mu^{\mp})$ [6]	$< 1.6 \times 10^{-7}$	90
$BR(Z^0 \to e^{\pm}\mu^{\mp})$ [7]	$< 7.5 \times 10^{-7}$	95

1.1 Other activities performed during Ph.D. period

During the Ph.D. period, aside from the analysis activity described in this thesis, I have also taken part in other activities on behalf of the UVic BaBar group as taking part in SuperB testbeam at TRIUMF. I was involved in another analysis which was intended to measure "Leptonic Forward Backward Asymmetry". The production of muon pairs in the process $e^+e^- \rightarrow \mu^+\mu^-$ is sensitive to the axial vector part of the weak neutral current through coupling and to the effects of higher order QED processes. As a result there exists an asymmetric contribution to the angular distribution of final state particles. This asymmetry can be a significant tool to test the validity of the SM in a precision level. However my detailed systematic studies showed the forward backward asymmetry measurement was dominated by the detector response effects rather than the interesting physics process involved. The project "Leptonic Forward Backward Asymmetry" helped me tremendously for completing the current project and write my dissertation. Through my previous project I learnt the BaBar basic framework such as how to use Long Term Data Analysis (LTDA) facility and to handle BaBar Data, software and Monte carlo productions. The previous project introduced several concepts that became very useful for running the current physics analyses.

Chapter 2

Motivation and Theoretical Background

Humankind has searched long for measuring many fundamental questions in nature such as where do we come from? Where are we? and where are we going? Even in the ancient times, peoples sought to organize the world around them into fundamental elements, e.g. earth, air, fire, and water. It is more than a century since physicists have discovered the atom. Based on their atomic number (number of protons), electron configurations, and the chemical properties atoms are classified in a tabular arrangement called the "periodic table". During the 20th century, physicists were able to see inside the atom by breaking it apart with the experiments. They conclude that the atom is mostly "empty" consisting of very light negative charged particles (electrons) surrounding a heavy positive nucleus (combined the neutral neutrons and charged protons together). Problems arose in the middle of the 20th century when physicists discovered many other particles in particle accelerators and cosmic rays, e.g. muon, pion, kion, lambda, delta, sigma, rho, omega etc. The quark model [8] provided an organization of all the known particles and it is known as the birth of the SM. Based on decreasing size, the current hierarchy of the structure of matter is in the sequence as shown in Figure 2.1: atoms $\rightarrow$ nuclei $\rightarrow$ nucleons $\rightarrow$ quarks.

2.1 The Standard Model

With the discovery of the "Higgs Boson" by the ATLAS [9] and CMS [10] experiments at the Large Hadron Collider (LHC) at CERN [11], the SM, got further credence as

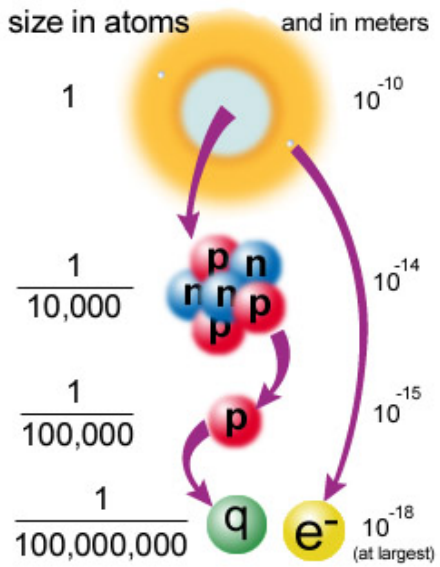

Figure 2.1: Hierarchy of the structure of matter

.

a very successful particle theory. The SM explained in detail in many textbooks [12], [18], [19], [20], (resulting from an immense experimental and theoretical inspired effort over the last several decades) explains the elementary particles and the interactions among them except the gravitational interaction which has negligible effect on elementary particles at currently accessible scales. According to this model, all matter is made up of fundamental spin 1/2 particles, or fermions: six leptons and six quarks interacting through fields, of which they are the sources. The particles associated with the interaction fields are spin-1 bosons.

2.1.1 Leptons

The lepton properties for integral electric charged particles are given in the Table 2.1. The Dirac equation for a charged massive fermion predicts, correctly, the existence of an antiparticle of the same mass and spin, but opposite charge, and opposite magnetic moment relative to the direction of the spin.

Of the charged leptons, only the electron (e^-) carrying charge -e and its antiparticle positron (e^+), are stable. In other words, lepton in the SM is structureless point particle and one of the fundamental building blocks of matter. The muon (μ^-) and tau (τ^-) and their antiparticles, (μ^+) and (τ^+), differ from the electron and positron

Table 2.1: Basic properties of leptons. The particles are grouped according to generation [21].

Lepton	**Charge** (e)	**Mass** (MeV/c^2)
Electron (e)	-1	$0.5109989461 \pm 0.000000031$
Electron Neutrino (ν_e)	0	$< 2 \times 10^{-6}$
Muon (μ)	-1	$105.6583745 \pm 0.0000024$
Muon Neutrino (ν_μ)	0	$< 2 \times 10^{-6}$
Tau (τ)	-1	1776.86 ± 0.12
Tau Neutrino (ν_τ)	0	$< 2 \times 10^{-6}$

only in their masses and their finite lifetimes. They appear to be elementary particles.

2.1.2 Quarks

The properties of the quarks are listed in the Table 2.2. In the SM, quarks, like leptons, are spin 1/2 Dirac fermions, but the electric charges they carry are +2/3 e, -1/3 e. Due to the phenomenon called colour confinement quarks are never directly observed or found in isolation; they can be found only within hadrons, such as baryons (e.g. protons, neutrons etc.) and mesons (e.g. pion, kion etc.). The net quark number of an isolated system has never been observed to change. However, the number of different types of "flavours" of quark are not separately conserved: changes are possible through the weak interaction.

Table 2.2: Basic properties of quarks. The particles are grouped according to generation [21].

Quarks	**Charge** (e)	**Mass** (GeV/c^2)
Up (u)	+ 2/3	$0.0022^{+0.6}_{-0.4}$
Down (d)	- 1/3	$0.0047^{+0.5}_{-0.4}$
Charm (c)	+ 2/3	1.27 ± 0.03
Strange (s)	- 1/3	0.096^{+8}_{-4}
Top (t)	- 1/3	$173.21 \pm 0.51 \pm 0.71$
Bottom (b)	+ 2/3	$4.18^{+0.04}_{-0.03}$

The proton basically contains two up quarks and one down quark (uud), and the

neutron two down quarks and one up (udd) as well as the gluons which bind the quark in the proton and neutron. The proton is the only stable baryon. The neutron is a little more massive than the proton and in free space it decays to a proton through the weak interaction: $n \rightarrow p + e^- + \bar{\nu_e}$, with a mean life of about 15 minutes. All mesons are unstable and the lightest mesons are pions.

2.1.3 Interactions

We have looked at the particles in the Tables 2.1 and 2.2; in addition to leptons and quarks the SM also comprises their interactions. Different interactions are described in quantum language in terms of the force carriers, called "bosons" given in the Table 2.3.

Table 2.3: Basic properties of mediators [21].

Mediator	**Charge**(e)	**Mass** (GeV/c^2)	**Interaction**
Photon (γ)	0	0	Electromagnetic
$W^{\pm}$	± 1	80.385 ± 0.015	Weak
Z^0	0	91.1876 ± 0.0021	Weak
Gluon (g)	0	0	Strong
Graviton (G)	0	0	Gravitational

The theory of quantum electrodynamics (QED), which is formed by quantizing the theory of classical electrodynamics, is based on the electromagnetic interaction. The electromagnetic interactions are responsible for virtually all the phenomena in extra-nuclear physics, in particular for the bound states of electrons with nuclei, i.e. atoms and molecules, and for the intermolecular forces in liquids and solids. These interactions are mediated by photon exchange.

The theory of weak interactions (sometimes called quantum flavour-dynamics) explains how the elementary particles are weakly interacting and the interactions are mediated by massive intermediate vector bosons. This is a unique interaction where the particles are capable of changing their flavours and which violates some symmetries, e.g. parity and charge-parity. In the sixties in 20th century, the electromagnetic and weak interactions were unified in a single electroweak theory by Glashow [22], Weinberg [23], and Salam [24], employing the Higgs mechanism of spontaneous symmetry breaking.

The strong interaction is responsible for binding the quarks in the neutron and proton, and the neutrons and protons within nuclei. The theory of quantum chromodynamics (QCD) describes the interactions between quarks and gluons, which has two distinct features: asymptotic freedom and confinement. Confinement (often called colour confinement) is the physics phenomenon that colour charged particles (such as quarks and gluons) cannot be isolated, and therefore cannot be directly observed. Asymptotic freedom means that the strength of the interaction decreases with increasing energy corresponding a decreased distance.

Gravitational interactions act between all types of particles. On the scale of experiments in particle theory, gravity is by far the weakest of all the fundamental interactions, although of course it is dominant on the scale of the universe. It is supposedly mediated by exchange of a spin 2 boson, the graviton, which is yet to be understood better. It is not embedded in the SM.

2.2 Challenges to the Standard Model

Despite being the most successful theory of particle physics to date, the SM still has a number of deficiencies and unexplained features, e.g.:

- Neutrino masses and mixings: neutrinos are massless in the SM frame, however neutrino oscillation experiments have shown that neutrinos do have mass [25];
- Dark matter and dark energy: Astrophysical measurements of the rotations of galaxies indicate that normal baryonic matter makes up only about 4.9 % of the total energy density of the Universe and rest are dark matter (26.8 %) and dark energy (68.3 %) [26]. Many physics models and astronomical observations [27], [28] predict the dark sector that might be a family of particles and forces. The new gauge bosons are mediating interactions between "dark sector" and the SM. The known SM particles and interactions are insufficient to explain the dark matter. BaBar has a significant role to search for "dark sector" [29], [30], [31], [32];
- In the SM, the strong and electroweak interactions are not unified;
- Why is the world we observe made up almost entirely of matter, while it is expected that equal quantities of matter and antimatter were produced in the Big Bang?;

- Hierarchy problem: why the natural scale of gravity 10^{19} GeV is much larger than the electroweak scale 10^2 GeV;
- SM does not explain gravity;
- Are there any other generations of elementary particles?
- The model has 19 free parameters, such as particle masses (plus neutrino masses) which cannot be independently calculated using the model itself;

Most of these outstanding issues require a BSM theory, which could be the extension of the original frame and brought to us the new physics.

2.3 Symmetry in Standard Model

A symmetry is an operation that leaves a system in a configuration which is indistinguishable from the system's original configuration. For example an equilateral triangle brought under to rotation by 120° about its center, reflecting the triangle through a line joining one of its vertices to the midpoint of the opposite side, it would seem no change has done at all to the triangle. "Doing nothing" at all to a system leaves it in a state indistinguishable from the original is technically a symmetry. Symmetries do not need to be visual, geometric symmetries, any abstract operation that meets the criterion given above is a symmetry.

Noether's theorem, proved in 1915, is a cornerstone of modern theoretical physics. It states that any differentiable symmetry of the action[1] of a physical system has a corresponding conservation law. In other words, every symmetry implies a conserved quantity, and every conserved quantity reveals an underlying symmetry [33]. Conserved quantities, of course, are quantities that are unchanged by transformations of a system. Such quantities include energy, momentum, and electric charge etc. To continue our example, the translational symmetry of Newtonian mechanics corresponds to the law of conservation of momentum.

The SM possesses a number of symmetries. Among them are: symmetry with respect to translation in time, which corresponds to the conservation of energy, symmetry with respect to translation in space, which corresponds to the conservation of momentum, and symmetry with respect to rotation about a point, which corresponds

[1]The action is the integral over time of a system's Lagrangian function.

to the conservation of angular momentum. The SM also possesses symmetry with respect to gauge transformations. In electrodynamics a gauge transformation adds the gradient of an arbitrary function f to the magnetic vector potential while subtracting the partial derivative of f with respect to time from the electric scalar potential:

$$A \rightarrow A + \triangle f \tag{2.1}$$

$$\phi \rightarrow \phi - \frac{\partial f}{\partial t} \tag{2.2}$$

This is an extension of the idea that only differences in potential energy have physical significance. Electrodynamic gauge symmetry corresponds to the conservation of electric charge. The other fundamental forces described by the Standard Model, namely the strong and weak nuclear forces, also possess gauge symmetry, corresponding to the conservation of color charge and weak isospin respectively[2]

Since the Standard Model describes elementary particles in terms of relativistic quantum fields, it possesses symmetry with respect to Lorentz boosts as required by the special theory of relativity. A boost is the operation of moving from one inertial coordinate system[3] to another, and boosts are described mathematically by Lorentz transformations, which are rotations of Minkowski spacetime[4] about the origin. Because of this, Lorentz transformations encompass rotations about the origin in three-dimensional Euclidean space. Now, moving from one inertial system to another may involve a translation of the spacetime origin in addition to a rotation about that origin, so the complete relativistic symmetry is a symmetry with respect to translations (in space and time) and Lorentz rotations. This symmetry, called Poincarè symmetry, corresponds to the relativistic versions of the conservation of energy, momentum, and angular momentum.

Julian Schwinger and other scientists, in the early 1950s showed that the relativistic quantum field theories actually describe nature possess symmetry with respect to the following combined operation: charge conjugation C, which replaces a particle

[2]Like electric charge, these quantities are quantum numbers, and just as a particle which has electric charge participates in electromagnetic interactions by emitting and absorbing photons, so do particles with color charge and weak isospin participate in the strong and weak interactions. In the former case the particles emit and absorb gluons; in the later case they emit and absorb W and Z bosons.

[3]An inertial system in one in which Newton's first law is valid, and any two inertial systems move at a constant velocity with respect to one another.

[4]This is the four-dimensional coordinate system in which the special theory of relativity is set.

with its antiparticle, inversion of spatial coordinates P, and time reversal T. Actually, the electromagnetic and strong interactions are symmetric with respect to C, P, and T separately, and they are said to conserve C-parity, parity, and T-parity, respectively. The weak interaction, however, has been shown experimentally to violate C-parity conservation and parity conservation, as well as the product of parities which would be conserved by the combined operation CP. Therefore, the weak interaction is only symmetric with respect to the combined operation CPT.

The SM also possesses symmetry arising from the fact that the fields describing the elementary fermions may be shifted by an arbitrary phase angle $\phi \rightarrow e^{i\alpha}\phi$ without changing the resulting physics. Four such phase shifts are possible: all quark fields may be shifted by the same phase; the electron and its neutrino may be shifted by some different phase; and the muon with its neutrino and the τ with its neutrino may likewise be shifted. These four symmetries correspond to the conservation of baryon number B, electron number L_e, muon number L_μ and τ number L_τ. Since L_e, L_μ and L_τ are separately conserved, their sum, lepton number L, is also conserved.

The symmetries with respect to phase shift are called accidental symmetries of the Standard Model because they were not explicitly postulated at the outset of its construction, and there is no compelling physical reason for these numbers to be conserved by nature. Experimentally, the phenomenon of neutrino oscillation [13] shows that the lepton flavor numbers are not in fact conserved by nature. Theoretically, even within the Standard Model non-perturbative quantum effects[5] violate all of these accidental symmetries, leaving only the combination $B - L$ inviolate. Table 2.4 showed the symmetries of SM and their corresponding conservation laws..

2.4 Lepton Flavour Violation

The conservation of lepton number is one of the accidental symmetries of the Standard Model. If we assign lepton number L = +1 to leptons, L = -1 to antileptons, and L = 0 to all other particles we find that the net lepton number of all particles going into an interaction equals the net lepton number of all particles coming out of the interaction. In other words the net lepton number of the system is unchanged by the interaction. For example, neutron beta decay can be understood in terms of the following weak interaction:

[5]These are effects not described in terms of particle exchange.

Table 2.4: Symmetries of the Standard Model and their corresponding conservation laws.

Symmetry	**Conserved Quantity**
Spacetime translations and boosts	Energy Momentum Angular momentum
Gauge transformations	Electric charge Colour charge 3rd comp. of weak isospin
Charge conjugation C Spatial inversion P Time reversal T	C-parity (strong, EM) Parity (strong, EM) T-parity (strong, EM)
Fermion phase	Baryon number Electron number Muon number τ number

$$d \rightarrow u + e^- + \bar{\nu}_e \tag{2.3}$$

One of the neutron's d quarks (L = 0) turns into a u quark (L = 0) by emitting a W^- boson (L = 0), which in turn decays into an electron (L = +1) and an electron antineutrino (L = -1). The net lepton number is zero before and after the interaction. As another example, consider the antineutrinos produced by the decay of negatively charged pions: $\pi^- \rightarrow \mu^- + \bar{\nu}_\mu$. The pion consists of a u antiquark bound to a d quark, which annihilate one another. This annihilation produces a W^- boson that quickly decays into a muon and a muon antineutrino, so in terms of elementary particles the interaction is

$$\bar{u} + d \rightarrow \mu^- + \bar{\nu}_\mu \tag{2.4}$$

Again lepton number is conserved (0+0 = 1-1). If the muon antineutrinos are now directed at a target of protons, the following reaction occurs:

$$\bar{\nu_\mu} + p \rightarrow \mu^+ + n \tag{2.5}$$

Or in terms of elementary particles as shown in the Figure 2.2:

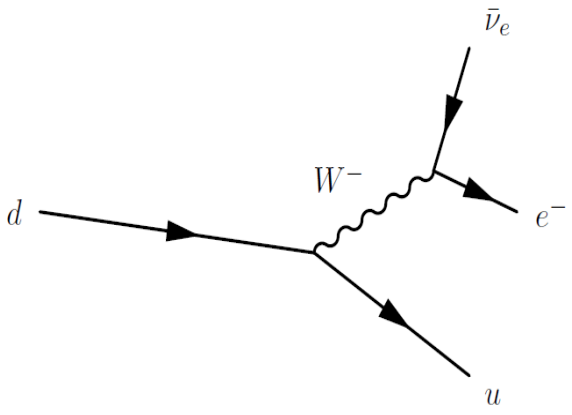

Figure 2.2: The fundamental interaction behind neutron beta decay.

.

$$\bar{\nu_\mu} + u \rightarrow \mu^+ + d \tag{2.6}$$

The muon antineutrino and one of the proton's u quark exchange a W boson and become an antimuon and d quark in the process. The d quark remains bound to the original proton's other two quarks, and a neutron results. Once again, lepton number is conserved (-1 + 0 = -1 + 0). Lepton number would also be conserved by this interaction:

$$\bar{\nu_\mu} + u \rightarrow e^+ + d \tag{2.7}$$

The only difference is that a positron[6] (L = -1) has been substituted for the antimuon (L = -1). However, no experiment to date has observed this.

If instead of decaying pions we use decaying neutrons as the source of antineutrinos, then positrons are always produced and antimuon has never observed:

$$n \rightarrow p + e^- + \bar{\nu}_e \tag{2.8}$$

$$\bar{\nu_e} + p \rightarrow e^+ + n \tag{2.9}$$

It appears that the antineutrinos are somehow associated with the particular type of charged lepton involved in their production. Finally, we note that the following charged lepton decays have never been observed:

$$\mu^- \rightarrow e^- + \gamma \tag{2.10}$$

$$\tau^- \rightarrow e^- + \gamma \tag{2.11}$$

$$\tau^- \rightarrow \mu^- + \gamma \tag{2.12}$$

We conclude that lepton number is separately conserved for each of the three charged-neutral lepton pairs[7]: e^- with ν_e, μ^- with ν_μ, and τ^- with ν_τ. To all elementary particles we assign a quantum number called electron number (L_e) with $L_e = +1$ for electrons and electron neutrinos, $L_e = -1$ for antielectrons and electron antineu-

[6]Positrons are antielectrons. The name is kept for historical reasons.

[7]The pairs are sometimes called lepton families or generations.

trinos, and $L_e = 0$ for all other particles. Muon number (L_μ) and τ number (L_τ) are similarly defined. Collectively L_e, L_μ, and L_τ are called lepton flavour numbers or simply lepton flavour, and we say that lepton flavour is conserved by all particle interactions.

Lepton flavour conservation allows us to understand why the following interaction has never been observed:

$$\bar{\nu_\mu} + u \rightarrow e^+ + d \tag{2.13}$$

Before the interaction we have $L_e = 0$, $L_\mu = -1$, and $L_\tau = 0$; afterward we have $L_e = -1$, $L_\mu = 0$, and $L_\tau = 0$. Both the conservation of electron number and the conservation of muon number have been violated. The neutrinoless decays of charged leptons, which were mentioned above, also violate lepton flavour conservation:

$$l \rightarrow l^{'} + \gamma \tag{2.14}$$

Here l and $l^{'}$ represent any two charged leptons (or charged antileptons for that matter) of differing flavour.

As shorthand we define lepton flavour violation (LFV) to be the non-conservation of lepton flavour number by an interaction. Following are the examples of lepton flavour violation[8] as shown in Figure 2.3.

$$\phi \rightarrow e^- + \mu^+ \tag{2.15}$$

$$\Upsilon \rightarrow \mu^- + \tau^+ \tag{2.16}$$

$$q\bar{q} \rightarrow l + \bar{l}^{'} \tag{2.17}$$

Where the last interaction is general and q represents any quark[9]

Although no experiment has observed LFV, there is no fundamental reason why it should not occur. The subject of the analysis described in this dissertation is a search for lepton flavour violation in decays of Υ mesons. We are looking for $\Upsilon(3S) \rightarrow e^{\pm}\mu^{\mp}$.

[8]Again we could equally well discuss the charge-conjugate interactions, where all particles are replaced with their corresponding antiparticles.

[9]Except for the t quark, which is so short-lived that it cannot bind into mesons. In this case we should write $t + \bar{t} \rightarrow l + \bar{l}^{'}$, $\bar{q}$ its antiquark, l a charged lepton, and $l^{'}$ a charged antilepton of differing flavour.

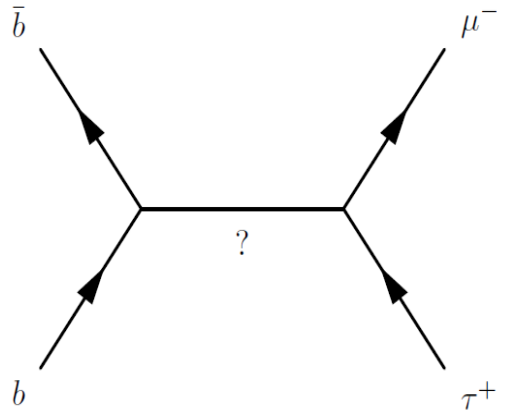

Figure 2.3: A lepton flavour violating decay. The details of the interaction are unknown and not part of the SM.

The Υ is a composite particle made of a bound state of b quark and a b antiquark. The quarks have their spins aligned, so the Υ has a spin quantum number of 1. Mass of Υ(3S) particle is measured [34] 10.355 GeV and the width of its resonance is Γ = 26.3 keV. The ratio of the partial width for a particular decay to the width of the resonance is the probability that a given particle will decay according to the particular decay mode.

With our statistics we do not expect to see lepton flavour violation in decays of Υ(4S) mesons because the Υ(4S) resonance is above the energy threshold for the production of pairs of B mesons[10]. Therefore, it decays into pairs of B mesons almost 100 % of the time[11]. Thus we use Υ(4S) data to estimate the background events in our analysis.

2.5 Overview of Theoretical Models that allow LFV Interactions

In this section we will give a brief overview of various theoretical models that allow for CLFV such as Higgs models, Super-symmetric extension of Standard Model etc.

[10]A B meson consists of a b quark bound to some other kind of quark. The lightest B meson is the B^-, which consists of a b quark bound to a u antiquark. Its mass is 5.279 MeV, and twice this falls just shy of the mass of the Υ(4S).

[11]The partial width for $\Upsilon(4S) \to e^- e^+$ is already small compared to the width of the Υ(4S), and the partial width for lepton flavour violation, $\Gamma(e^{\pm}\mu^{\mp})$, has to be smaller still.

These processes go as $\frac{g_{NP}^2}{\Lambda_{NP}^2}$ of new physics, where g_{NP}^2 is the coupling of the new physics and Λ_{NP}^2 is the energy scale of the NP, given by the mass of the NP propagator.

2.5.1 Higgs Models

A group of non-super-symmetric models that include LFV processes are Little Higgs models. One of the most attractive is the Littlest Higgs Model [14] with T-parity (LHT). The model is based on a two-stage spontaneous symmetry breaking occurring at the scale $f \geq 500$ GeV and the electroweak scale v. The additional introduced gauge bosons, fermions and scalars are sufficiently light enough to be discovered at Large Hadron Collider (LHC) and this models include also a dark matter candidate. While the models without T-parity show results close to the Standard Model (SM) predictions, a very different situation is expected in the LHT model, where the presence of new flavour violating interactions and mirror leptons with masses of order 1TeV can change the SM expectations by up to 45 orders of magnitude, bringing the relevant branching fractions for LFV processes close to the bounds available presently or in the near future.

While the possible enhancements of LFV branching fractions in the LHT model are interesting, such effects are common in many other new physics models, such as the minimal super-symmetric SM, and therefore cannot be used to distinguish between them. However correlations between various branching fractions should allow a clear distinction of the LHT model from the minimal super-symmetric SM (MSSM). Any difference between these ratios of branching fractions (BFs) from the predictions of the MSSM or the LHT model could confirm one model and exclude the other one.

2.5.2 Super Symmetric Extension of Standard Model

In the low energy Super Symmetric (SUSY) extensions of the SM the flavour and CP-violating (CPV) interactions would originate from the misalignment between fermion and sfermion mass eigenstates. Understanding why all these processes are strongly suppressed is one of the major problems of low energy SUSY. The absence of deviations from the SM predictions in LFV and CPV (and other flavour changing processes in the quark sector) experiments suggests the presence of a small amount of fermion-sfermion misalignment.

Assuming a see-saw mechanism with three heavy right-handed neutrinos, the effective light-neutrino mass matrix and its misalignment depend on Yukawa couplings

between left- and right-handed neutrinos, the latter being a potentially large source of LFV. A complete determination of LFV interactions magnitude would require a complete knowledge of the neutrino Yukawa matrix which is not possible using only low-energy observables from the neutrino sector. This is in contrast with the quark sector, where Yukawa couplings are completely determined in terms of quark masses and CKM matrix elements. As a result, the predictions of flavour changing neutral current effects in the lepton sector usually have sizable uncertainties. Making assumptions on neutrino mass matrices, we can reduce the number of free parameters and estimate some BFs for LFV decays.

2.5.3 Super Symmetric Grand Unified Theories

Other predictions for LFV processes can be obtained by embedding the SUSY model within a Grand Unified Theory (GUT), such as minimal SU(5), which incorporate the triplet see-saw mechanism. Using a minimal SU(5) GUT, a very predictive scenario can be obtained with only three free parameters: the triplet mass M_T , the effective SUSY breaking scale B_T and the coupling constant λ [15]. The phenomenological predictions more important and relevant for LHC, the B-factories, the incoming MEG experiment or the forecast Super Flavour factory, concern the sparticle and Higgs boson spectra and the LFV decays.

2.5.4 Higgs-Mediated LFV in Super-Symmetry

An independent (and potentially large) class of LFV contributions to rare decays comes also from the Higgs sector: if the slepton mass matrices have LFV entries and the effective Yukawa interaction includes non-holomorphic couplings, Higgs-mediated LFV amplitudes are necessarily induced [16]. Interestingly enough, gauge and Higgs-mediated LFV amplitudes lead to very different correlations among LFV processes.

SM extensions containing more than one Higgs doublet generally allow flavor-violating couplings of the neutral Higgs bosons with fermions. Such couplings, if unsuppressed, will lead to large flavor-changing neutral currents in direct opposition to experiments. The possible solution to this problem involves an assumption about the Yukawa structure of the model. A discrete symmetry can be invoked to allow a given fermion type to couple to a single Higgs doublet, and in such a case flavour changing neutral currents are absent at tree level.

2.5.5 Leptoquarks Model

Leptoquarks are hypothetical particles that carry information between quarks and leptons of a given generation that allow quarks and leptons to interact. They are colour-triplet bosons that carry both lepton and baryon numbers. They are encountered in various extensions of the Standard Model, such as technicolour theories or GUTs based on PatiSalam model [17], SU(5) etc. Leptoquarks, predicted to be nearly as heavy as an atom of lead, could only be created at high energies, and would decay rapidly. A leptoquark, for example, might decay into a bottom and antibottom quark and then decayed to an electon and muon lepton as shown in the Figure 2.4.

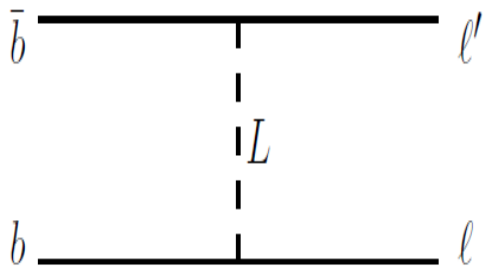

Figure 2.4: BSM processes mediating lepton flavour violating decays of the Υ to two charged leptons of different flavour, process is mediated by the exchange of a leptoquark L, a particle postulated in Grand Unified Theories which couples to both quarks and leptons.

2.5.6 Other Viable BSM scenarios

In addition to the models that we discussed earlier, many other viable beyond-the-Standard Model (BSM) scenarios predict potentially large rates for different processes as shown in Figure 2.5, which would therefore give a clear signal of new physics.

2.6 Prior Constraints

The probability that a given particle will decay according to a particular decay mode is given by the branching fraction (BF) of the decay. One of the primary concerns of experimental particle physics is the determination of branching fractions, and this

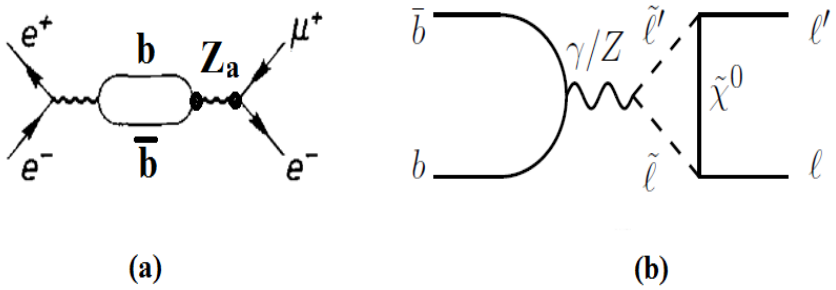

Figure 2.5: BSM processes mediating lepton flavour violating decays of the Υ to two charged leptons of different flavour, process (a) is mediated by an anomalous Z or heavy cousin of the Z denoted Z_a; while processes (b) is mediated by loops containing Supersymmetric particles.

analysis in particular seeks to measure the BF of $\Upsilon(3S) \rightarrow e^{\pm}\mu^{\mp}$, the probability that a single Υ meson will decay into a muon and an electron as shown in Figure 2.6. Prior to this direct experimental search, theoretical estimates of the upper limit on this branching fraction have been made using the experimental results on searches for $\mu \rightarrow 3e$.

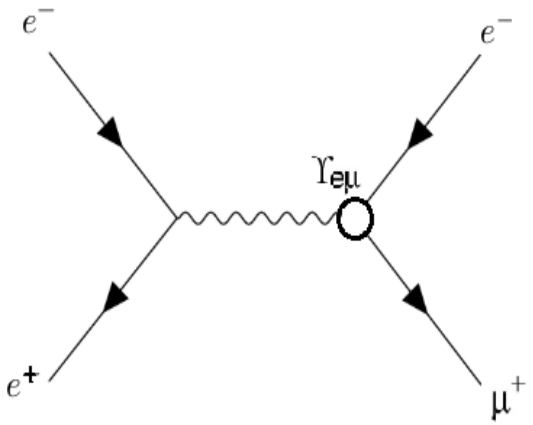

Figure 2.6: A direct search for lepton flavour Violation in $\Upsilon(3S) \rightarrow e^{\pm}\mu^{\mp}$.

Theoretical constraints on the Υ LFV decay branching fractions can be derived using an argument based on unitarity considerations. As shown in Figure 2.6, the diagram mediating the process $e^+e^- \rightarrow \Upsilon \rightarrow e^{\pm}\mu^{\mp}$ is related to the diagram mediating $\mu^- \rightarrow e^+e^-e^-$ via reordering of input and output lines. If the Υ couples to $e\mu$, then by exchange it must contribute to the decay $\mu^- \rightarrow e^+e^-e^-$. Let us write the effective

coupling between the vector boson V_i (here V_i could be either a fundamental state, such as Z^0, or a quark-antiquark bound state such as J/ψ or Υ) and $e^{\pm}\mu^{\mp}$ as

$$L_{eff} = gV_{e\mu}\bar{\mu}\gamma_{\alpha}eV^{\alpha} + h.c. \tag{2.18}$$

The coupling g, through the diagram of Figure 2.7 (left side) contributes to an amplitude term A ($\mu \rightarrow 3e$) as equation 2.19. Comparing the contribution to the $\mu \rightarrow 3e$ process to that of ordinary muon decay, $\mu \rightarrow e\nu\bar{\nu}$, which proceeds via W exchange and (almost) identical kinematics, [37] as shown in Figure 2.7 (right side) gives the relation

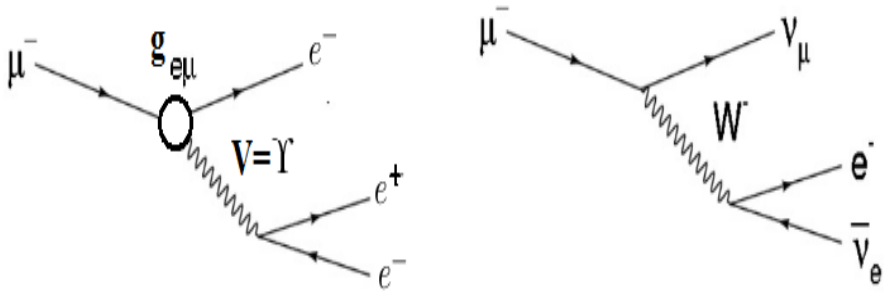

Figure 2.7: (Left)A vector exchange diagram contributing to $\mu \rightarrow 3e$. (Right) Ordinary muon decay, $\mu \rightarrow e\nu\bar{\nu}$, which proceeds via W exchange

$$A(\mu \rightarrow 3e) = (\bar{u}_{\mu}(p)\gamma^{\alpha}u_e(k_3))(\bar{v}_e(k_1)\gamma_{\alpha}u_e(k_2))\frac{g_{V_{e\mu}}g_{V_{ee}}}{M_V^2 - s} \tag{2.19}$$

$$\frac{[\Gamma(\mu \rightarrow 3e)]_{V-exch}}{[\Gamma(\mu \rightarrow e\nu\bar{\nu})]} \approx \frac{g^2V_{e\mu}g^2V_{ee}}{M_V^4} / \frac{g_W^4}{M_W^4} \tag{2.20}$$

Since $[\Gamma(V \rightarrow e^+e^-)] \sim g^2\ V_{ee}\ M_V$ and

$[\Gamma(V \rightarrow e^{\pm}\mu^{\mp})] \sim g^2\ V_{e\mu}\ M_V$, while $[\Gamma(W \rightarrow e\nu)] \sim g_W^2\ M_W$, we can rewrite equation 2.20 as

$$[BR(\mu \rightarrow 3e)]_{V-exch} \approx \frac{[\Gamma(V \rightarrow e^+e^-)][\Gamma(V \rightarrow e^{\pm}\mu^{\mp})]}{[\Gamma^2(W \rightarrow e\nu)]}(\frac{M_W}{M_V})^6 \tag{2.21}$$

Using BR ($\mu \rightarrow 3e < 10^{-12}$) [35] and other information pertaining to the widths of various vector mesons V_i, a set of theoretical bounds for the two-body LFV branching

ratios [37] [38] were calculated. These bounds are

$$BR(\phi \rightarrow e\mu) \leq 4 \times 10^{-17} \tag{2.22}$$

$$BR(J/\Psi \rightarrow e\mu) \leq 4 \times 10^{-13} \tag{2.23}$$

$$BR(Z^0 \rightarrow e\mu) \leq 5 \times 10^{-13} \tag{2.24}$$

By using equation 2.19 and 2.21, we can find the BR($\Upsilon(3S) \rightarrow e\mu$) as stated in equation 2.25

$$BR(\Upsilon \rightarrow e\mu) = BR(\mu \rightarrow eee)\frac{\Gamma(W \rightarrow e\nu)^2}{\Gamma(\Upsilon)(\Gamma(\Upsilon) \rightarrow ee)}(\frac{M_\Upsilon}{M_W})^6 \tag{2.25}$$

Using the updated decay widths and BF as given below we calculated theoretical BR($(\Upsilon(3S) \rightarrow e^{\pm}\mu^{\mp} \leq$) 2.5×10^{-8}. We note that there is a typographical error in equation 7 of reference [37] the exponent is -8 rather -9 as reported.

- BF($\mu \rightarrow$ eee) $\leq 1.0 \times 10^{-12}$ [35]
- BF($\mu \rightarrow e\nu\bar{\nu}$) $\simeq$ 100 %
- BF(W $\rightarrow e^{+}\nu$) $\simeq$ (10.71 $\pm$ 0.09) % [36]
- BF($\Upsilon(3S) \rightarrow l^{+}l^{-}$) $\simeq$ (2.18 $\pm$ 0.21) %
- $\Gamma(\Upsilon(3S)) = (20.32 \pm 1.85)\ keV$
- Γ(W) = (2.046 $\pm$ 0.049) GeV

As noted in references [37] and [38], the size of the vector boson exchange contribution to the $\mu \rightarrow 3e$ decay amplitude as determined above can be significantly reduced if there are kinematical suppressions. They note that such suppressions are possible when the effective boson couplings involve derivatives (or momentum factors). Reference [38] gives a specific example where the LFV vertex involves an anomalous magnetic moment coupling. This possibility means there could be effective tensor and pseudo-tensor LFV couplings in the $\mu \rightarrow 3e$ decay which would reduce the contribution of the virtual vector bosons, which for the Υ(3S) only has vector couplings. Reference [37] estimates that the contribution of the virtual $\Upsilon(3S) \rightarrow e^{\pm}\mu^{\mp}$ to the

$\mu \rightarrow 3e$ rate would be reduced by approximately $\frac{M_{\mu}^2}{(2\times M_{\Upsilon(3S)}^2)}$, or 5×10^{-5}. In such a scenario, this implies that the experimentally determined limit on $\mu \rightarrow 3e$ yields a limit on $\Upsilon(3S) \rightarrow e^{\pm}\mu^{\mp}$ of $\frac{2.5\times10^{-8}}{5\times10^{-5}} \sim 5 \times 10^{-4}$.

Recently, the SND Collaboration at the BINP (Novosibirk) [5] reported on the search for the LFV process on some channels as ϕ, (J/Ψ) in the energy region $\sqrt{s}$ = 948-1060 MeV at the VEPP-2M e^+e^- collider. However, no experimental search (either indirect or direct) or theoretical estimate on the direct decay on the branching fraction for $e^+ + e^- \rightarrow \Upsilon(nS) \rightarrow e^{\pm}\mu^{\mp}$ resonance been published yet. In this dissertation we are going to describe a direct search for LFV $\Upsilon(3S)$ decays, using data collected with the BaBar detector at the PEP-II B factory at SLAC National Accelerator Laboratory.

Assuming that the partial widths for LFV Υ decays are comparable at the $\Upsilon(2S)$, $\Upsilon(3S)$ and $\Upsilon(4S)$ resonances, the branching fractions for rare decays of the narrow (nS) resonances (henceforth n =2, 3) are enhanced by approximately $\frac{\Gamma\Upsilon(4S)}{\Gamma\Upsilon(nS)} = (10^3)$ [39] with respect to those of the $\Upsilon(4S)$. No signal is expected in data collected at the $\Upsilon(4S)$ since the LFV branching fractions are strongly suppressed, or in data collected away from the Υ resonances, since this data contains very few Υ decays.

Chapter 3

Experimental Apparatus

Due to huge infrastructure, e.g., accelerator, detector, location, finance, and manpower requirements the experimental particle physics researches are always in a big collaboration. The BaBar experiment is such a large international collaboration of scientists and engineers located at the SLAC National Accelerator Laboratory in the USA. The BaBar detector [40] is built around the interaction point of the high luminosity e^+e^- asymmetric collider PEP-II [41]. Even though the main focus of the experiment is to study the anti-matter nature by CP violations, BaBar physics results span a broad range of topics, including B, charm, and tau physics; CP violation; precision CKM measurements; charmonium and bottomonium states; hadron production; and searches for physics beyond the standard model. The data taking ended in 2008 and the machine and the detector are dismantled but analysis of those data taken still continues. In this chapter the design and performance details of the PEP-II collider and the BaBar detector are described.

3.1 The PEP-II Collider

PEP-II is an upgrade of the electron positron project (PEP) collider at the SLAC National Accelerator Laboratory on Stanford University campus in the USA. It has two independent storage rings, one located atop the other in the PEP tunnel. The high energy ring (HER) contains the 9 GeV electron beam, while the low energy ring (LER) carries the 3.1 GeV positron beam. The schematic representation of the PEP-II collider is shown in the Figure 3.1.

Electrons are produced by an electron gun, while positrons are created by firing an

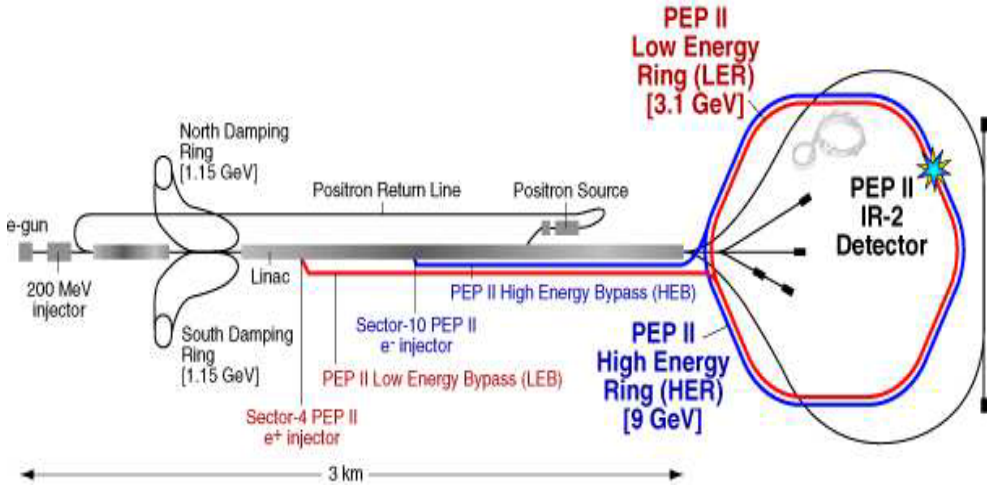

Figure 3.1: The Schematic representation of the PEP-II storage rings [42].

electron beam at a tungsten target to produce e^+e^- pairs via pair production. These are accelerated by the 2 mile long linear accelerator (LINAC), which injects into the 1.4 mile circumference PEP-II storage rings, as shown in Figure 3.1. These asymmetric beams collide at the center-of-mass (CM) energy of 10.58 GeV, corresponding to the mass of the $\Upsilon(4S)$ vector meson resonance as shown in the Figure 3.2. $\Upsilon(4S)$ decays almost exclusively to the $B\bar{B}$ pairs (either $B^0\bar{B}^0$ or B^+B^-) according to the SM.

Due to the asymmetric nature the collision, outgoing particles experience a Lorentz boost of $\beta\gamma = 0.56$ between the CM and the laboratory frames. This translates to a typical separation between the two B meson vertices of about 250 μm, within the resolution of the BaBar silicon vertex tracker. This allows the determination of their relative decay times and one can therefore measure the time dependent decay rates and CP-asymmetries.

3.1.1 The PEP-II Performances

The PEP-II collider was built with the designed luminosity of $3.0 \times 10^{33}\ cm^{-2}s^{-1}$. However, its actual performance far exceeded this target on August 16, 2006 when the BaBar detector recorded data at peak luminosity of $12.1 \times 10^{33}\ cm^{-2}s^{-1}$. The integrated luminosity of PEP-II collider, as shown in the Figure 3.3.

While most of the data was recorded at the Υ(4S) resonance peak, about 12 % of the measurements were taken at CM energy around 30 MeV lower. The off-peak

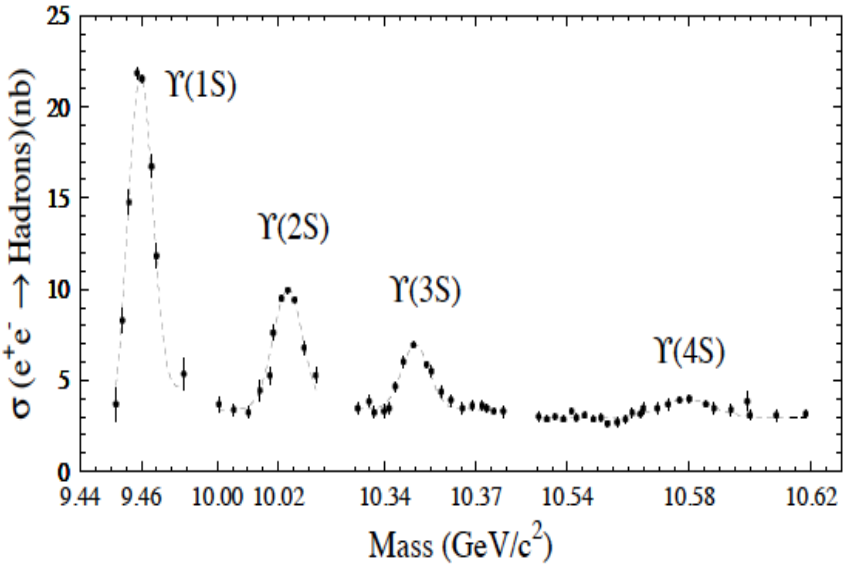

Figure 3.2: The first four S-wave Υ resonances shown with the hadronic cross section versus CM energy/c^2 in the Υ mass region [43].

dataset allows for studies of the non-resonant background. In addition, smaller data samples were recorded at the Υ(2S) and Υ(3S) resonances. The Υ resonances are shown in the Figure 3.2. The high energy beam was tuned to a lower energy reduced by 380 MeV to reach the Υ(3S) and reduced by 550 MeV to reach the Υ(2S). The data taking were in steps (called runs) corresponding to the PEP-II CM energy $\sqrt{s}$ for Υ resonances. Table 3.1 shows the data taking time periods with different runs.

In addition to $B\bar{B}$ pairs, there are many other processes take place, e.g. Bhabha scattering, muon production, tau production, $c\bar{c}$ and light quark production. As mentioned above the off peak data are used to study these processes in the continuum and to validate Monte Carlo simulations used for event selection optimization. Table 3.2 shows the production cross-section for various physics processes in BaBar experiment.

3.2 The BaBar Detector

The BaBar detector is a multi-system particle detector operated in the PEP-II collider interaction region as shown in Figure 3.4.

The coordinate system is defined as right handed where the origin (0,0,0) corresponds to the interaction point (IP). The +z axis is pointing in the direction of the electron beam along the beam line. The +y axis points upward, while the +x axis

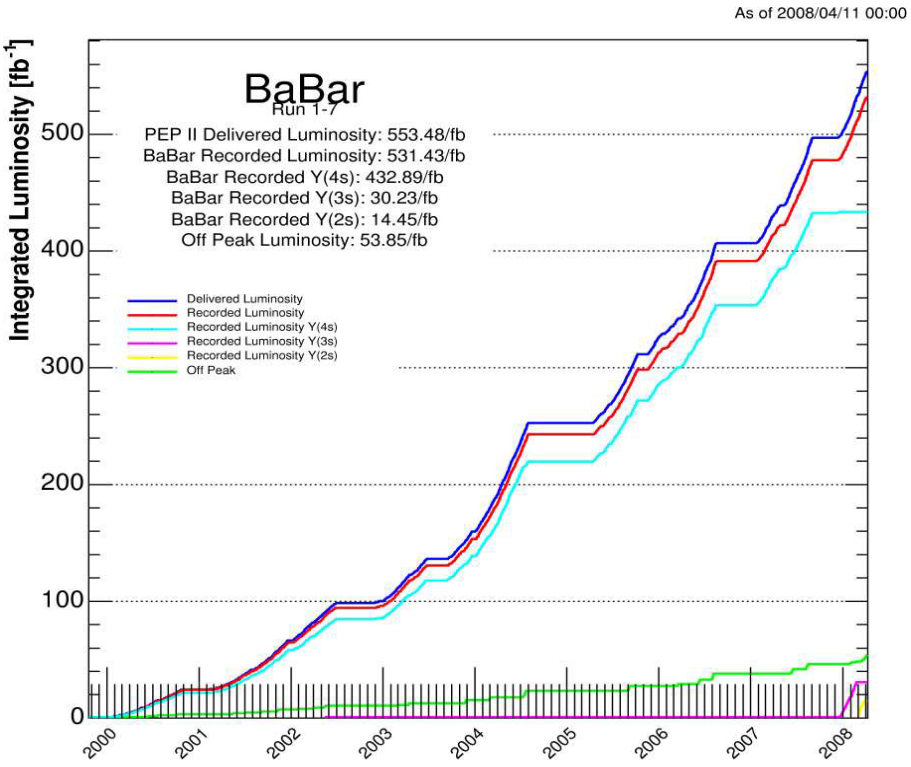

Figure 3.3: Total luminosity delivered by PEP-II from October 1999 to April 2008. The luminosities integrated by BaBar at different resonances are also shown [44].

points horizontally outward from the center of the storage rings. The BaBar detector was specifically designed to handle the asymmetric beam energies (from e^- and e^+) provided by the PEP-II storage rings, the detector was offset by 0.37 meters in the direction of the lower energy beam relative to the IP. The diverse physics program of the BaBar experiment requires that the detector has a large and uniform acceptance, especially in the boost direction. It must also have relatively good momentum and vertex resolution. The reconstruction efficiency is important for charged particles down to 60 MeV/c and for photons down to 20 MeV. The energy and angular resolution are important for photons with an energy between 20 MeV and 2 GeV. There must be efficient and accurate identification of electrons, muons and hadrons. The detector is made up of several subsystems, as shown in Figures 3.5 and 3.6.

Starting nearest the beam pipe and working outwards these systems are:

- The silicon vertex tracker (SVT): the SVT provides precise measurements of decay vertex positions and detection of low momentum charged particles;

- The drift chamber (DCH): the DCH measures the momentum of charged par-

Table 3.1: Data-taking period and the resonance corresponding to the PEP-II CM energy $\sqrt{s}$ for each of the BaBar runs [45].

Resonance	$\sqrt{s}$ in GeV	**Run**	**Month/Year**	**Luminosity** (fb^{-1})
Υ(4S)	10.579	Run1	10/1999 - 10/2000	20.37
		Run2	02/2001 - 06/2002	61.32
		Run3	12/2002 - 06/2003	32.28
		Run4	09/2003 - 07/2004	99.58
		Run5	04/2005 - 08/2006	132.33
		Run6	01/2007 - 09/2007	78.31
Υ(3S)	10.355	Run7	12/2007 - 02/2008	27.96
Υ(2S)	10.023	Run7	02/2008 - 03/2008	13.60

Table 3.2: Physics processes cross-sections for $\sqrt{s}$ = 10.58 GeV ($M_{\Upsilon(4S)}$) at BaBar [46],[47].

$e^+e^- \rightarrow$	**cross section (nb)**
$b\bar{b}$	1.05
$c\bar{c}$	1.30
$s\bar{s}$	0.35
$u\bar{u}$	1.39
$d\bar{d}$	0.35
$\tau\bar{\tau}$	0.92
$\mu\bar{\mu}$	1.16
e^+e^-	$\sim$ 40

ticles and it also provides measurements of the ionization energy loss per unit length (dE/dx) for use in particle identification(PID);

- The ring-imaging Cherenkov detector (DIRC): the DIRC is a device providing separation of pions, kaons and protons from 500 MeV to 4.5 GeV;

- The electromagnetic calorimeter (EMC): the EMC is designed to measure the energy deposits of charged and neutral particles from 20 MeV to 9 GeV, mostly photons and electrons; it also measures minimum ionize particles and particles that interact hadronically.

- The superconducting solenoid: Apart from the IFR the whole detector is sur-

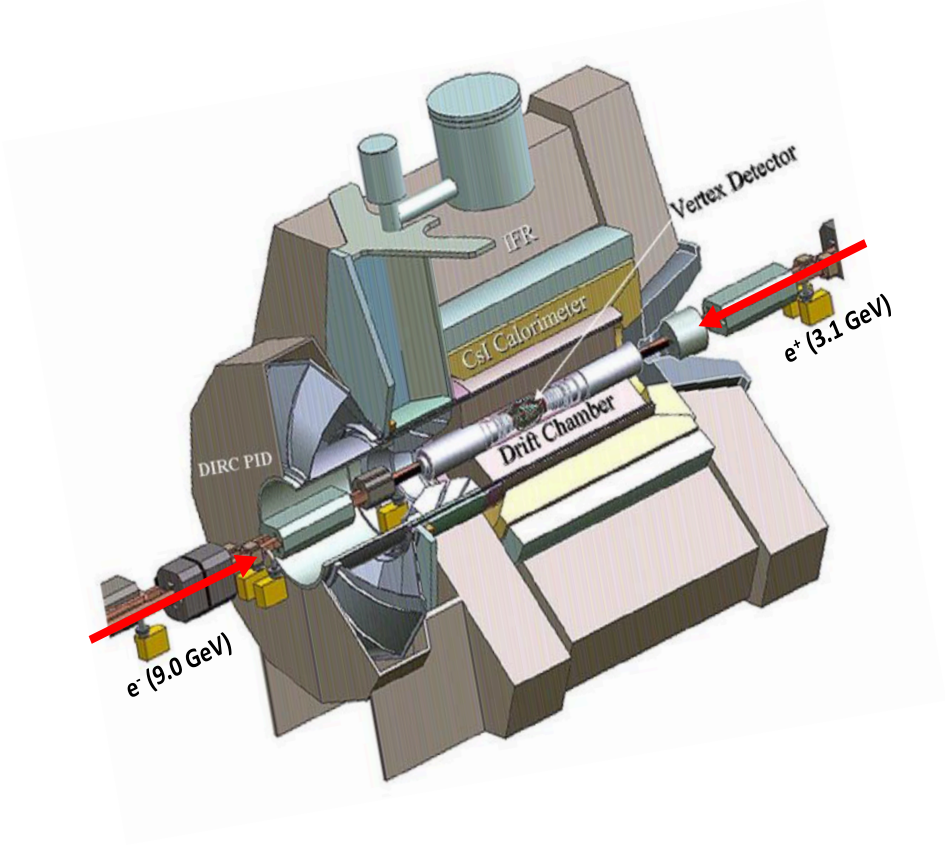

Figure 3.4: Schematic view of the BaBar detector [48]. From top to bottom the detector is about 6.5m.

rounded by a uniform magnetic field of 1.5 T which allows to measure the momentum of charged particles;

- The instrumented flux return (IFR): the Instrumented Flux Return is primarily used for identification of muons and neutral hadrons such as K_L.

There are significant amounts of radiation and high level of background, which must be tolerated by each subsystem, and the components must be robust and reliable as access to much of the detector is difficult. Both end doors of the IFR and the endcap of the EMC are split vertically so that they can open up to give access to some inner components. The calorimeter has a barrel and an endcap which extends it asymmetrically into the forward direction (e^- beam direction), where many of the collision products emerge. All the detectors located inside the magnet have full

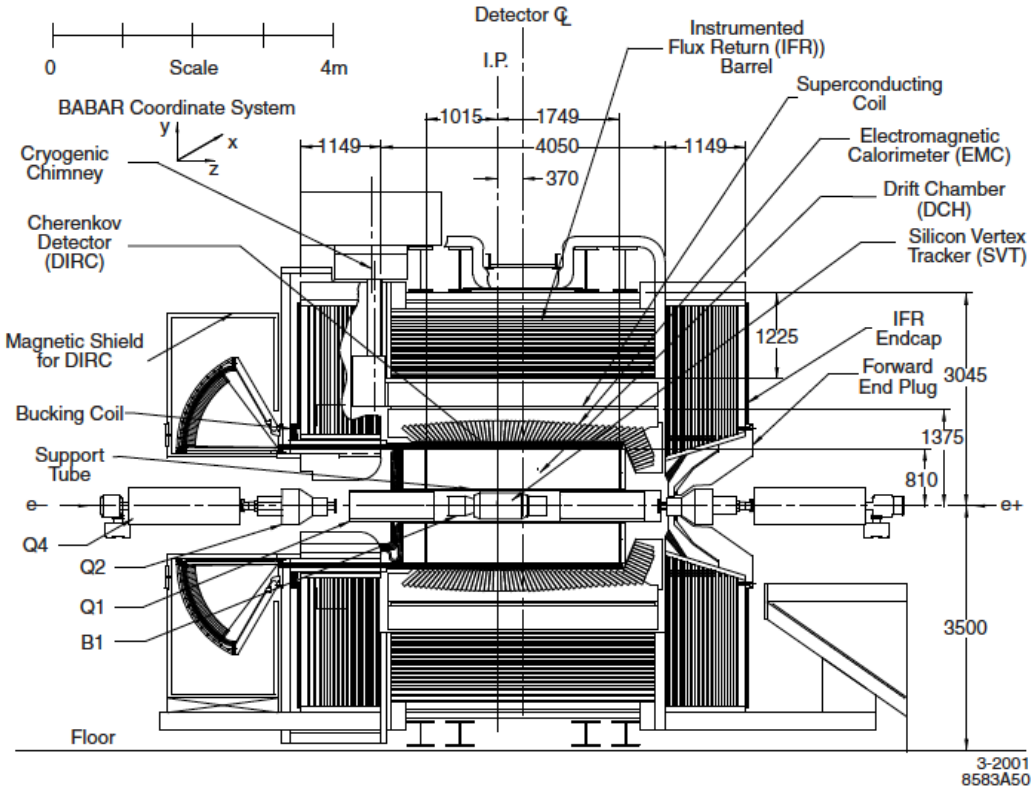

Figure 3.5: Cross-sectional schematic drawing of the BaBar detector: side view [49].

acceptance in azimuth (ϕ). The instrumented flux return (IFR) outside the cryostat is composed of 18 layers of steel, which increase in thickness outwards, with in-between 19 layers of planar resistive plate chambers (RPC) or limited streamer tubes (LST) in the barrel and 18 in the end-caps. Between run5 and run6 the active detectors were changed to LST and the iron partially reconfigured. Once the data are taken, the trigger system must select the physics events required to achieve the physics goals and reject background events, both with well understood efficiencies. This is done in two sequential stages using information from the DCH, EMC and IFR.

3.3 The Silicon Vertex Tracker (SVT)

The Silicon Vertex Tracker (SVT) is the innermost part of the BaBar detector located around the interaction region of e^- and e^+ beams. The SVT uses silicon strip sensors and is responsible to precisely reconstruct the trajectories and decay vertices of charged particles near the IP.

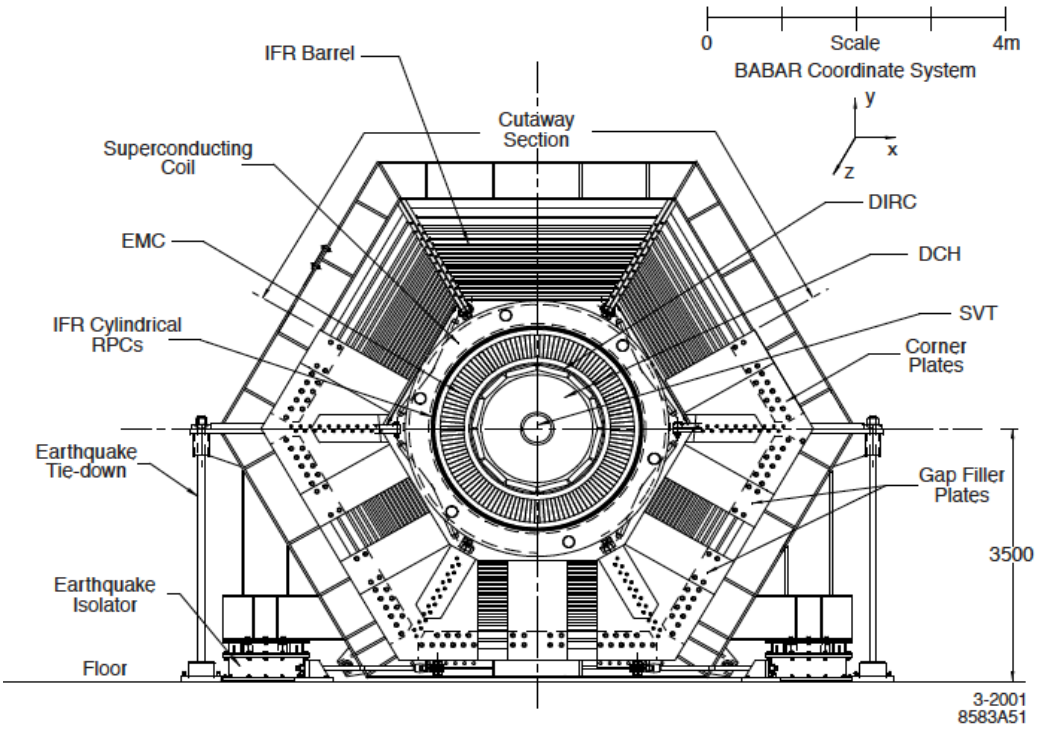

Figure 3.6: Cross-sectional schematic drawing of the BaBar detector: beams-eye view [49].

After producing from the $\Upsilon(4S)$, many of the decay products of a B meson have low transverse momentum (< 150 MeV/c), and the SVT provides standalone tracking for those particles. The design goal of SVT was reconstructing B and D meson decay vertices with a precision of 80 μm along the meson flight direction and to provide tracking information with an efficiency larger than 80% for low transverse-momentum (< 120 MeV/c) particles such as soft pions from D^* mesons. It also requires the resolution of ~ 100 μm in the x-y transverse plane for reconstructing the final state particles in B, τ, and charm decays. Finally, the SVT supplies PID information by measuring dE/dx both for low and high momentum tracks. It can achieve a 2σ separation between kaons and pions up to a momentum of 500 MeV/c, and between kaons and protons up to a momentum of 1 GeV/c.

3.3.1 Design of the SVT

The SVT of the BaBar detector, housed inside the 4.5m-long support tube, consists of five unequally-spaced layers of double-sided silicon microstrip sensors [50], where

strips on one side are oriented parallel to the beam to provide angular information, while strips on the other side are oriented perpendicular to the beam to measure z. Each sensor is 300 μm thick and organized into modules arranged in 5 concentric layers, as shown in Figures 3.7 and 3.8.

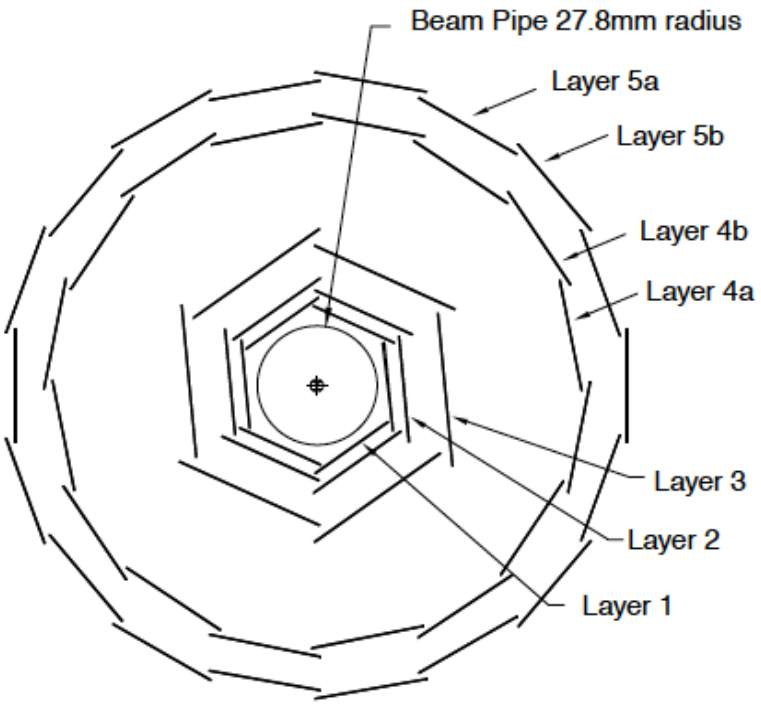

Figure 3.7: Schematic view of the SVT: transverse section [49].

Three inner layers, barrel-shaped and composed of six modules each, are responsible for providing angle and position information for the measurement of the vertex position. In order to minimize the effect of multiple scattering in the beam pipe, these layers are mounted as close to the beam pipe as possible. They are placed next to the interaction region, at radii 3.3, 4.0 and 5.9 cm from the beam axis, respectively. In order to cover the full azimuthal range, there are slight overlaps on segments at the edges of each layer (5°). The outer two layers, composed by 16 and 18 modules, have a peculiar arch structure to reduce the incident angles of particles going in the forward and backward direction; their barrel parts are placed at radii between 12.7 and 14.6 cm from the beam axis.

The outer two layers provide position and angle measurements to link the tracks with the DCH measurements and they are necessary for pattern recognition and low

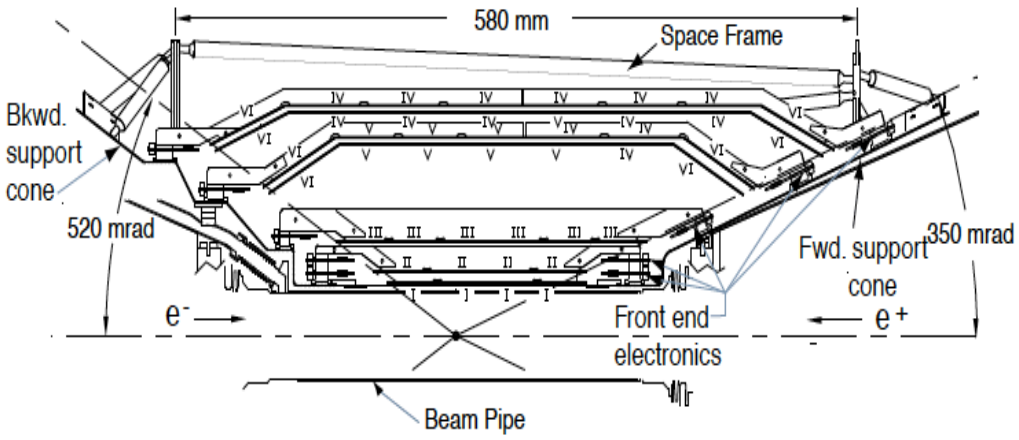

Figure 3.8: Schematic view of the SVT longitudinal section. The angular coverage is indicated, it is constrainted to be 350 mrad (20°) in the forward direction and 520 mrad (30°) in the backward direction due to the presence of the B1 magnets. [49].

p_t tracking. The total number of read out channels exceeds 150,000, and the total active silicon area is 0.96 m^2. Each silicon detector consists of a high-resistivity n^- bulk implanted with p^+ strips on one side and orthogonally-oriented n^+ strips on the other side. The strips are AC-coupled to the electronics via integrated decoupling capacitor.

3.3.2 Performance of the SVT

The SVT efficiency can be calculated for each half-module by comparing the number of associated hits to the number of tracks crossing the active area of the module. Excluding 9 out of 208 defective readout sections, the combined hardware and software efficiency is measured to be about 97%. The spatial resolution of SVT hits is determined by measuring the distance (in the plane of the sensor) between the track trajectory and the hit, using high-momentum tracks in two prong events. The uncertainty due to the track trajectory is subtracted from the width of the residual distribution to obtain the hit resolution. Figure 3.9 shows the SVT hit resolution for z and ϕ side hits as a function of track incident angle, for each of the five layers. The measured resolutions are in excellent agreement with expectations from Monte Carlo simulations.

Most of the physics analysis at BaBar uses five parameters (d_0, ϕ_0, ω, z_0, and tanλ)

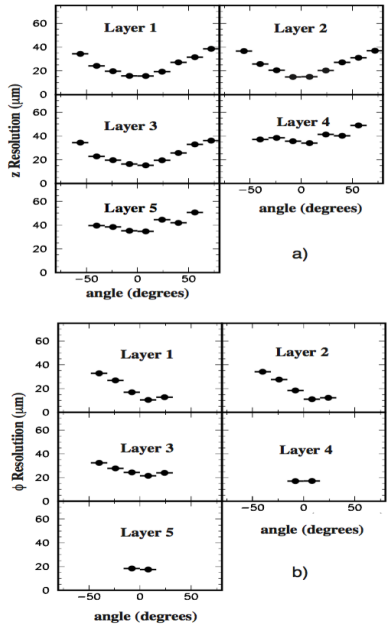

Figure 3.9: SVT hit resolution for five layers in the a) z and b) ϕ coordinate in microns, plotted as a function of track incident angle in degrees. [49].

to define charged tracks at POCA (point of closest approach) to the z axis along with the associated error matrix. d_0 is defined as the distance of closest approach to the z axis, ϕ_0 is the corresponding azimuthal angle, z_0 is the corresponding distance along z axis, λ is the angle between the transverse plane and the track tangent vector at POCA (also called dip angle), and ω is known as the curvature of the track.

3.4 Drift Chamber (DCH)

A drift chamber is a particle tracking detector that measure the drift time of ionization electrons in a gas to calculate the spacial position of ionizing particle. In the BaBar experiment, the DCH plays an important role to detect the charged particles and

measure their momenta and angles for high precision reconstruction of the decay products of B and D mesons. The DCH can provide up to 40 measurements of space coordinates per track, which ensures the high reconstruction efficiency of tracks with transverse momenta greater than 100 MeV/c. The DCH, together with the SVT, is the BaBar tracking system and provides an excellent spatial momentum resolution required for many physics analyses in the BaBar experiment. The DCH also measure the longitudinal position of tracks with a resolution of $\sim$ 1 mm, since this is the sole detector to measures the reconstruction of decay and collision vertices [1] outside of the Silicon Vertex Detector (SVT).

The main goals of the DCH, explained in detail elsewhere [51], are: provide spatial resolution better than 140 μm, averaged over the cell in the R - ϕ plane; and to supply particle identification for low momentum tracks by dE/dx [2], with a resolution of 7 % (for 40 measurements). Since the average momenta of charged particles produced in B and D meson decays is less than 1 GeV/c, multiple scattering is a significant, if not the dominant limitation on the track parameter resolution. In order to reduce this contribution, material in front of and inside the chamber volume has to be minimized [47]. For tracks with momenta above 1 GeV/c, a resolution of $\sigma_{p_t} \approx 0.3\% \times p_t$ is expected. The angular acceptance in the forward region must extend down to the beam-line components, i.e., 300 mr. In addition, the drift chamber is designed to provide one of the principal triggers for the experiment [49].

3.4.1 Drift Chamber Design and Performances

The Drift Chamber at BaBar is a 3 m long cylinder having 23.6 cm inner and 80.9 cm outer radii respectively, as shown in the Figure 3.10. Since the BaBar events will be boosted in the forward direction, the design of the detector is optimized to reduce the material in the forward end. The forward endplate is made thinner (12 mm) in the acceptance region of the detector compared to the rear endplate (24 mm), and all the electronics are mounted on the rear endplate. The inner cylinder is made of 1 mm beryllium, which corresponds to 0.28 % radiation lengths (X_0). The outer cylinder consists of 2 layers of carbon fiber on a Nomex core, corresponding to 1.5% X_0.

Drift cells in the DCH are arranged in 10 super-layers of 4 layers each, for a total of 40 layers. It contains 7104 hexagonal cells, each having a typical dimension of

[1] K_s^0 decays and interaction vertices must be measured entirely in the DCH

[2] Energy loss of a moving charged particle per unit distance

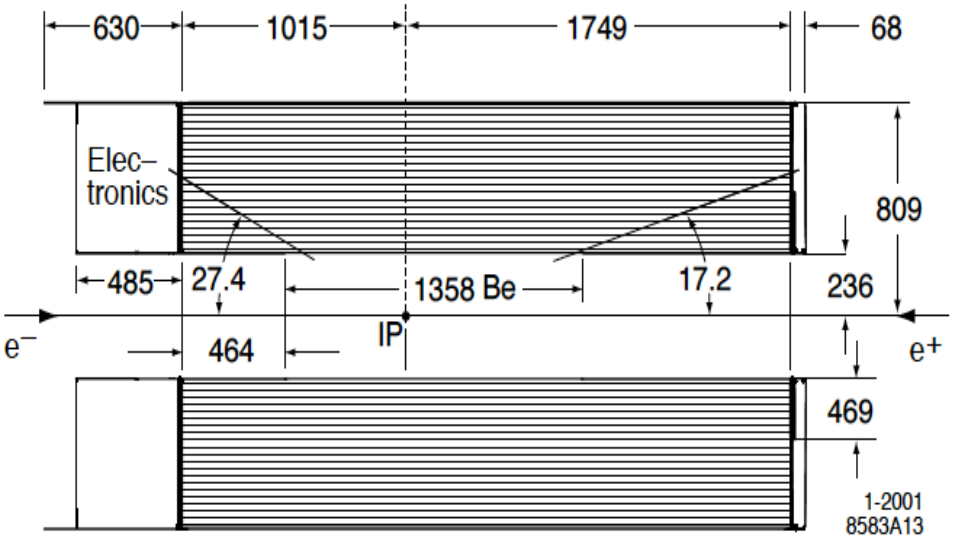

Figure 3.10: Longitudinal section of the DCH with principal dimensions; the chamber center is offset by 370 mm from the interaction point (IP)[49].

1.2 (high) $\times$ 1.8 (wide) cm^2. Sequential layers are staggered by half a cell. This arrangement enables local segment finding and left-right ambiguity resolution within a super-layer, even if one out of four signals is missing. The stereo angles of the super-layers alternate between axial (A) and stereo (U,V) pairs, in the order AUVAUVAUVA, as shown in Figures 3.11 and 3.12 side-by-side. The 40 layers provide up to 40 spatial and ionization loss measurements for charged particles with p_t greater than 180 MeV/c. The electronics provides prompt trigger signals by sending the hit information from all 7104 channels to the Level 1 Trigger system at a sampling frequency of 3.75 MHz. The system is designed to maintain good performance in severe background conditions. The expected single-cell efficiency for the trigger signal is greater than 95%.

The gas mixture (He:C_4H_{10}, 80%:20%) used in the DCH has five times larger radiation length than commonly used Argon based gases. The angle between the drift direction of electrons under the influence of magnetic field and the direction of electric field (known as Lorentz angle), is small and its important for the better spatial resolution. Table 3.3 show the gas mixture and its properties used in BaBar DCH system.

For measuring the energy loss per unit length, the total charge deposited in each drift cell along the tack path is measured. Figure 3.13 shows the dE/dx distributions

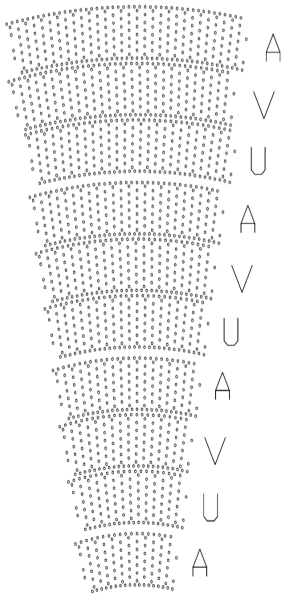

Figure 3.11: 10 super-layer cells layout in the BaBar drift chamber [47].

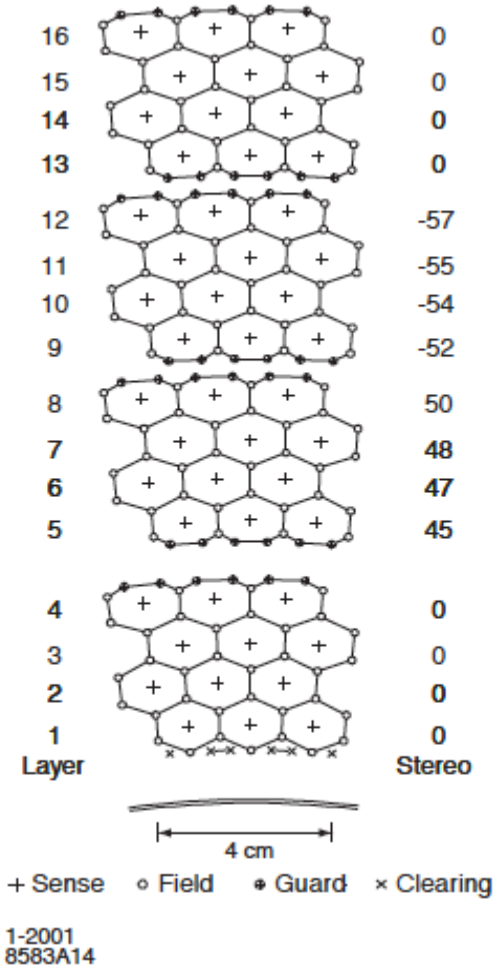

Figure 3.12: Schematic layout of drift cells for the four innermost superlayers [49].

for different charged particles with respect to the particles momentum. The Drift Chamber has been performing extremely well over the entire BaBar operating time. The DCH also dominates the precision of momentum measurement for most tracks, parametrized by

$$\frac{\sigma_{p_t}}{p_t} = (0.13 \pm 0.01)\% \times p_t + (0.45 \pm 0.03)\% \tag{3.1}$$

where p_t is measured in GeV/c. The first contribution, dominating at high p_t, comes from the curvature error due to finite spatial measurement resolution; the second contribution, dominating at low momenta, is due to multiple Coulomb scattering.

Table 3.3: Properties of helium-isobutane gas mixture at atmospheric pressure and 20^0C. The drift velocity is given for operation without magnetic field, while the Lorentz angle is stated for a 1.5T magnetic field.[47].

Parameter	**Values**
Mixure He:C_4H_{10}	80:20
Radiation Length	807 m
Primary Ions	21.2/cm
Drift Velocity	22 μm/ ns
Lorentz Angle	32^0
dE/dx Resolution	6.9 %

3.5 The DIRC

When a charged particle (such as an electron) moves through a dielectric medium faster than the phase velocity of light in that medium, it emits a radiation called Cherenkov radiation with an angle θ_c. The Cherenkov angle depends on the velocity, v, of the particle and the refractive index, n, of the radiator material according to the relation where β = v/c and c is the velocity of light. The relationship between the Cherenkov angle (measured by the DIRC) and the particle momentum (measured by the tracking system) depends on the particle mass, as illustrated by Figure 3.14, and therefore, different particles will have different θ_c values and this information together with the information of the tracking system allows particle identification (PID).

$$cos\theta_c = \frac{1}{n\beta} \tag{3.2}$$

PID is needed both for flavour tagging and to reconstruct exclusive final states, mainly for separation of kaons vs pions and protons. Information from the Drift Chamber, Calorimeter, and the Instrumented Flux Return can be used to identify most of the leptons and many of the hadrons. However, these subsystems are not sufficient to distinguish pions from kaons with momentum greater than 700 MeV/c, or protons above 1.3 GeV/c. The DIRC was designed to provide at least 3σ separation between high-momentum pions and kaons. The DIRC inverts the traditional concept of ring-imaging Cherenkov counters (RICH) in that it relies on the detection of Cherenkov photons trapped in the radiator due to total internal reflection [53].

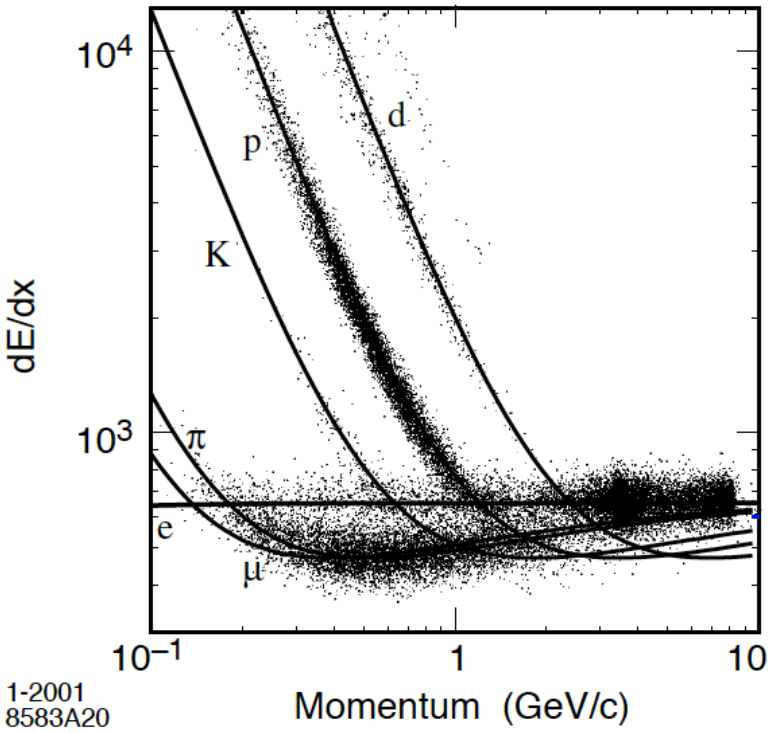

Figure 3.13: Measurement of dE/dx in the DCH as a function of track momenta[49].

3.5.1 Design and performance of the DIRC

As shown in the Figure 3.15, the DIRC consists of 144 synthetic quartz bars that trap Cherenkov light via total internal reflection. These bars are arranged in a 12 sided polygonal barrel optically isolated by a $\sim$ 150 μm air gap between neighboring bars, enforced by custom shims made from aluminum foil. Since the electron beam is more energetic than the positron beam, particles produced in the collision are preferentially in the forward region and, to minimize interference with other detector systems in the forward region, the DIRC photon detector is placed at the backward end. The bars are 17 mm thick, 35 mm wide, and 4.9 m long. Each bar is assembled from four 1.225 m pieces that are glued end-to-end; this length is the longest high-quality bar currently obtainable [40]. The Cherenkov light that propagates via total internal reflection is detected by an array of photomultiplier tubes (PMTs).

The standoff box is made of stainless steel, consisting of a cone, cylinder, and 12 sectors of PMTs. It contains about 6,000 liters of purified water. Water is used to fill this region because it is inexpensive and has an average index of refraction (n $\sim$ 1.346) reasonably close to that of fused silica, thus minimizing the total internal

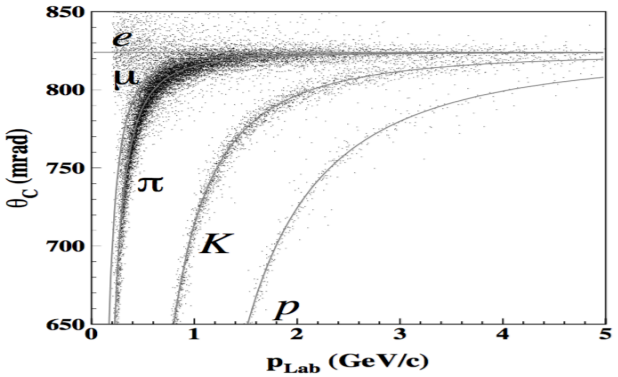

Figure 3.14: The Cherenkov angle, θ_c, of tracks from an inclusive sample of multihadron events plotted against the momentum of the tracks at the entrance to the DIRC. The grey lines are the predicted values of θ_c for different particle species (from [52]).

reflection at silica-water interface. Six m^3 of water are needed to fill the Standoff Box, and about 11,000 PMTs to cover the detection area.

The DIRC has been robust and stable and, two years after installation, about 99.7 % of all PMTs and electronic channels are operating with nominal performance. It is possible to achieve a 4.3 σ separation of π-K at 3 GeV/c.

3.6 The Electromagnetic Calorimeter (EMC)

A calorimeter, an important part of a particle detector used for measuring the energy and position of a particle, absorbs the full kinetic energy of incident particle, and provides signal proportional to that deposited energy. Calorimeters are distinct

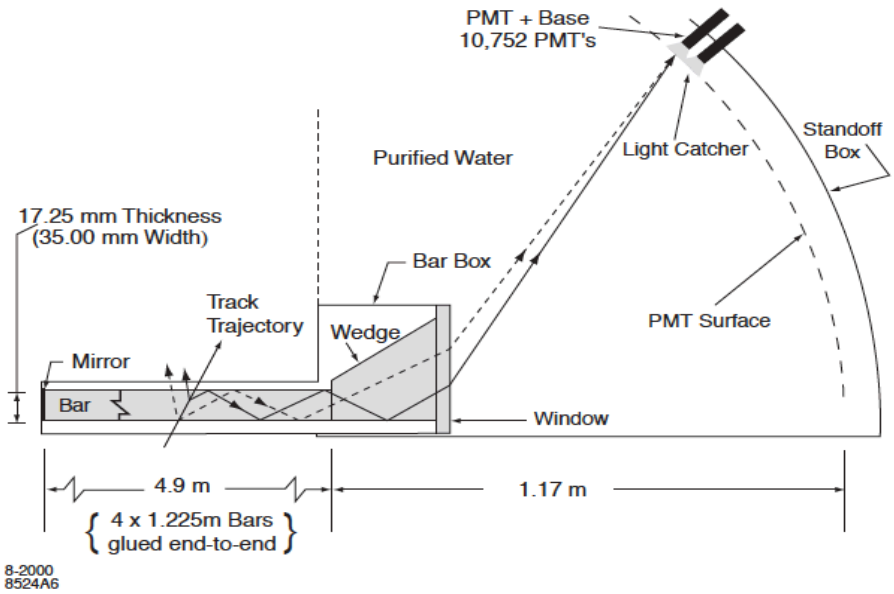

Figure 3.15: Schematics of the DIRC fused silica radiator bar and imaging region [49].

from most other parts (sub-detectors) of a particle detector in that: the nature of the particle is changed by the detector; and they can detect the charged as well as neutral particles. Since the original particle no longer exists after the measurement, the energy measurement by a calorimeter is a destructive process. Calorimeters in a particle detector always exist behind charged particle tracking chambers, which are non-destructive measuring devices. Calorimeters are often classified as electromagnetic and hadronic for measuring particles position and energy based on their identifications.

The Electromagnetic Calorimeter (EMC) plays a central role in the BaBar experiment. It also plays an important role in the analysis $e^+e^- \rightarrow \Upsilon(3S) \rightarrow e\mu$, which is the subject matter of this thesis. The EMC at BaBar detector is designed to measure electromagnetic showers with excellent efficiency, and energy and angular resolution over the energy range from 20 MeV to 9 GeV.

Electromagnetic Shower

A shower is a cascade of secondary particles resulting from a high-energy particle interacting with dense matter. Electromagnetic showers are produced by e, γ etc. via the electromagnetic force. An electromagnetic shower begins when the above

mentioned particles enter into a material with an energy > 10 MeV. A highly energetic electron enters into the matter and produce bremsstrahlung [3] as shown in the Figure 3.16. On the other hand, a high energy photon interacting with matter converts into an electron and positron pairs as shown in the Figure 3.17.

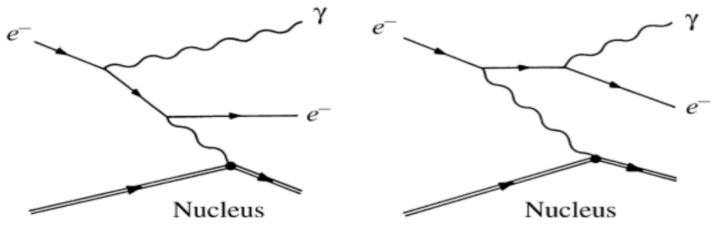

Figure 3.16: Dominant Feynman diagrams for the bremsstrahlung process e^- +(Z,A) $\rightarrow e^- + \gamma$ + (Z,A) [54].

The resulting electrons and positrons may produce another photon via bremsstrahlung. These in turn convert into further electron-positron pairs and so on. The result is a cascade or shower of photons, electrons and positrons as shown in Figure 3.18. This continues until the energy of the pair-produced electrons and positrons drops below the critical energy [4]. Below the critical energy electrons lose their energy via ionization and photons lose their energy by Compton and Rayleigh scattering. Electromagnetic showers are characterized longitudinally by the radiation length X_0 [55] and by narrow transverse profiles.

[3] Bremsstrahlung radiation is the radiation due to the deceleration of a charged particle, such as an electron, when deflected by another charged particle, such as an atomic nucleus.

[4] The critical energy is the energy at which the energy loss via ionization is equal to the energy loss via bremsstrahlung

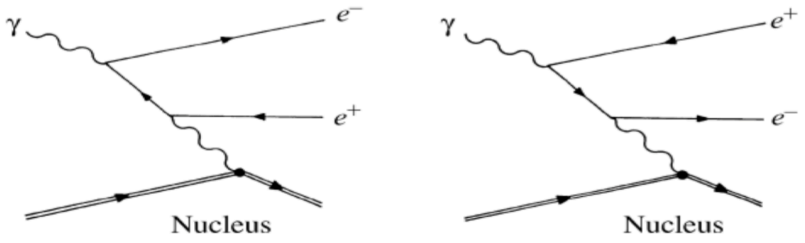

Figure 3.17: The pair production process γ + (Z, A) $\rightarrow e^- + e^+$ + (Z, A) [54].

3.6.1 The EMC Design and Performance

The electromagnetic calorimeter at BaBar, a nearly hermetic design [5], total-absorption detector, is composed of an array of 6580 Thallium activated CsI [6] crystals. This type of crystal calorimeter has detection efficiencies close to 100 % when a photon, electron or positron impacts it with an energy above 20 MeV. The crystals are read out with silicon photodiodes that are matched to the spectrum of scintillation light.

Properties of CsI(Tl) are summarized in Table 3.4: the high light yield and small Moliere radius give the excellent energy and angular resolution required, while the short radiation length guarantees complete shower containment at BaBar energies with a relatively compact design.

All CsI(TI) crystals are pointing toward the interaction point and arranged in a cylindrical barrel and a conical forward endcap region. The EMC has full coverage in azimuth and extends in polar angle from 15.8^0 to 141.8^0 corresponding to a solid-angle coverage of 90% in the CM system as shown in the Figure 3.19.

The barrel contains 5,760 crystals arranged in 48 distinct rings with 120 identical crystals each. The endcap holds 820 crystals arranged in eight rings. The precision with which the energy of a particle can be measured in a calorimeter is known as

[5] It covers most of the 4π steradians of solid angle around the interaction point.

[6] CsI is the an ionic compound of Cesium and Iodine.

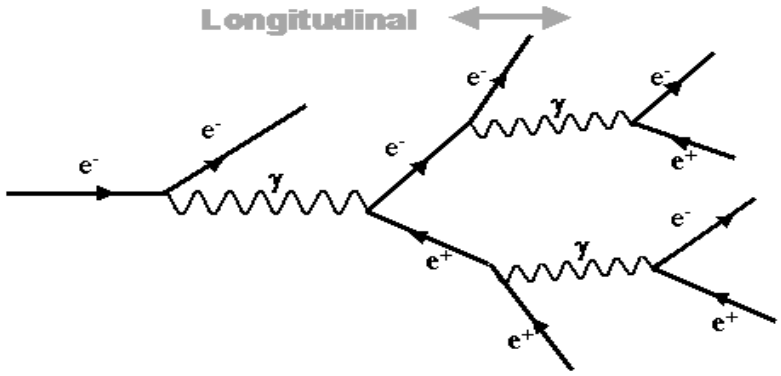

Figure 3.18: Schematic view of an electromagnetic shower propagating longitudinally [56].

its energy resolution. The determination of the energy resolution of a calorimeter depends on the actual energy deposited in the calorimeter (sampling fluctuation), leakage of energy out of the calorimeter, noise from electronics, ion or light collection, etc. The energy resolution of a homogeneous crystal calorimeter can be described empirically in terms of a sum of two terms added in quadrature

$$\frac{\sigma_E}{E} = \frac{a}{\sqrt[4]{E(GeV)}} \oplus b \tag{3.3}$$

where E and σ_E are the energy of a photon and its root mean square (rms) error, measured in GeV, a is mainly the fluctuation in photon statistics (plus electronic noise of the photon detector and electronics if any), and b is the non-uniformity in light collection, leakage or absorption in the material between and in front of the crystals, and uncertainties in the calibrations (dominant at higher energies (1 GeV)). The

Table 3.4: Properties of CsI(Tl) [47].

Parameter	**Values**
Radiation Length	1.85 cm
Moli'ere Radius	3.8 cm
Density	4.53 g/cm^3
Light Yield	50,000γ/MeV
Light Yield Temp. Coeff.	$0.28\%/^0C$
Peak Emission λ_{max}	565 nm
Refractive Index (λ_{max})	1.80
Signal Decay Time	680 ns (64%)
	3.34 μs (36%)

angular resolution can also be determined empirically as

$$\sigma_\theta = \sigma_\phi = \frac{c}{\sqrt{E(GeV)}} + d \tag{3.4}$$

The design of the EMC was made on the basis of extensive studies, prototyping and beam tests [57], and Monte Carlo simulation, taking into account limitations of space and the impact of other BaBar detector systems.

The crystals are 4.7 cm × 4.7 cm in cross-section and vary in length from 29.6 cm (16 X_0) to 32.4 cm (17.5 X_0). Each crystal has a thin reflective coating to contain the scintillation light produced by an incident particle. Two silicon photodiodes with quantum efficiency of 85% read out the signal from the back of each crystal as shown in the Figure 3.20.

Electrons are separated from charged hadrons almost exclusively on the basis of the energy measurements from the EMC and the momentum measurements in the DCH. In addition, the measured energy loss and reconstructed Cherenkov angle must be be consistent with an electron. An important variable for discriminating between hadrons and electrons is the ratio of shower energy to the track momentum (E/| P |). The calorimeter is calibrated using 6.13 MeV gamma rays from activated fluorinert fluid, as well as with $e^+e^- \rightarrow e^+e^-$ Bhabha scattering events that produce 39 GeV clusters for high-energy cal- ibration. The energy and angular resolutions are parametrized as follows:

$$\frac{\sigma_E}{E} = \frac{(2.32 \pm 0.30)\%}{\sqrt[4]{E(GeV)}} \oplus (1.85 \pm 0.12)\% \tag{3.5}$$

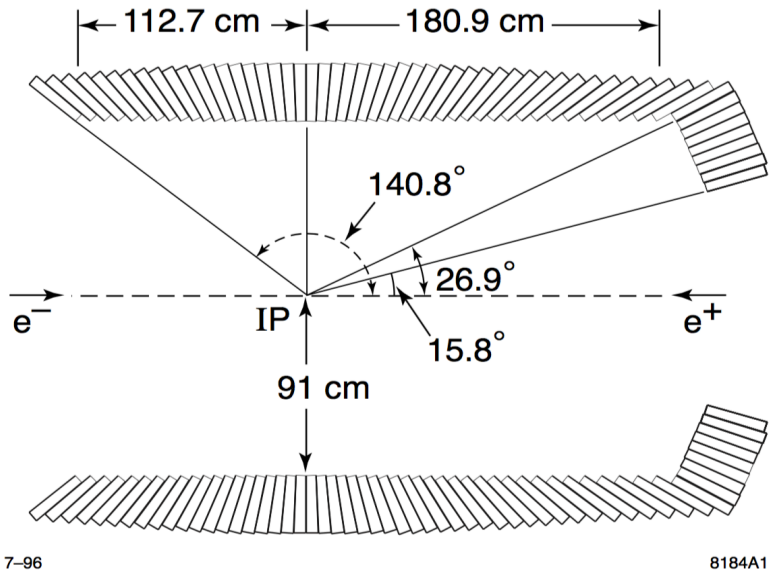

Figure 3.19: The EMC layout: Side view showing dimensions (in mm) of the calorimeter barrel and forward endcap [47].

$$\sigma_\theta = \sigma_\phi = \frac{(3.87 \pm 0.07)}{\sqrt{E(GeV)}} + 0.00 \pm 0.04 mrad \tag{3.6}$$

3.7 Solenoid Magnet

The BaBar experiment has a 1.5 T (Tesla) superconducting solenoid, a segmented flux return, and a bucking coil for field compensation. The magnetic field created by superconducting solenoid is required to achieve the desired momentum resolution for charged particles. The solenoid is made of 10.3 km of niobium- titanium filaments, each less than 40 μm in diameter, and a pure aluminium stabilizer. It is cooled to a temperature of 4.5 K using liquid helium [52]. The flux return, made of low-carbon steel, provides structure and support for the detector subsystems and serves as a hadron absorber for muon/hadron separation, which is discussed in the following section.

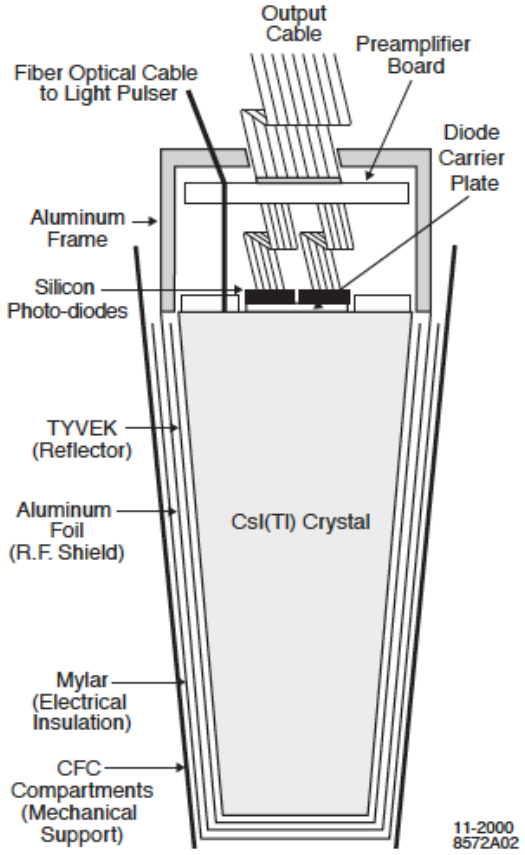

Figure 3.20: Schematic drawing of an EMC crystal [49].

3.8 Instrumented Flux Return (IFR)

Muons are also charged particles but they are about 200 times heavier than electrons and having sufficient lifetime to be detected, which makes the behavior of high-energy muons as they pass through matter quite different from those of electrons. The force from the electric field is not large enough at these energies to cause the muon to change direction significantly and it goes right through the field region without significantly radiating photons to produce pairs or showers. Muons can penetrate through the calorimeters and reach the outermost part of BaBar detector, known as the Instrumented Flux Return (IFR). The IFR surrounds the calorimeters and designed to identify muons with high efficiency and good purity (down to momenta below 1 GeV/c), and to detect neutral hadrons (primarily K_L^0 and neutrons) over a wide range of momenta and angles. Identifying Muon with high precision is very

important in this analysis $e^+e^- \rightarrow \Upsilon(3S) \rightarrow e\mu$.

3.8.1 The IFR Design and Performance

The IFR consists of a central part (Barrel), and two plugs (End Caps), which complete the solid angle coverage down to 300 mrad in the forward direction and 400 mrad in the backward direction. The IFR uses the steel flux return of the magnet as a muon filter and hadron absorber. Single gap resistive plate chambers (RPCs) with two-coordinate readout have been chosen as detectors [58]. The RPCs are installed in the gaps of the finely segmented steel of the barrel and the end doors of the flux return, as illustrated in Figure 3.21. The steel segmentation has been chosen on the basis of Monte Carlo studies of muon penetration and charged and neutral hadron interactions. The steel is segmented into 18 plates, increasing in thickness from 2 cm for the inner nine plates to 10 cm for the outermost plates. The nominal gap between the steel plates is 3.5 cm in the inner layers of the barrel and 3.2 cm elsewhere. There are 19 RPC layers in the barrel and 18 in the endcaps. In addition, two layers of cylindrical RPCs are installed between the EMC and the magnet cryostat to detect particles exiting the EMC. The muon system upgradation has been done in 2002 [59].

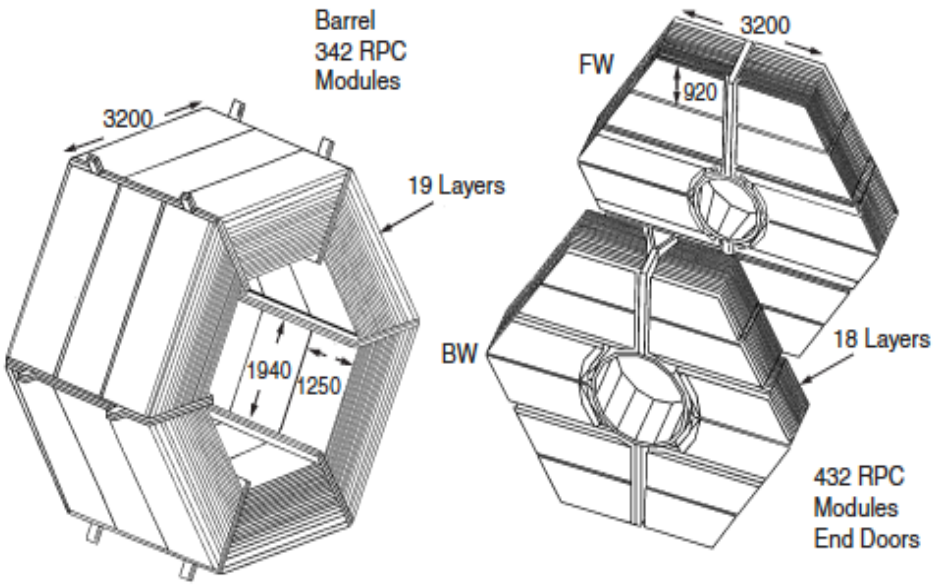

Figure 3.21: Overview of the IFR Barrel sectors and forward and backward end-doors; the shape of the RPC modules and the way they are stratified is shown [49].

The efficiency of the RPCs is evaluated both for normal collision data ($e^+e^- \rightarrow \mu^+\mu^-$) and for cosmic ray muons recorded with the IFR trigger. While muon identification relies almost entirely on the IFR, other detector systems provide complementary information. To identify muons, a number of variables are defined for each IFR cluster associated with a charged track to discriminate muons from charged hadrons: 1) the total number of interaction lengths traversed from the IP to the last RPC layer with an associated cluster, 2) the difference between this measured number of interaction lengths and the number of interaction lengths predicted for a muon of the same momentum and angle, 3) the average number and the rms of the distribution of RPC strips per layer, 4) the χ^2 for the geometric match between the projected track and the centroids of clusters in different RPC layers, and 5) the χ^2 of a polynomial fit to the two-dimensional IFR clusters. The performance of muon identification has been tested on samples of muons from $\mu\mu$ee and $\mu\mu\gamma$ final states and pions from three-prong τ decays and $K_s \rightarrow \pi^+\pi^-$ decays. The selection of these control samples is based on kinematic variables, and not on variables used for muon identification. A muon detection efficiency of close to 90 % has been achieved in the momentum range of $1.5 < p < 3.0$ GeV/c with a fake rate for pions of about 6 - 8 %. Decays in flight contribute about 2 % to the pion misidentification probability. The hadron misidentification can be reduced by a factor of about two by tighter selection criteria which lower the muon detection efficiency to about 80 % [49].

IFR Upgrade

The original production RPCs showed serious aging problems within one year, necessitating replacement of the forward endcap and barrel RPCs. More than 200 second-generation RPCs were installed in the forward endcap in 2002 to replace the original chambers. The barrel RPCs were replaced by layers of Limited Streamer Tubes (LSTs) [60] during shutdowns in 2004 and 2006. In the final IFR configuration shown in Figure 3.22, there were 12 layers of LSTs in the barrel sextants and 16 layers of second generation RPCs in the forward endcap. When some of the forward endcap RPCs were converted to avalanche mode in 2007, a different gas mixture was required. A new gas supply system, similar to the one designed for the LST chambers (89:3:8, CO_2:Ar:C_4H_{10}), was built and operated. We use run6 data as background in this thesis as run6 and run7 data were produced with the upgrade described above.

3.9 Trigger System

The events rate in a particle collision are enormous, which consists of desired and uninteresting events simultaneously. Since particle physics experiments are typically searching for "interesting" events (such as decays of rare particles) that occur at a relatively low rate, trigger systems are used to identify the events that should be recorded for later analysis. Trigger systems are necessary due to real-world limitations in data storage capacity and rates. Each particle detector has its own trigger design and features. The BaBar trigger system was designed for selecting events of interest with a high, stable, and well-understood efficiency while rejecting background events and keeping the total event rate under 120 Hz. It has two main level of trigger systems: level 1 (L1) trigger is based on charged tracks in the DCH above a preset transverse momentum, showers in the EMC, and tracks detected in the IFR (trigger data are processed by three specialized hardware processors); and level 3 (L3) trigger is based on software and keep the interesting events for further physics analysis.

Figure 3.23 shows the flow chart of L1 trigger operating in the BaBar experiment. Trigger data from DCH, EMC, and IFR are sent to global level 1 trigger (GLT) in every 134 ns. The drift chamber trigger uses both the timing and z coordinate information to reject background events. The GLT matches calorimeter clusters to drift chamber tracks for physics triggering, while also using IFR information for diagnostic triggering on $\mu^+\mu^-$ pairs and cosmic rays. The overall rate for Level 1 trigger is about 2.5 kHz at luminosity of 8×10^{33} cm$^{-2}s^{-1}$.

The L3 trigger software comprises event reconstruction and classification, a set of event selection filters, and monitoring. This software runs on the online Linux computer farm comprised of 28 Dell 1650 (Dual Pentium-III 1.4 GHz) capable of processing an individual event in about 4 ms. Here, quick reconstruction of DCH helices and EMC clusters is performed, and events are selected for logging. These events are then further grouped into runs and written to tape for long-term storage. Event rates are further reduced by about a factor of 10 by the Level 3 trigger, which also vetoes Bhabha scattering events. Apart from hosting the Level 3 trigger, the BaBar online event processing system as shown in figure 3.24 is also responsible for general monitoring tasks related to data acquisition, real-time data quality monitoring, detector calibrations performed regularly during normal detector operation, and running an event display that provides visual event reconstruction information.

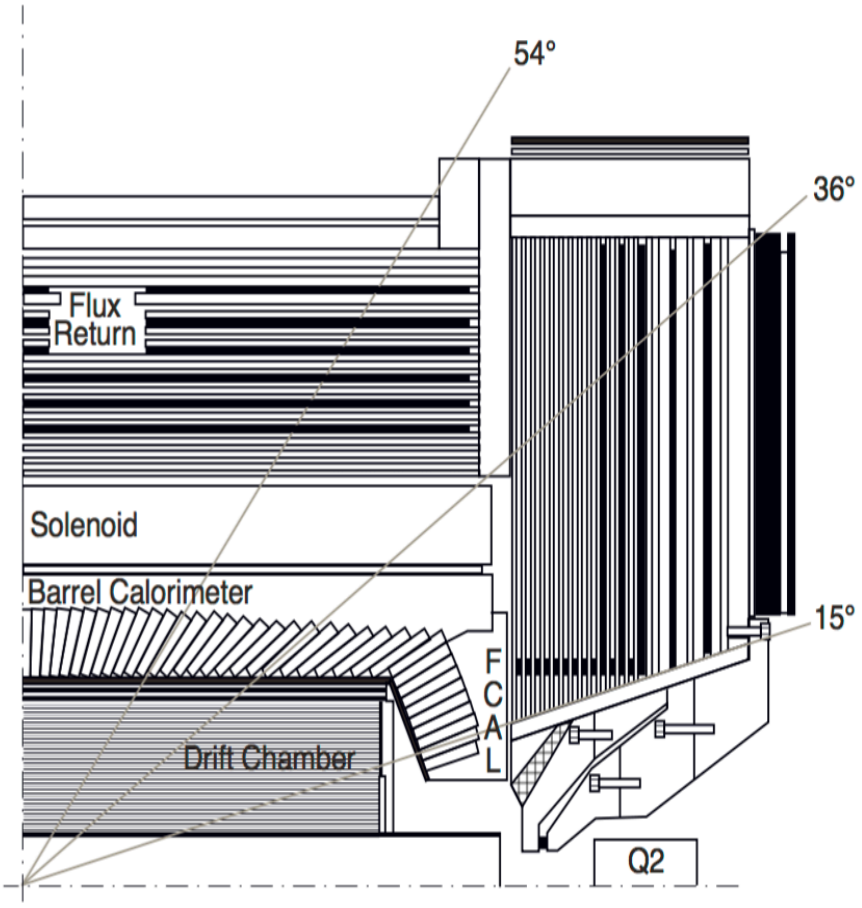

Figure 3.22: Final configuration of the IFR shown as a longitudinal section of the BaBar detector with details of the IFR barrel and forward endcap surrounding the inner detector elements. LST modules fill the gaps in the barrel, and RPC planes fill the forward endcap. The added brass and steel absorbers are marked in black [61].

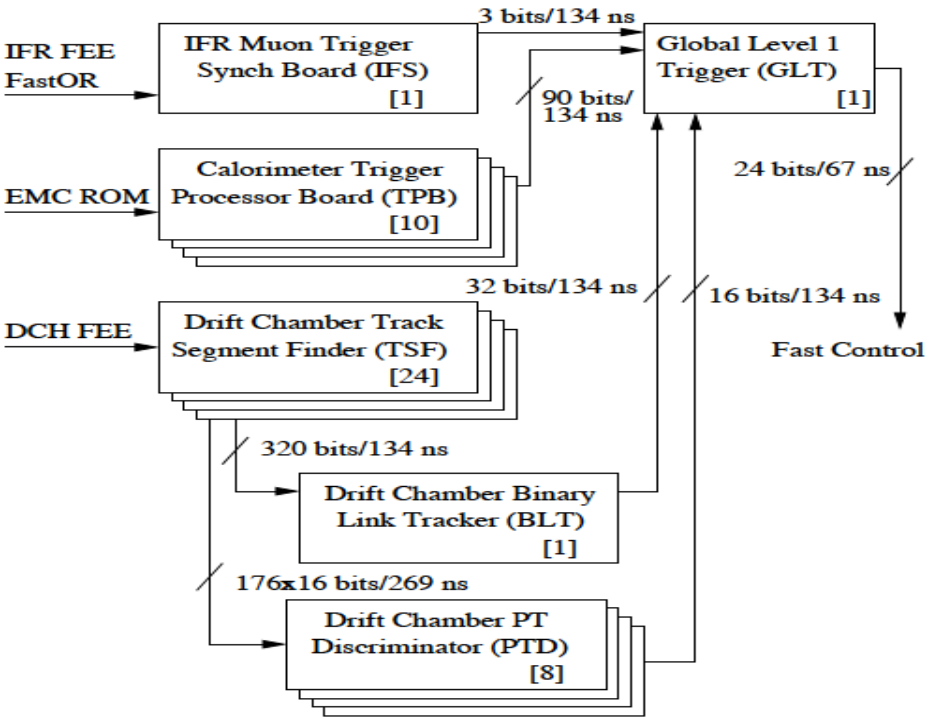

Figure 3.23: Simplified L1 trigger schematic [49].

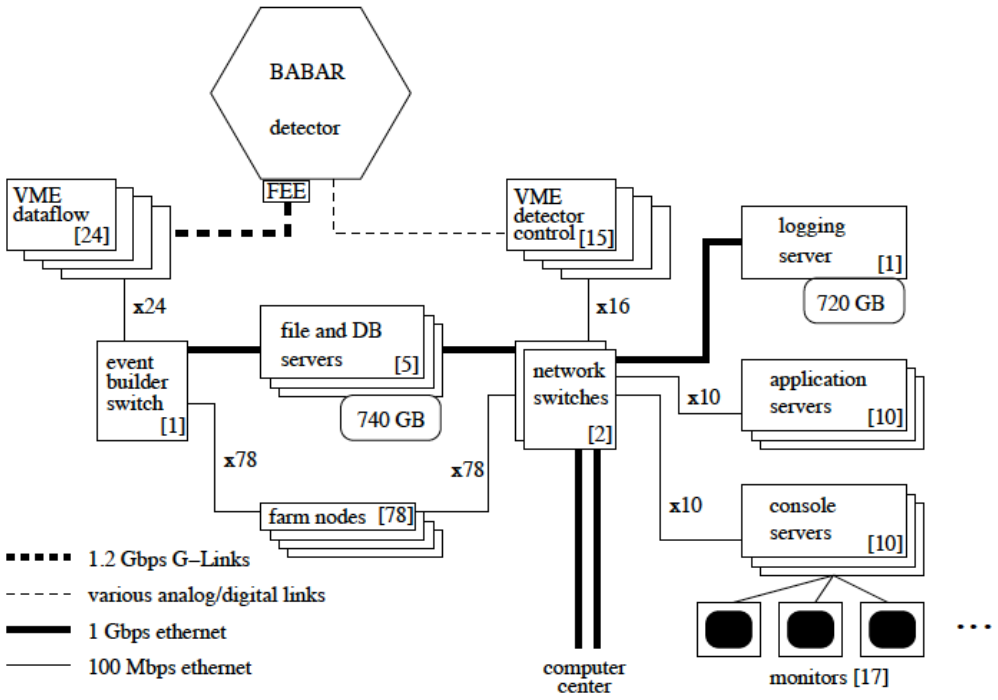

Figure 3.24: Physical infrastructure of the BaBar online system, including VME crates, computers, and networking equipment [49].

Chapter 4

Analysis Methodology

In a typical BaBar analysis the selection of signal candidates is performed in several stages. Since it is not efficient to process all available data for each analysis, a pre-selection, or skim, is performed at the first stage. The skim is usually designed to have a high signal selection efficiency while the background rejection is normally high but less important at this stage. Usually a single skim is used as a starting sample for the analysis.

The second selection stage is under control of the analyst. The optimization of this stage is performed on the skimmed dataset and depends on the physics goal of the analysis. Usually at the user level, two additional selections are performed. The first is a pre-selection defined to have a high signal selection efficiency with the goal of reducing the sample size so that the optimization process is faster. The second is the final selection from which the observables are obtained to measure the branching fraction.

Blind analysis [62] techniques have been employed in this search, to ensure the validity of a measurement with no experimenter bias. In this technique, a measurement performed without looking at the final answer, to avoid the expectation of a "right" answer from influencing the results and to remove the chance of "tuning" a selection to emphasize a statistical fluctuation. At BaBar once the blind analysis is completed, with selection cuts finalized, it will undergo an internal review. It is only after an internal committee has reviewed and approved of the analysis that the results are unblinded.

In this analysis, we search for the lepton flavour violating process $\Upsilon(3S) \to e^{\pm}\mu^{\mp}$ collected at $\sqrt{s} = 10.352$ GeV by the PEP-II storage ring at SLAC. The specific datasets and the corresponding Monte Carlo (MC) used in this analysis are summa-

rized in the following sections.

4.1 BaBar Data and Monte Carlo Samples

The BaBar event store contains two types of collections: real data collections and Monte Carlo simulated (SP, or Simulation Production) collections.

Real data begins as signals in the BaBar detector, and must pass through several stages before it is translated into a collection in the BaBar event store. The signals are digitized and reconstructed into tracks and clusters. Particle identification (ID) algorithms identify each track or cluster as a candidate for a given type of particle. Once the final-state particles are identified, they are used to reconstruct other particles in the decay chain.

Simulated data consists of generated particles, each with their own identities and four-vectors, which propagate through and leave signals in a GEANT4-simulated [63] BaBar detector. These signals have the same format as the signals left by real data in a real detector, so from that point on reconstruction is the same as for real data.

This analysis uses ROOT [64] tuples generated by using a system called Long Term Data Access (LTDA) [65]. LTDA is a project aimed to keep BaBar data, software and documentation available and in perfect working conditions for as long as possible (at least until 2018). It utilizes the analysis-52 software release and TauMiniUser package to produce the ntuples from the AllEvents skim (R24d-v05 skim cycle) [66]. Skims are subsets of the full data set that contain particular tag bits needed for a given analysis. The TauMiniUser package reads the input collections, process events that pass the channel specific background filters.

For Run 7, additional changes were made to significantly improve efficiency for detecting transitions between Upsilon states. For any event, information on whether or not individual trigger and filter lines are True or False can be found from the tag data.

4.1.1 DATA Sample

BaBar data was produced and collected during finite operational cycles known as runs that are classified and grouped according to specific detector and accelerator configurations. Each run is divided into unique run numbers which correspond to a small sub-collection of data. Detector upgrades and/or component failures produce

unique detector responses to be identified and documented. Additionally, large detector upgrades and changes in beam collision energies will correspond to divisions between the labelled operational runs. The largest data-taking run is called Run 5, which has a different detector configuration from Run 6 (CM energy corresponding to Υ(4S) events) and Run 7 (the production of Υ(2S) and Υ(3S)).

In this analysis, we use a small portion (3%) of main Υ(3S) data set as an unblinded sample which is roughly 0.93 fb^{-1} to validate the analysis procedure and agreement between data and MC events simulated by using Monte Carlo techniques. For the systematic study in the control sample and to estimate the background events, full data sets of Υ(3S) and Υ(4S) are used respectively. Table 4.1 shows the time integrated luminosities [45] of various datasets and the estimated number of Υ(3S) decays used in this analysis.

Table 4.1: Integrated luminosity and estimated number of Υ(3S) events of various data sets used in this analysis for the signal and the control sample. On means $\sqrt{s}$ is on the Υ resonances; off means $\sqrt{s}$ is slightly below the Υ resonances.

Data Set	$\sqrt{s}$ (GeV)	**Integrated** Luminosity (fb^{-1})	**Υ(3S) Number** $\times 10^6$
Υ(3S)On 3 % unblinded sample for analysis validation	10.3552	0.93 $\pm$ 0.006 $\pm$ 0.008	(4.06 $\pm$ 0.04)
Υ(3S)On for blinded analysis	10.3552	27.02 $\pm$ 0.027 $\pm$ 0.157	(117.7 $\pm$ 1.2)
Υ(3S)On Total	10.3552	27.96 $\pm$ 0.027 $\pm$ 0.168	(121.7 $\pm$ 1.2)
Υ(4S)On control sample	10.5782	78.31 $\pm$ 0.017 $\pm$ 0.348	0
Υ(3S)Off control sample	Below Υ(3S)	2.623 $\pm$ 0.008 $\pm$ 0.017	0
Υ(4S)Off control sample	Below Υ(4S)	7.752 $\pm$ 0.006 $\pm$ 0.036	0

4.1.2 Background and Signal Simulation Collections

Monte Carlo simulated events are used to estimate the cross sections of all background modes. They are also used to establish the selection criteria, agreement between data/MC and estimate the background rates, as well as provide a mechanism to determine efficiencies. In this analysis, simulated background processes consisting of continuum QED events [67], [68] and generic Υ(3S) decays, as well as signal Υ(3S)$\rightarrow$ $e^{\pm}\mu^{\mp}$ decays [69], are produced and analyzed to optimize the analysis procedure. The

GEANT4 [63] software is used to simulate the interactions of particles traversing the BaBar detector, which is described in detail elsewhere [70]. This analysis uses the following BaBar Monte Carlo background sources and signal MC as described below in the table 4.2.

Table 4.2: Monte Carlo background sources and signal MC for Υ(3S) at $\sqrt{s} = 10.36$ GeV and their generators.

Mode	**BaBar SP production**	**Generators**
$e^+e^- \to \mu^+\mu^-$	SP-3981-R7-Y(3S)-OnPeak-R24-v04	KK2F [71]
$e^+e^- \to e^+e^-$	SP-2400-R7-Y(3S)-OnPeak-R24-v04	BHWIDE [72]
$e^+e^- \to \tau^+\tau^-$	SP-3429-R7-Y(3S)-OnPeak-R24-v04	KK2F and TAUOLA
$e^+e^- \to uds$	SP-998-R7-Y(3S)-OnPeak-R24-v04	EvtGen [73]
$e^+e^- \to c\bar{c}$	SP-1005-R7-Y(3S)-OnPeak-R24-v04	EvtGen
Generic Υ(3S)	SP-8739-R7-Y(3S)-OnPeak-R24-v04	EvtGen
Υ(3S) $\to e^{\pm}\mu^{\mp}$	SP-8785-R7-Y(3S)-OnPeak-R24-v04	EvtGen

In order to produce comparison plots between data and simulated events, a scaling weight has to be applied. Using the number of events generated, the luminosity, and the estimated cross section the scaling weight is defined in equation 4.1 where σ_x is the production cross-section for a given process x, L^i_{int} is the integrated data luminosity for Run i, and $N^i_{gen,x}$ is the number of generated events of process x according to run i conditions. Table 4.3 shows the corresponding luminosities and cross sections [46] for different modes used in the 3 % unblinded sample analysis. Cross section from e^+e^- s-channel processes at the Born level are proportional to $\frac{1}{s}$. The reference article [46] for cross scetions provides the corresponding values, measured at Υ(4S) resonance, thus we have used cross sections with a correction factor equal to $(10.58)^2/(10.36)^2$ = 1.04 that corresponds to Υ(3S) (10.355 GeV) resonance energy.

$$w^i_{L_x} = \frac{\sigma_x \times L^i_{int}}{N^i_{gen,x}} \tag{4.1}$$

4.2 Analysis Strategy

The signature for Υ(3S) $\to e^{\pm}\mu^{\mp}$ events consists of exactly two oppositely charged primary particles: an electron, and a muon with momentum close to the beam energy

Table 4.3: Number of generated events and corrected Cross sections for the corresponding decay modes used in the 3 % unblinded sample analysis.

Mode	Number of Events (N_{GEN}) Υ(3S) On-Peak	**Cross-section** (nb)
$e^+e^- \to \mu^+\mu^-$	81.8×10^6	1.21
$e^+e^- \to e^+e^-$	83.8×10^6	41.60
$e^+e^- \to \tau^+\tau^-$	57.32×10^6	0.97
$e^+e^- \to uds$	41.7×10^6	2.17
$e^+e^- \to c\bar{c}$	55.9×10^6	1.35
$e^+e^- \to \Upsilon(3S)$	257.2×10^6	4.38

$E_B = \sqrt{s}/2$. Since we are searching for two lepton, directly decaying from Υ(3S) resonance, any secondary charged lepton from the τ (or μ) decay will considered as background events. These requirements on the identified particle types are necessary to suppress Bhabha and μ-pair backgrounds.

4.3 Main Sources of Background

The main source of background contribution to the eμ channel originates from τ-pair, μ-pair and Bhabha events. In τ-pair events, one of the τ decays to $\tau \to e\bar{\nu}_e\nu_\tau$ and the other decays to $\tau \to \mu\bar{\nu}_\mu\nu_\tau$. In such decays, the final state particles are eμ which are the daughter particles and considered as background. On the other hand, in μ-pair events, one of the muons is misidentified or decays in flight or an electron is generated in a material interaction. Bhabha events in which one of the electrons is misidentified as a muon is considered as background too.

Any decay from resonant Υ(3S) decays where there are two oppositely charged leptons in the final state would also be potential background. For example, backgrounds could arise from $\Upsilon(3S) \to l^+l^-$ (where l = e, μ, and τ) or if the Υ(3S) meson decays through an intermediate state, such as Υ(2S) and Υ(1S), and then the intermediate state decays to a pair of leptons and transition photons, then the final state particles would look the same as signal events. Note that the branching fraction of Υ (n = 1, 2, 3) $\to l^+l^-$ is about 2%. A simple list of some of the possible cascade decay channels of Υ(3S) can be found in Table 4.4.

Table 4.4: Listing of a few of the cascade decay channels

No.	Decay channels
1	$\Upsilon(3S) \rightarrow \gamma\gamma\ \Upsilon(2S)$ $\Upsilon(3S) \rightarrow \gamma\gamma\ \Upsilon(1S)$ $\Upsilon(2S) \rightarrow \gamma\gamma\ \Upsilon(1S)$
2	$\Upsilon(3S) \rightarrow \gamma\chi_{b_2}\ (2P)$ $\Upsilon(3S) \rightarrow \gamma\chi_{b_1}\ (2P)$ $\Upsilon(3S) \rightarrow \gamma\chi_{b_0}\ (2P)$
3	$\Upsilon(3S) \rightarrow \gamma\chi_{b_2}$ $\Upsilon(3S) \rightarrow \gamma\chi_{b_1}$ $\Upsilon(3S) \rightarrow \gamma\chi_{b_0}$
4	$\chi_{b_2}(2P) \rightarrow \gamma\ \Upsilon(2S)$ $\chi_{b_1}(2P) \rightarrow \gamma\ \Upsilon(2S)$ $\chi_{b_0}(2P) \rightarrow \gamma\ \Upsilon(2S)$
5	$\chi_{b_2}(2P) \rightarrow \gamma\ \Upsilon(1S)$ $\chi_{b_1}(2P) \rightarrow \gamma\ \Upsilon(1S)$ $\chi_{b_0}(2P) \rightarrow \gamma\ \Upsilon(1S)$
6	$\chi_{b_2} \rightarrow \gamma\ \Upsilon(1S)$ $\chi_{b_1} \rightarrow \gamma\ \Upsilon(1S)$ $\chi_{b_0} \rightarrow \gamma\ \Upsilon(1S)$

4.4 Particle Identification (PID) and Weighting

Particle Identification, referred to as PID, is the process by which information from different detector subsystems are joined to identify the type of charged particle passing through the detector at a given time. PID is essential to physics analyses, especially ones that involve flavour tagging or lepton flavour violating processes. Given the energy of the BaBar detector, only 5 charged particles live long enough to interact with the detector. These are the electron, muon, pion, kaon and proton. Each particle has a momentum given by: $\mathrm{p} = \mathrm{mc}\beta\gamma$ where $\beta = \frac{v}{c}$ and $\gamma = \frac{1}{\sqrt{(1-\frac{v^2}{c^2})}}$. The momentum of the particle is given by the tracking, and thus if a measurement of the velocity can be made, then the mass of the particle can be found. This is the idea behind PID at BaBar. However, instead of measuring β directly to form a PID hypothesis, gathered from all parts of the BaBar detector, primarily from DIRC and the tracking system.

Either for simple requirements or advanced technique methods, different levels of efficiency and rejection can be provided by modifying parameters and criteria. To make available the PID information in a simple way for different physics analyses, we

define " Selectors". A selector is a category related to a selection method with certain parameters and criteria. For each method you can have more selectors, generally 4, depending if we request a looser selection or a tighter selection. Each track satisfies or not a specific selector if it respects its criteria (binary information) and, if a track that satisfies a tighter selector, it satisfies also a looser one from the same method (i.e. selectors are nested). For each particle category (electron, muons, pions and kaons), the analyst could choose the best for his/her analysis without going deeply into the technical details of PID. Table 4.5 summarizes the multivariate techniques available for PID in BaBar.

Table 4.5: Different types of available selectors.

Selector	**Features**	**Identifying** Particles
KM	Based on error correcting output code and decision tree	π, K, p and $e^{\pm}$
Likelihood (LH)	Now usually replaced by KM selector	Hadrons and $e^{\pm}$
Decision Tree (BDT)	Offers μ/π discrimination	Hadrons, $e^{\pm}$, $\mu^{\mp}$
Example:muonBDT	offers substantially lower kaon-as-muon and proton-as-muon misID rates.	μ
Example:kaonBDT	Offers K/π discriminations	K
Neural Network (NN) Example:muNN	These are applied at different levels of particle efficiency.	$e^{\pm}$ and $\mu^{\mp}$

The best analysis sensitivity is likely to be achieved with eKM for electrons, muBDT for muons, piKM for pions, kaonBDT for kaons and pKM for protons. As stated earlier, PID selectors show a different efficiency for data and MC samples. To choose the appropriate PID selector, the multivariate technique allows us to measure 16 different selector combinations [76] implemented in this analysis. We checked the performance of each PID selectors as ($\frac{\epsilon_{SignalMC}}{\sqrt{Background}}$), and we find that the optimal selector, is SuperTightKMElectronMicroSelection (SuperTight) = 11 for electron [77] and BDTTightMuonSelection (BDTTight) =18 for muon [79]. Table 4.6 shows available PID setectors that can use in this analysis. Specific Variation of PID selector and outcome of using different PID combination details will found in the next section as shown in Figure 4.27 - 4.38. Brief descriptions of the electron and muon PID selectors ultimately used in the analysis are provided in the next two sections.

Table 4.6: Different PID selectors implemented in this analysis that can measure 16 sets of PID Combinations.

Electron PID	**Muon PID**
PidLHElectrons (tight)=5	BDTLooseMuonSelection (bdtLoose)=17
TightKMElectronMicroSelection=9	BDTTightMuonSelection (bdtTight)=18
VeryTightKMElectronMicroSelection (Very Tight)=10	BDTVeryTightMuonSelection (bdtVeryTight)=19
SuperTightKMElectronMicroSelection (Super tight)=11	BDTVeryTight MuonSelectionFakeRate (VeryTightFakeRate)=23

4.4.1 SuperTightKM Electron Selection

The multivariate electron identifier optimized for this analysis uses the Error Correction Output Code (ECOC) [78] multiclass classifiers for K, π, p and e particle identification in the KM selectors, originally developed by Kalanand Mishra (KM). The performance of this technique exceeds likelihood(LH) technique and vs matrix ECOC technique and therefore these selectors are in general the recommended ones for the Ultimate Particle ID. ECOC is a technique for combining multiple binary classifiers trained differently to form a multiclass classifier. This technique is the major part in KM selectors. We chose the exhaustive matrix shown in Table 4.7 as our indication matrix. It consists of 7 binary classifiers trained differently as shown by columns of Table 4.7. The algorithm we chose for each binary classifier was Bootstrap Aggregate Decision Tree.

Table 4.7: Exhaustive matrix is the indicator matrix used in KM selector [78]. Each entry indicates whether the training sample of the given type should be treated as signal(1) or background(-1).

Class	t_0	t_1	t_2	t_3	t_4	t_5	t_6
K	1	1	1	1	1	1	1
π	-1	1	-1	1	-1	1	-1
p	1	-1	-1	1	-1	-1	-1
e	1	1	-1	-1	-1	-1	-1

To classify a given track, we ask each classifier to give an output between -1 and 1 according to its own definition of signal and background. The output from binary

classifiers can be represented by a string of real number between -1 and 1 with length 7. We then compute the sum of squared difference (generalized hamming distance) of the output string with each row of Table 4.7. From this, we have 4 numbers. Each number corresponds to each particle hypothesis. We can select the hypothesis that gives the minimum hamming distance and called it our best guess. But, in BABAR we need multiple tightness levels for different demands from analyses. To supply multiple tightness levels in KM selectors, we noticed that selecting the minimum can be written as the comparison between the ratio and one shown in equation 4.2.

$$A < B \&\& A < C \rightarrow \frac{A}{B} < 1 \&\& \frac{A}{C} < 1 \tag{4.2}$$

We can generalize this relation by changing 1's to constants. This allows us to adjust those constants for different levels of tightness. This also creates an easy way for us to ensure the inclusiveness for tightness level: e.g. every track in satisfying the loose tightness should satisfy also the very loose tightness. So, for a given particle type selector we have 4 values to select on: hamming distance and 3 ratios. To make this clear, let Ha be the hamming distance between the output and the template for particle of type a. Table 4.8 shows which values are used to select which type of particle. It should be noted here that each of the variables, placed on the selection has intuitive meanings. The hamming distance of the particle itself represents how likely it is that this track is that type of particle. The three ratios represent how sure we are that it's not another type of particle. This interpretation is also very useful in tuning. Let us suppose we are looking at kaon and the pion as kaon misidentification rate is too high. It's quite obvious that the value we should tighten the selection on is either $\frac{H_\pi}{H_K}$ or H_K.

4.4.2 Decision Tree Algorithm and BDTTight Muon Selector

A decision tree is a decision support tool that uses a tree-like graph or model of decisions and their possible consequences, including chance event outcomes, resource costs, and utility. Decision tree is a representation of displaying an algorithm, which uses by the BaBar collaboration to help identify a strategy to reach in decision analysis about PID selectors.

A decision tree is a flowchart-like structure in which each internal node represents a "test" on a variable (it goes through all variables and find best variable and value to split events, then each of the two subsets repeat the process), each branch represents

Table 4.8: The selection cirteria for each type of particle in KM selector.

Particle Type	**Ratio 1**	**Ratio 2**	**Ratio 3**	**Ratio 3**
K	H_K	$\frac{H_\pi}{H_K}$	$\frac{H_p}{H_K}$	$\frac{H_e}{H_K}$
π	H_π	$\frac{H_K}{H_\pi}$	$\frac{H_p}{H_\pi}$	$\frac{H_e}{H_\pi}$
p	H_p	$\frac{H_K}{H_p}$	$\frac{H_\pi}{H_p}$	$\frac{H_e}{H_p}$
e	H_e	$\frac{H_K}{H_e}$	$\frac{H_\pi}{H_p}$	$\frac{H_p}{H_e}$

the outcome of the test, and each leaf node represents a class label (decision taken after computing all variables). The paths from root to leaf represent classification rules. In contrast to other PID selectors algorithm (for example, Neural Nets) process, its easy to understand (at each node) how a decision is derived. In this process, no event is removed completely, no information is lost which is equivalent to optimizing a conventional "cuts".

The muon selector that we used in our analysis is based on a Bagging Decision Tree (BDT) algorithm. A brief description of this muon selector is provided here.

StatPatternRecognition (SPR) is a pattern-recognition software package developed by Ilya Narsky [80]. Preliminary investigation of using SPR for muon identification indicated that it held the promise of noticeably exceeding the performance of the neural network. SPR Bootstrap Aggregating Decision Trees (BDT) [80] were chosen for the muon ID task because their performance exceeded other tools in SPR. A decision-tree algorithm involves splitting training data into rectangular nodes. All possible binary splits of all input data in each dimension are considered to find the split that produces the highest figure of merit. After the split, the algorithm repeats the process recursively on the two nodes that resulted from the first split. If the figure of merit of at least one of the resulting nodes after a split is not greater than the previous figure of merit, the split is rescinded, and the node becomes a terminal node. If it has more signal than background events, it is labelled as a signal node; otherwise, it becomes a background node. In addition, the user building the tree can specify a minimum node size, so that splitting ceases when a node reaches the minimum size.

Various figures of merit can be used. The negative Gini index is used by default.

It is equal to -2pq, where p and q = 1 - p are the fractions of correctly and incorrectly classified events in each node.

Bootstrap aggregating involves training many trees on different subsets of the training data. Each subset is a random draw from the full training data set. After training, data are classified by a majority vote of the trained trees.

For the task of muon identification, the SPR BDT algorithm is trained on a set of muon and pion tracks. The muon and pion training data are divided into 720 bins by p, polar angle θ, and charge and then any excess muons or pions are discarded so that each bin holds equal numbers of muons and pions. This process allows p, θ, and charge to be used by the tree as classification variables without biasing the classification with regard to these variables; that is, the tree will not separate muons from pions purely based on p, θ, or charge. The following list shows the 30 variables used for classification of the tracks:

- momentum p
- polar angle θ
- charge
- YYYYMM date - month and year of the track
- IFR Variables
- ifrns - number of strips in IFR cluster
- χ^2_{mat} (ifrmatchchi2) - χ^2 between the IfrKalman track and cluster
- χ^2_{fit} (ifrfitchi2) - χ^2 for the cluster w.r.t. 3rd-order polynomial fits in both views
- T_C (ifrcont) - continuity of IFR hits in the 3-D IFR cluster
- σ_m (ifrsigmu) - truncated sigma of strip multiplicity
- λ_{meas} (ifrmeasintlen) - number of measured interaction lengths
- $\triangle\lambda$ (deltalambda) - difference between the expected number of interaction lengths and the measured number
- ifrcrackphi - distance of the track from the nearest crack in the IFR detector; zero for tracks that go through a crack

- EMC Variables

- E_{cal} (ecal) - EMC energy, corrected for leakage of photon showers
- lmom - lateral moment of the EMC shower
- zmom20 - Zernicke 20 moment of shower shape
- zmom42 - Zernicke 42 moment of shower shape
- ncry - number of crystals in the EMC bump
- s1s9 - energy of centroid crystal divided by the energy of the nine nearest crystals
- s9s25 - energy of nine nearest crystals over the energy of the twenty-five nearest crystals
- secmom - smoothness of shower in theta and phi
- emcdepth - depth of the shower in the EMC
- ecaldivp - ecal divided by p

- DCH Variables

- dEdxdchPullmu the ratio of the expected dE/dx for a muon in the DCH over the measured dE/dx, adjusted to make a Gaussian centered at 0
- ndch - number of hits in the DCH
- lhit - last layer hit in the DCH (helps detect decays in flight)

- DRC Variables

- drcmuprob - probability for the track to be a muon, based upon DRC data
- smsdrcmuprob - probability track is a muon, as computed by the SMS selector
- drcpiprob - probability track is a pion, based upon DRC data
- drckprob - probability track is a kaon, based upon DRC data
- nphot - number of DRC photons

The result of the training is one SPR BDT classifier. Tracks can be passed to the classifier, and it outputs a quantity that varies from 0 for pions to 1 for the tracks that are the most likely to be muons. Figure 4.1 shows the performance of the standard selector criteria that have muon efficiency targets.

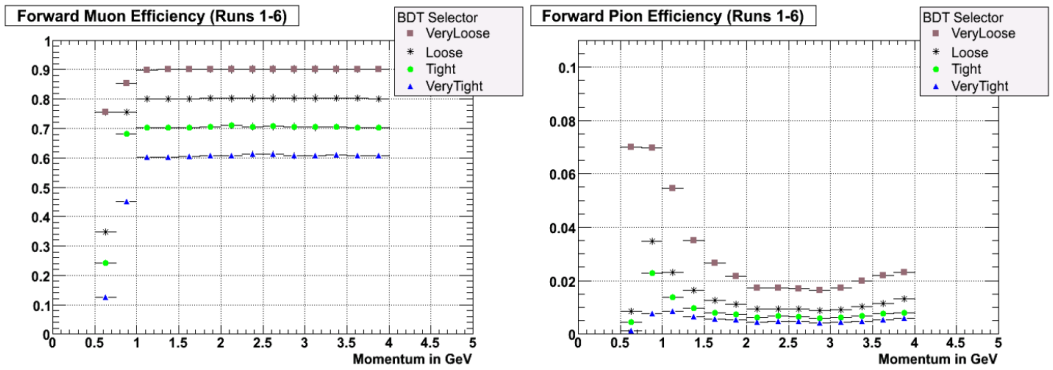

Figure 4.1: BDT selector efficiency vs. lab momentum in GeV/c for the forward endcap. Muon efficiencies are on the left, pion efficiencies on the right. These plots only cover Runs 1-6, but the addition of Run 7 would not noticeably change the plots [79].

The choice of PID selectors was guided by BaBar's recommendations only as we explained above. Thus in the analysis, we check the electron bit first and declare an "electron track" if it passes the electron selector. Remaining tracks that pass the muon selector are identified as "muon tracks". As such, PID efficiencies from BaBar's PidTables package were used to correct for known differences between data and simulation. The weight applied to all simulated events is the product of the weights for the electron track and the muon track.

$$w_{PID} = w^{e}_{PID}(q, p, \theta, \phi) \times w^{\mu}{}_{PID}(q, p, \theta, \phi) \tag{4.3}$$

where q is the charge of the particle (+1 or -1), p is the magnitude of its momentum with polar angle θ, and azimuthal angle ϕ.

4.5 Selection Criteria

Selection proceeds in two stages. First a background filter has used for preselection to select eμ events efficiently. Then the analyst taken over the control on preselected

data. In the second stage, to select signal, separating and reducing the background, we employed multivariate techniques [74] in Particle Identification (PID). In this analysis, we used a multivariate PID system which allow us to optimize the PID selectors. In addition to the multivariate PID system, we also use specific cuts using the tracking and calorimeter systems. Details of these two stages are described in the following sections.

4.5.1 Pre-Selection

The purpose of preselection is mainly to reduce the samples removing most of the background events like Bhabha, dimuon, uds and $c\bar{c}$ applying requirements on basic event variables like numbers of tracks and calorimeter clusters, shape and thrust magnitude. In this analysis, we use a specific background filter called BGFEMuSelector [75]. The performance of BGFEMuSelector was checked by processing 103000 events in signal MC. The selector is 80.2% efficient for selecting the $\Upsilon(3S) \rightarrow e^{\pm}\mu^{\mp}$ decay mode. The TauMiniUser package reads the input collections and process events that pass (BGFEMuSelector) background filters. The selector sets the BGFEMu flag using reconstuction level quantities for events passing the following selection as stated below: these flags are set after part of the reconstruction code has run on the event. They are designed to prevent overloading the prompt reconstruction system. An event must have one of these flags set true in order to be fully reconstructed and written to the Event Store. Each such flag is True only if the line contributed to the final decision to keep the event, i.e., it is after any prescaling. Overall, all events are required to have exactly two tracks in GoodTracksLoose, one in each hemisphere. The event must pass either the drift chamber or electro-magnetic calorimeter level 3 triggers (L3OutDch or L3OutEmc). These selection criteria supress Bhabha, μ-pair and two-photon processes as well as beam-gas interactions.

- Distance of closest approach of any track vertex with respect to the beam spot in Drift Chamber in the x - y plane < 1 cm and in the z plane < 4 cm;
- Number of hits in the Drift Chamber > 0. Transverse Momentum $p_{\perp} > 100$ MeV;
- Total charge of the 2 tracks $== 0$;
- Polar angle of the two tracks: $2.8 < (\theta_1 + \theta_2) < 3.5$;

- Sum of momentum of the two tracks $|P_1| + |P_2| > 9$ GeV/c;
- Exactly one electron of two tracks defined by $E_{CM}/P_{CM} > 0.8$;
- The acolinearity angle associated with two tracks < 0.1 radians in CM.

Charged particles are reconstructed as tracks in the Drift Chamber (DCH) and Silicon Vertex Tracker (SVT) as discussed details in the previous chapter. First, a track should have a minimum number of hits in the detector so an accurate momentum measurement can be made. The two main variables used to identify well measured tracks (Reconstructed Good Tracks) are the number of DCH hits used in the track fit and the transverse momentum ($P_\perp$) of the track. Tracks that have large values for these variables will have penetrated further into the detector and will leave enough information to have a suitable fit of their trajectory. The second requirement is that a track originate from the luminous region, where the e^+e^- beams collide. This requires the track reconstructed in the detector to extrapolate close to the beamspot. Tracks resulting from interactions of the beams with residual gas in the PEP-II vacuum system, or with the beampipe's beryllium walls, are eliminated. Cuts on the track's distance of closest approach (DOCA) to the beamspot are made in both the plane transverse to the beam direction (DOCAxy) and along the direction of beam travel (DOCAz), conventionally termed the xy plane and the z direction. The two separate cuts are made because the luminous region is significantly larger in z than in the xy directions. The final requirement is that a track should not be near the edge of the detector's active area so as to avoid any edge effects at the detector boundaries where efficiencies for reconstructing a track can rapidly vary. Because the resolution on a track's parameters is not perfect, it can be difficult to understand efficiency of detection in these areas. If the Primary tracks are not electron or muon but other charged particles say τ, then the τ must decay into an odd numbers of particles which impart the momentum. That means sum of two primary tracks' momenta would drop down less than 9 GeV. Furthermore, BGFElMuSelector, requires small acolinearity angle between the two tracks shown in figure 4.2. Acolinearity is used as a direct measurement of beam energy loss.

Most of the beam energy loss is due to initial state radiation, but non-negligible contribution result from bremsstrahlung and from the initial beam energy difference.

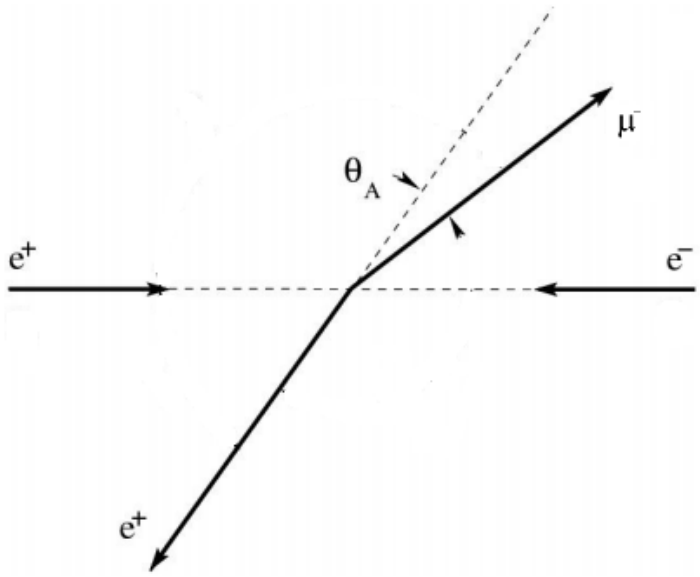

Figure 4.2: Acolinearity angle θ_A between two tracks.

4.5.2 Final Selection Criteria

We are now on the second stage of selection. Different selection criteria are applied on the preselected events to eliminate background events and to keep the signal selection efficiency high at the same time. Figure 4.3 shows the log distribution of $e^{\pm}\mu^{\mp}$ mass in the preselected events before any user defined selection criteria applied. To select the real $e^{\pm}\mu^{\mp}$ signal, we have implemented several selection criteria to different kinematic variables such as lepton momentum, angle btween two tracks etc.

The first selection is based on PID selection which requires all events to have exactly two tracks of opposite charge, both consistent with originating from the primary interaction point. The event must pass either the drift chamber or electromagnetic calorimeter level 3 triggers (L3OutDch or L3OutEmc). An electron track must pass the SuperTightKMElectronMicro selection but not BDTTightMuon selection. Also a muon track must pass the BDTTightMuon selector but not SuperTightKMElectronMicro selection. In order to ensure a pion or kaon track not to mis-selected as a charged lepton both electron and muon tracks must not pass veryLoosePion and veryLooseKaon selectors. Purpose of this cut is to ensure two tracks would emerged as e and μ in the final state. It also suppressed misID rates as pion-as-electron tracks.

The next selection criteria is applied on the distribution of polar angle of electron

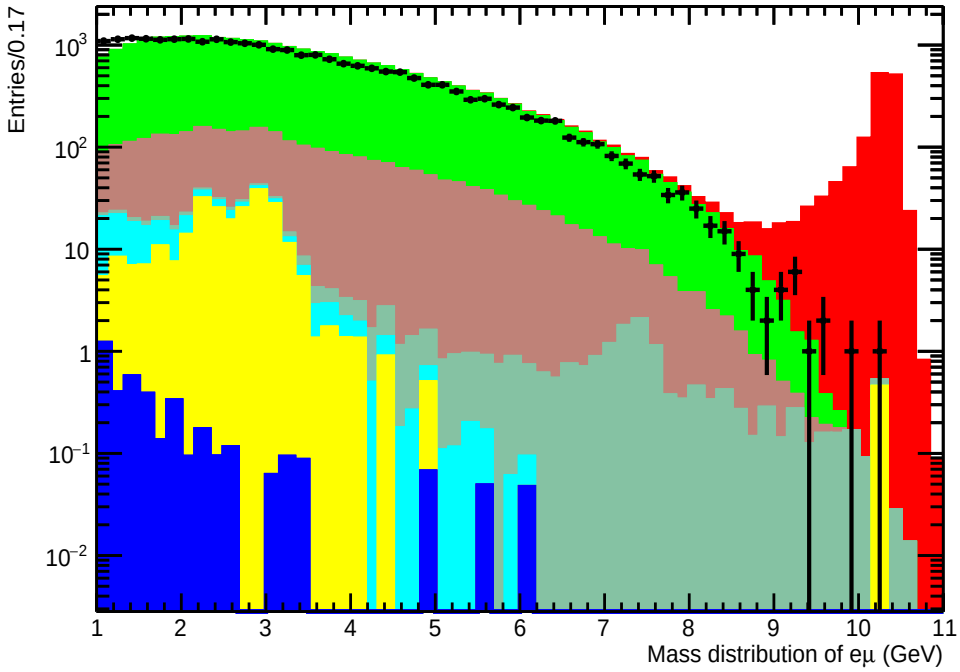

Figure 4.3: Distribution of $e^{\pm}\mu^{\mp}$ mass before applying any user defined selection criteria, only preselection criteria has applied. The green histogram is the continuum τ-pair production, the sea-green histogram is μ-pair production, the yellow histogram is the Bhabha, and the brown histogram represents the generic Υ(3S) MC, the royal blue histogram represents uds, the cyan histogram represents $c\bar{c}$ while the red histogram is the signal MC. The black line with error bars represents Υ(3S) data for 3 % unblinded sample luminosity.

and muon tracks. The purpose of this cut is to ensure selected events to fall within the angular acceptance of the EMC. The angular EMC acceptance is defined by approximately $24^\circ < \theta_{Lab} < 130^\circ$, where θ is the polar angle of lepton tracks in the lab frame. This selection helps suppress continuum (such as μ-pair) backgrounds. Figures 4.4 and 4.5 show the distributions of the polar angle of lepton tracks in (N-1) plots. (N-1) plot is a specific type of plot where all other selection criteria have been imposed except the "current" selection criteria.

The next selection criteria is applied on the lepton momentum planes. If the Primary tracks are not electron or muon but other charged particles say τ, which further decayed to an odd number of particles that look like the same as signal events with some missing energy, on those case the primary lepton momentum imparted to

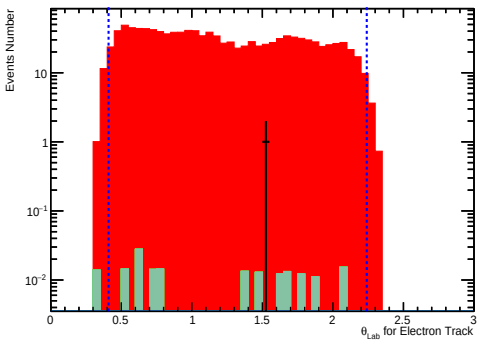

Figure 4.4: Distribution of polar angle for electron tracks at lab frame. The dotted blue line showed two edges where the selection cut is applied. The sea-green histogram is the background comes from μ-pairs, while the red histogram is the signal MC and the black line with error bars represents Υ(3S) 3 % unblinded data sample that we used to estimate background events.

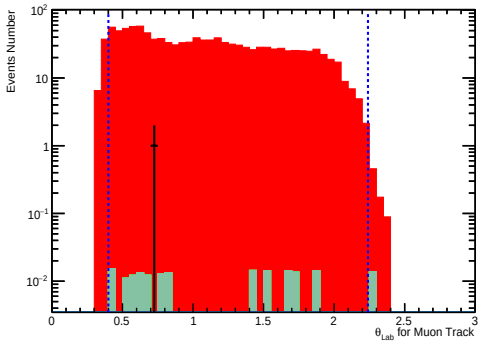

Figure 4.5: Distribution of polar angle for muon tracks on the lab frame. The dotted blue line showed two edges where the selection cut is applied. The sea-green histogram is the background comes from μ-pairs, while the red histogram is the signal MC and the black line with error bars represents Υ(3S) 3 % unblinded data sample that we used to estimate background events.

its daughter particles is less than original track momentum. For example, in τ-pair events, one of the τ decays to $\tau \rightarrow e\bar{\nu}_e\nu_\tau$ and the other decays to $\tau \rightarrow \mu\bar{\nu}_\mu\nu_\tau$. We will use these background events as a control sample to study efficiency and data MC agreement in the next chapter. This selection criteria is also intended to suppress those particles that are not directly decayed from the resonant Υ(3S). The lepton momenta must satisfy the following condition which is defining a circle of radius of 0.1 centered at (1,1) in the $\frac{p_e}{E_{Beam}}$ vs $\frac{p_\mu}{E_{Beam}}$ plane. Figure 4.6 shows the circle formed by the MC signal in the lepton momemtum planes.

Figure 4.7 shows the radius of the circle formed in the lepton momentum planes. The cut is applied in such way that it will only take those events that satisfy the following condition as described in equation 4.4. This cut is the most effective selection criterion that is able to eliminate most of background events.

$$(\frac{p_e}{E_{Beam}} - 1)^2 + (\frac{p_\mu}{E_{Beam}} - 1)^2 < 0.01 \tag{4.4}$$

where, $E_{Beam} = \frac{\sqrt{s}}{2}$.

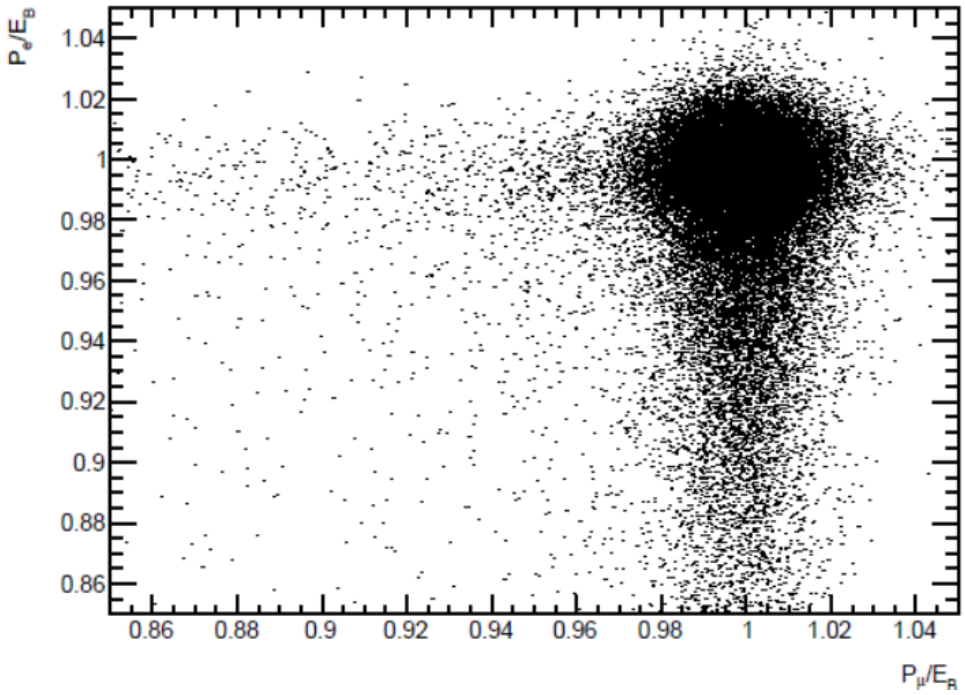

Figure 4.6: MC signal forms a circle on the $\frac{p_e}{E_{Beam}}$ vs $\frac{p_\mu}{E_{Beam}}$ lepton momentum planes.

The next selection applied to suppress further background events mainly coming from the Bhabha and μ-pair which are emerged back to back. We require the angle between the two lepton tracks must satisfy $\theta_{12}^{CM} > 179^\circ$ to ensure they are emerged as back to back. θ_{12}^{CM} is the quantity that provides the angle between 2 tracks in the CM frame. Figure 4.8 shows the distribution of angle between 2 tracks in (N-1) cut presentation.

For reducing continuum background from μ-pair and suppress Bhabha events in which an electron is misidentified as a muon, because, e.g. it misses a crystal on the Electromagnetic Calorimeter (EMC), the primary muon candidate must deposit at least 50 MeV in the EMC. Figure 4.9 shows the distribution of energy deposited at EMC by the muon track.

The following summerizes the user defined selection criteria as explained above:

- The event must have exactly 1 electron and 1 muon in the final state, one in each hemisphere, must pass L3 Trigger (L3OutDch or L3OutEmc)

  e$_{PID}$: An electron must pass the SuperTightKMElectronMicroSelection

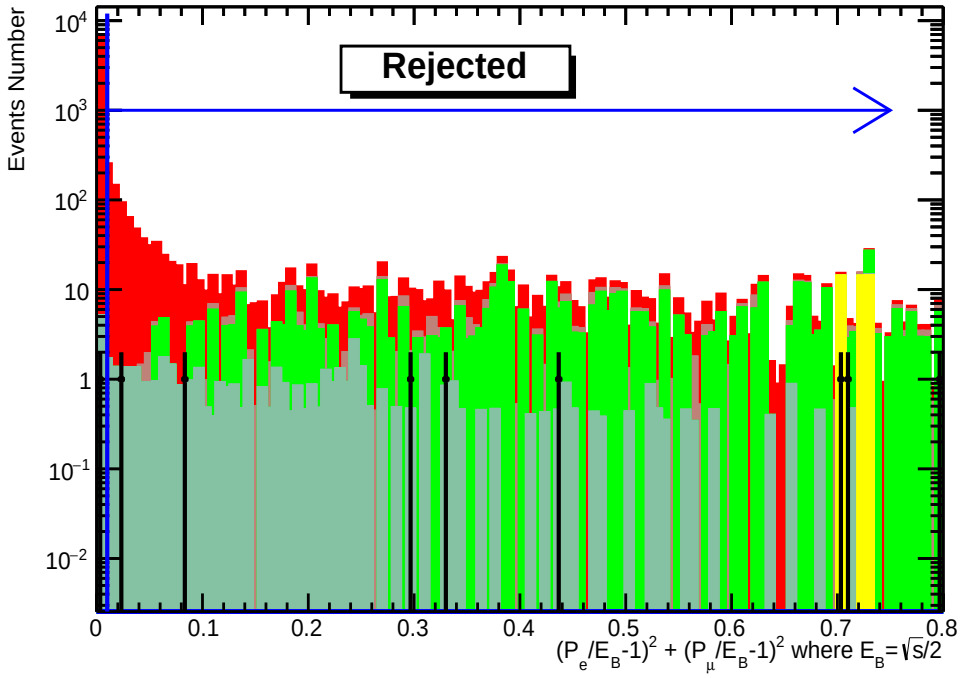

Figure 4.7: Radius of the circle in the lepton momentum planes in (N-1) cuts. The broken blue line indicates that selection criteria is applied on 0.01 at x-axis to eliminate the background events. The green histogram is continuum τ-pair production, the sea-green histogram is μ-pair production, the yellow histogram is bhabha, and the brown histogram represents the generic $\Upsilon(3S)$ MC while the red histogram is the signal MC. Data for 3% unblinded sample are the data points.

(Super tight) selector but not BDTTightMuonSelection (bdtTight).

μ_{PID}: An muon must pass the BDTTightMuonSelection (bdtTight) but not SuperTightKMElectronMicroSelection (Super tight) selector.

Both electron and muon tracks must not pass veryLoosePion and veryLooseKaonselectors.

- Tracks must fall within the angular EMC acceptance: $24° < \theta_{Lab} < 130°$.
- The angle between the two lepton tracks must satisfy $\theta_{12}^{CM} > 179°$ to ensure they are emerged as back to back.
- Energy deposit by Muon track on the Electromagnetic Calorimeter should be greater than 50 MeV.

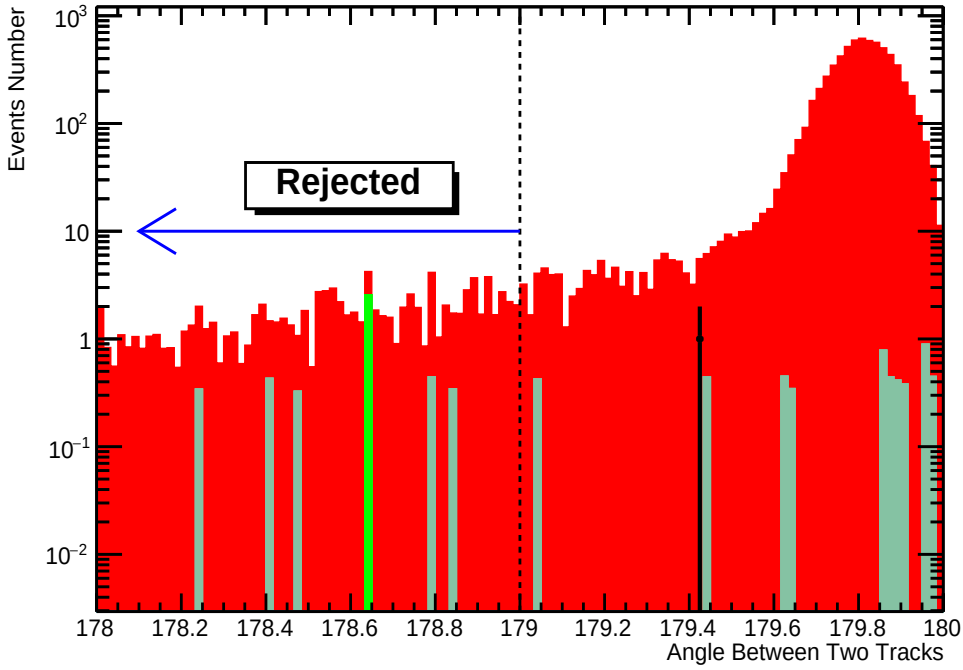

Figure 4.8: Distribution of angle between 2 tracks in (N-1) cut presentation. The green histogram is continuum τ-pair production, the sea-green histogram is μ-pair production, and the brown histogram represents the generic Υ(3S) MC while the red histogram is the signal MC.

- The lepton momenta must satisfy the following condition which is defining a circle of radius 0.1 centered at (1,1) in the $\frac{p_e}{E_{Beam}}$ vs $\frac{p_\mu}{E_{Beam}}$ plane: $(\frac{p_e}{E_{Beam}} - 1)^2 + (\frac{p_\mu}{E_{Beam}} - 1)^2 < 0.01$ where, $\mathrm{E}_{Beam} = \frac{\sqrt{s}}{2}$.

After including all selection requirements, signal efficiencies determined from signal MC is $0.2342 \pm 0.0013_{STAT}$, the number of events passing the selection criteria is 1 for the 3 % unblinded sample in Υ(3S) dataset. No events from Bhabha, τ-pairs, $c\bar{c}$ and uds MC sample passed the selection. The number of the Bhabha MC generated events is much lower than the data because the MC is not expected to acurately to describe the data. The remaining contribution in background only came from μ-pair events which are kinematically identical to the signal events, kinematic discrimination between signal and background processes is not possible. Therefore the rates for the background processes must be determined using control samples and subtracted to determine the event rate due to the signal process. After including all selection

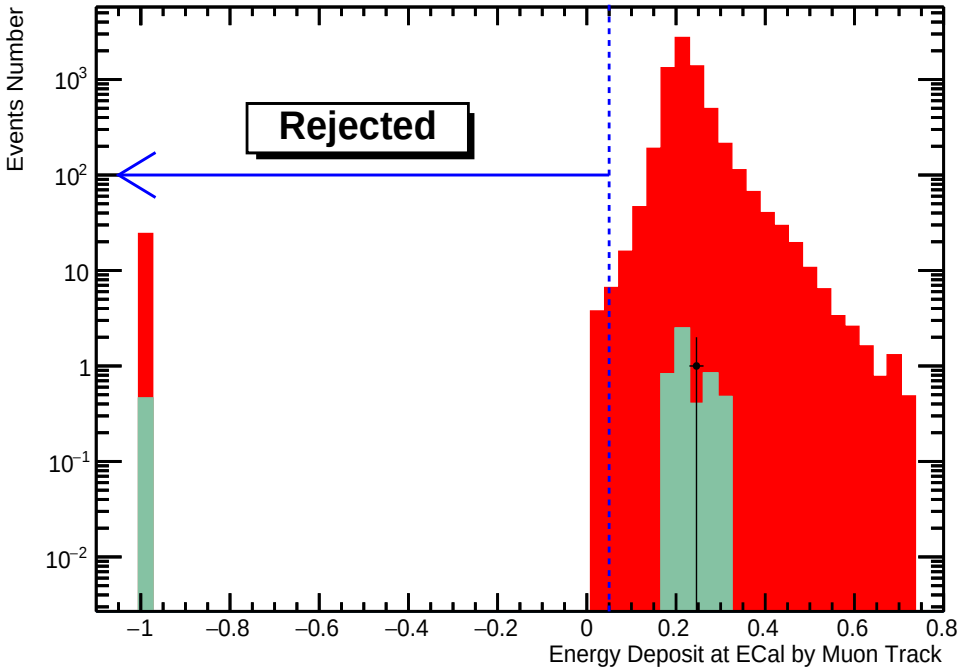

Figure 4.9: Distribution of energy deposited at EMC by the muon track. The broken blue line indicates that selection criteria is applied at 50 MeV in the x-axis. The sea-green histogram is μ-pair production, while the red histogram is the signal MC.

requirements, we also checked the difference between electron and muon momenta in CM and found the radiative losses are dominated by electrons, as expected as seen by the asymmetric tail of the $p_\mu - p_e$ distribution shown in Figure 4.10.

The total number of generated events, the pre-selected events passing through BGFEMu and survived events passing through the user defined selections are summarzied in Tables 4.9, 4.10, and 4.11 for the main simulated background MCs, Signal MC, and Data. The value of the distribution of e-μ mass differs slightly between $\Upsilon(4S)$ and $\Upsilon(3S)$ data, as expected for backgrounds at two slightly different values of $\sqrt{s}$. There are no cuts on $\sqrt{(s)}$, so it is valid to use the $\Upsilon(4S)$ data as a control sample. Also, a correction factor has applied to the number of events for the data $\Upsilon(4S)$On and $\Upsilon(4S)$Off in the Table 4.10 and 4.11, respectively, to account for the slightly different cross sections between the $\Upsilon(4S)$ data and $\Upsilon(3S)$ data as well as the different integrated luminosities of the samples.

The total number of generated events, the pre-selected events passing through

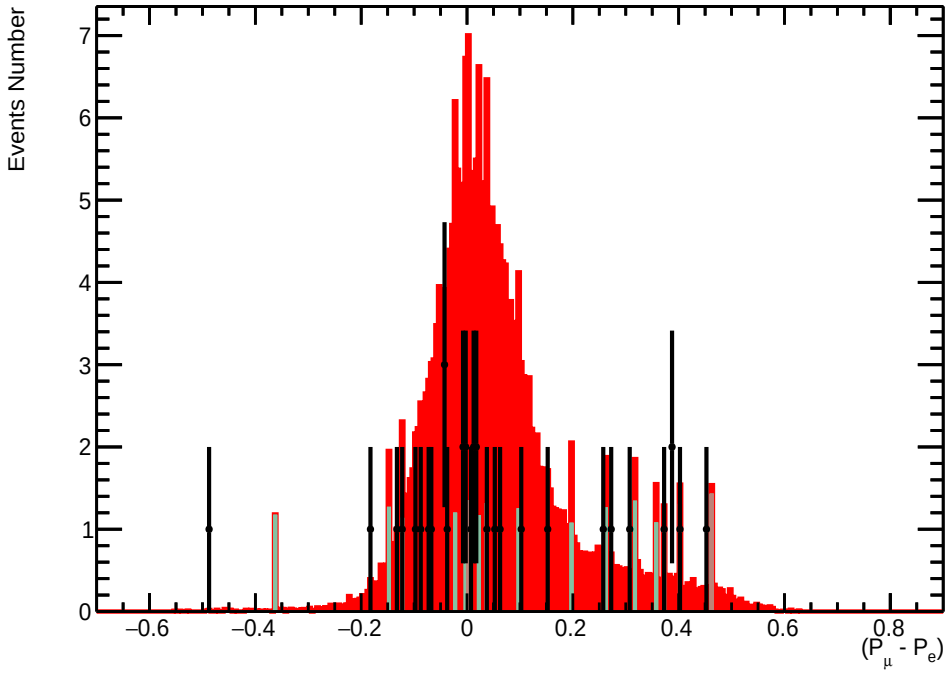

Figure 4.10: Difference between electron and muon momenta in CM after applying all selection. The sea-green histogram is μ-pair production, the tan coloured histogram represents Υ(3S) MC, while the red histogram is the signal MC and the black line with error bars represents the Υ(4S) data sample that is used to estimate background.

BGFEMu selector are summarized in Table 4.9, for the main simulated background MCs, Signal MC and Data control samples. The pre-selected events passing through BGFEMu selector and (N-1) cuts are summarized in Table 4.10, for the main simulated background MCs, Signal MC and Data for the 3 % pre-blinded sample. Table 4.11 summarized the pre-selected events passing through BGFEMu selector and (N-1) cuts for the main simulated background MCs, signal MC and data sample.

Table 4.9: The total number of generated events, the pre-selected events passing through BGFEMu selector in simulated background MCs, Signal MC and control samples are summarized. These events numbers represents the real event numbers survived in the respective luminosities as mentioned in the top row.

Selection	**MC Signal**	**Survived Events on MCs**				$\Upsilon(4S)$**Off**	$\Upsilon(4S)$**On**	$\Upsilon(3S)$**Off**
		$\mu\mu$	$\tau\tau$	Υ**(3S)**	**Bhabha**	7.75 fb^{-1}	78.31 fb^{-1}	2.62 fb^{-1}
N_{Gen}	103000	81854000	57322000	257432000	368000000	115335554	1262797446	89535261
Pre-Selec.	82612	57462380	30778350	16222480	72337260	43736310	429768800	24956320
PID-Selec.	24254	12	0	0	0	1	41	0
Lep. Mom.	27653	137	211	188	3	61	734	28
Back to back	24744	23	1	1	0	19	105	5
Accept. on EMC	25704	13	0	0	0	2	39	0
Energy on EMC	24234	13	0	0	0	1	49	0
All Cuts	24127	12	0	0	0	1	34	0

Table 4.10: The survived events shown here are the equivalent numbers for the pre-blinded sample for simulated background MCs, Signal MC, and control samples. The numbers are shown in the format of (N-1) cut which represents the number of those events where every other cuts was applied except that specific selection criteria. The second column here represented the efficieny of Signal MC and the uncertainties are statistical uncertainty only. Data $\Upsilon(4S)On$ in the 8th column is used for estimating background events. Data $\Upsilon(3S)Off$ and $\Upsilon(4S)Off$ are the control samples used to measure the continuum background events estimated from $\Upsilon(4S)On$ data. The events in the 10th column represents the numbers survived in pre-blinded sample. Event numbers shown on the On and Off peak resonance of control sample data are corrected for the different integrated luminosities as well as slightly different cross sections arising from the difference in CM energy.

Selection	**Efficiency** $\varepsilon_{e\mu}$	**Survived Events on MCs**				$\Upsilon(4S)$**Off**	$\Upsilon(4S)$**On**	$\Upsilon(3S)$**Off**	$\Upsilon(3S)$**On**
		$\mu\mu$	$\tau\tau$	Υ**(3S)**	**Bhabha**				
Pre-Selec.	82612	782091	460416	246347	20702657	5247003	5120346	8848409	8271184
PID-Selec.	0.2355 ± 0.0013	0.16 ± 0.05	0	0	0	0.13 ± 0.13	0.51 ± 0.08	0	1
Lep. Mom.	0.2684 ± 0.0012	1.86 ± 0.16	19.17 ± 0.54	2.90 ± 0.21	0.86 ± 0.50	7.61 ± 0.97	9.07 ± 0.36	9.93 ± 1.87	12
Back to back	0.2402 ± 0.0013	0.31 ± 0.04	0.12 ± 0.04	0.02 ± 0.02	0	2.37 ± 0.57	1.30 ± 0.13	1.77 ± 0.79	1
Accept. on EMC	0.2495 ± 0.0013	0.18 ± 0.05	0	0	0	0.25 ± 0.18	0.48 ± 0.08	0	1
Energy on EMC	0.2452 ± 0.0013	0.18 ± 0.05	0	0	0	0.13 ± 0.13	0.61 ± 0.09	0	1
All Cuts	0.2342 ± 0.0013	0.16 ± 0.05	0	0	0	0.13 ± 0.13	0.42 ± 0.07	0	1

Table 4.11: The survived events shown here are the equivalent numbers for data, after unblinding the data sample for simulated background MCs, Signal MC, and control samples. The numbers are shown in the format of (N-1) cut which represents the number of those events where every other cuts was applied except that specific selection criteria. The second column here represented the efficieny of Signal MC and the uncertainties are statistical uncertainty only. Data $\Upsilon(4S)On$ in the 8th column is used for estimating background events. Data $\Upsilon(3S)Off$ and $\Upsilon(4S)Off$ are the control samples used to measure the continuum background events estimated from $\Upsilon(4S)On$ data. The events in the 10th column represents the numbers survived in data sample. Event numbers shown on the On and Off peak resonance of control sample data are corrected for the different integrated luminosities as well as slightly different cross sections arising from the difference in CM energy.

Selection	**Efficiency** $\varepsilon_{e\mu}$	**Survived Events on MCs**				$\Upsilon(4S)$**Off**	$\Upsilon(4S)$**On**	$\Upsilon(3S)$**Off**	$\Upsilon(3S)$**On**
		$\mu\mu$	$\tau\tau$	Υ**(3S)**	**Bhabha**				
Pre-Selec. (blinded)	82612	22649650	13333831	7134301	599556063	152445188	148286975	257079590	254122200
PID-Selec.	0.2355 ± 0.0013	4.73 ± 1.37	0	0	0	3.62 ± 3.62	14.71 ± 2.30	0	18
Lep. Mom.	0.2684 ± 0.0012	54.00 ± 4.61	91.40 ± 6.29	82.67 ± 6.03	24.86 ± 14.35	210.22 ± 26.91	263.39 ± 9.72	288.43 ± 54.50	302
Back to back	0.2402 ± 0.0013	9.07 ± 1.89	43.32 ± 43.32	0.44 ± 0.44	0	68.84 ± 15.79	37.67 ± 3.67	51.50 ± 23.03	39
Accept. on EMC	0.2495 ± 0.0013	5.12 ± 1.42	0	0	0	7.24 ± 5.12	13.99 ± 2.24	0	17
Energy on EMC	0.2452 ± 0.0013	5.12 ± 1.42	0	0	0	3.62 ± 3.62	17.58 ± 2.51	0	19
All Cuts	0.2342 ± 0.0013	4.73 ± 1.37	0	0	0	3.62 ± 3.62	12.20 ± 2.09	0	15

As mentioned earlier, our multivariate technique allows us to measure 16 different selector combinations to choose the appropriate PID selectors to implement on the analysis. Usually, a looser selection means higher efficiency but also higher misidentification rate and a tighter selection means lower efficiency but also lower misidentification rate. In our analysis, we choose to go with tighter selection to reduce background as much as we can. Figures 4.11 - 4.22 show the distributions of $e^{\pm}\mu^{\mp}$ mass for 16 different PID combinations. Figures 4.27 - 4.38 show the distributions for the mass of $e^{\pm}\mu^{\mp}$ in 16 different PID combinations estimated from Υ(4S)On data. The colour scheme for the following figures are: the sea-green histogram represents μ-pairs, yellow histogram is for Bhabha and the tan histogram is for generic Υ(3S) while the red histogram is the signal MC and the black line with error bars represents 3 % unblinded data sample. Table 4.12 summarize variation in outcomes with different PID selectors after all selection requirements are applied. We checked the performance of each PID selector as $(\frac{N_{candidate}}{\sqrt{N_{Background}}})$ with keeping MC signal efficiency ε_{SIG} high and measured the BF for each set of PID combination to know the best performing PID selector. For example in 11th row the PID selector (e=11 and μ=19) provides ε_{SIG} = 0.1827 $\pm$ 0.0012 and 26 background events from $\Upsilon(4S)On$ Data. For this PID combination, background is suppressed impressively, however the efficiency became very low which provides a poorer BF sensitivity. Considering all of those outcomes we choose to use the optimized PID selectors (e=11 and $\mu = 18$) in our analysis.

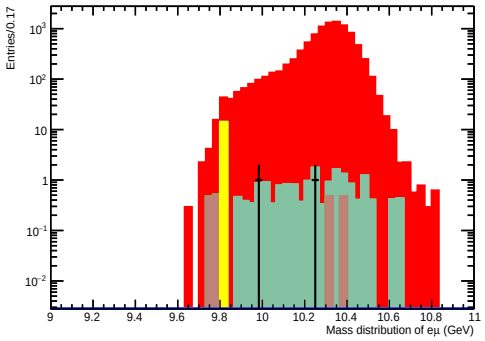

Figure 4.11: Mass distribution of $e^{\pm}\mu^{\mp}$ after all selection criteria are applied. PID selectors e=5 and μ=17 are used in this selection.

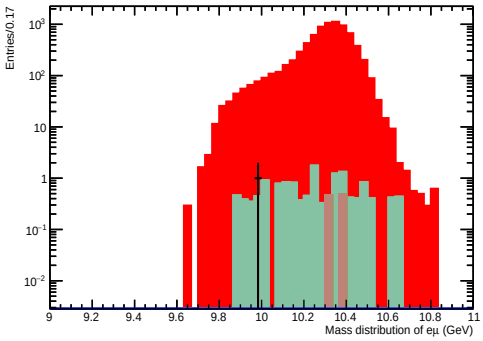

Figure 4.12: Mass distribution of $e^{\pm}\mu^{\mp}$ after all selection criteria are applied. PID selectors e=5 and μ=18 are used in this selection.

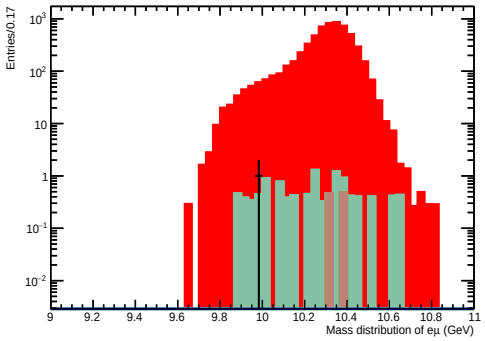

Figure 4.13: Mass distribution of $e^{\pm}\mu^{\mp}$ after all selection criteria are applied. PID selectors e=5 and μ=19 are used in this selection.

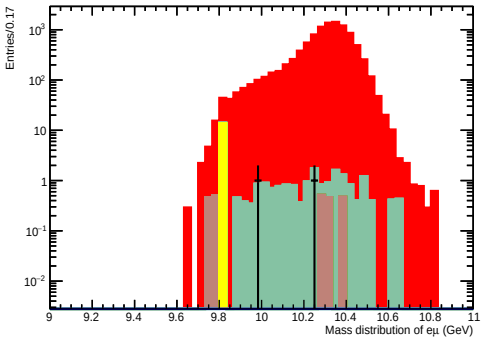

Figure 4.14: Mass distribution of $e^{\pm}\mu^{\mp}$ after all selection criteria are applied. PID selectors e=5 and μ=23 are used in this selection.

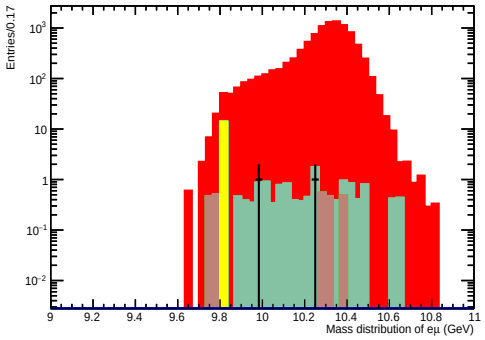

Figure 4.15: Mass distribution of $e^{\pm}\mu^{\mp}$ after all selection criteria are applied. PID selectors e=9 and μ=17 are used in this selection.

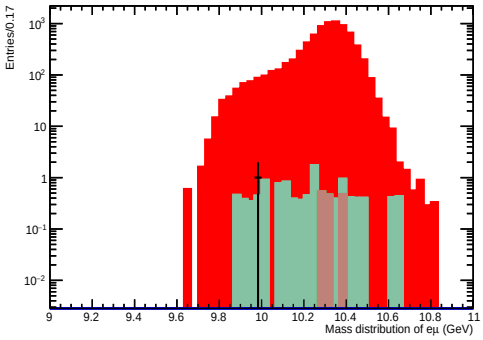

Figure 4.16: Mass distribution of $e^{\pm}\mu^{\mp}$ after all selection criteria are applied. PID selectors e=9 and μ=18 are used in this selection.

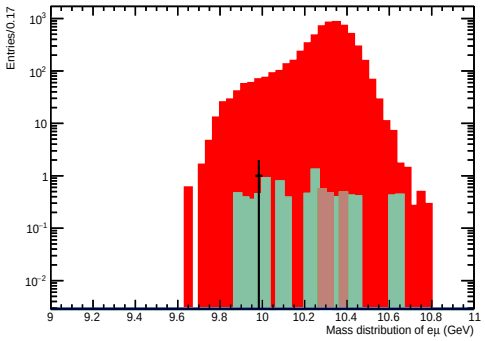

Figure 4.17: Mass distribution of $e^{\pm}\mu^{\mp}$ after all selection criteria are applied. PID selectors e=9 and μ=19 are used in this selection.

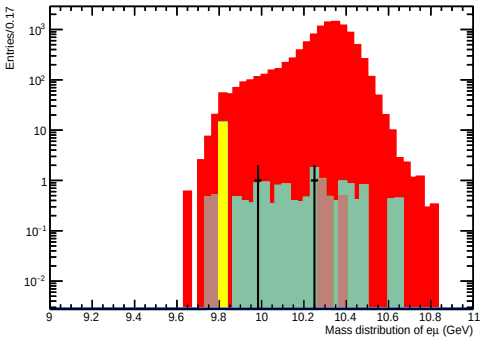

Figure 4.18: Mass distribution of $e^{\pm}\mu^{\mp}$ after all selection criteria are applied. PID selectors e=9 and μ=23 are used in this selection.

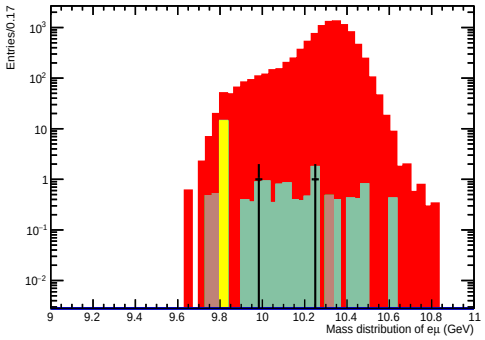

Figure 4.19: Mass distribution of $e^{\pm}\mu^{\mp}$ after all selection criteria are applied. PID selectors e=10 and μ=17 are used in this selection.

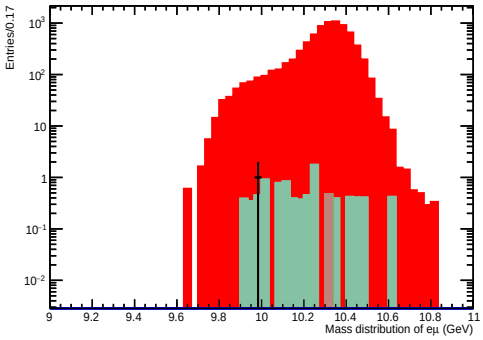

Figure 4.20: Mass distribution of $e^{\pm}\mu^{\mp}$ after all selection criteria are applied. PID selectors e=10 and μ=18 are used in this selection.

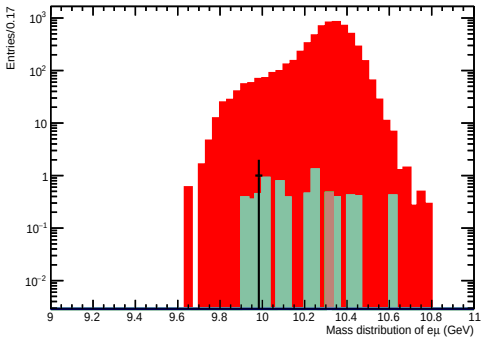

Figure 4.21: Mass distribution of $e^{\pm}\mu^{\mp}$ after all selection criteria are applied. PID selectors e=10 and μ=19 are used in this selection.

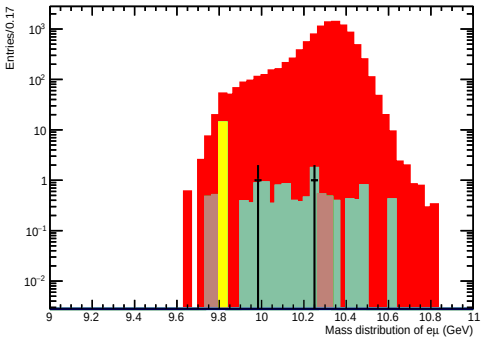

Figure 4.22: Mass distribution of $e^{\pm}\mu^{\mp}$ after all selection criteria are applied. PID selectors e=10 and μ=23 are used in this selection.

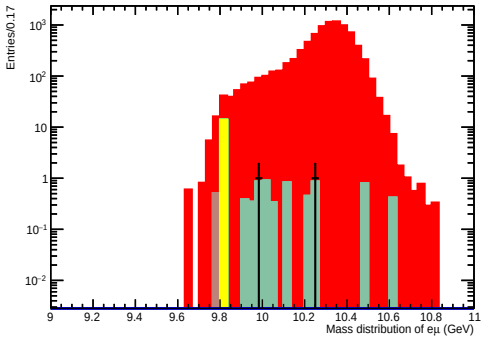

Figure 4.23: Mass distribution of $e^{\pm}\mu^{\mp}$ after all selection criteria are applied. PID selectors e=11 and μ=17 are used in this selection.

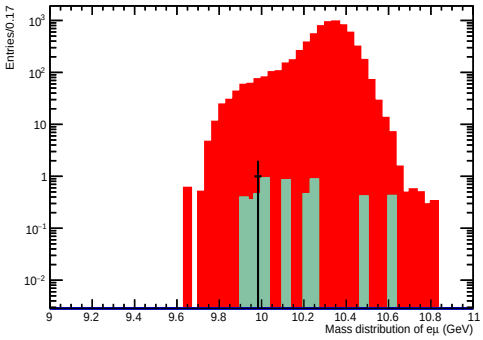

Figure 4.24: Mass distribution of $e^{\pm}\mu^{\mp}$ after all selection criteria are applied. PID selectors e=11 and μ=18 are used in this selection.

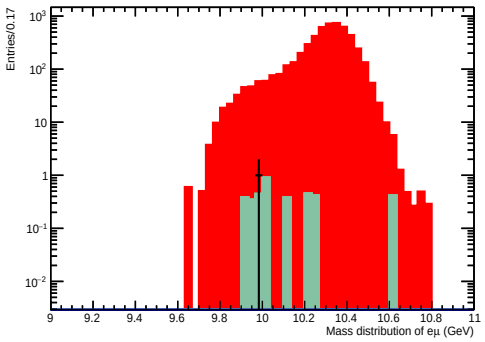

Figure 4.25: Mass distribution of $e^{\pm}\mu^{\mp}$ after all selection criteria are applied. PID selectors e=11 and μ=19 are used in this selection.

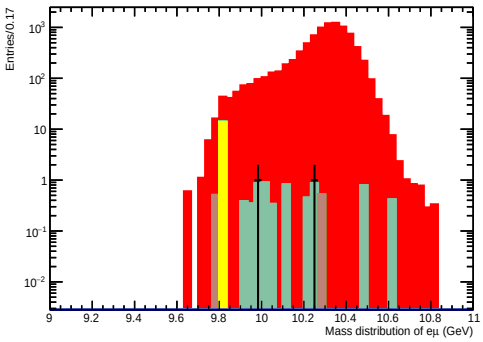

Figure 4.26: Mass distribution of $e^{\pm}\mu^{\mp}$ after all selection criteria are applied. PID selectors e=11 and μ=23 are used in this selection.

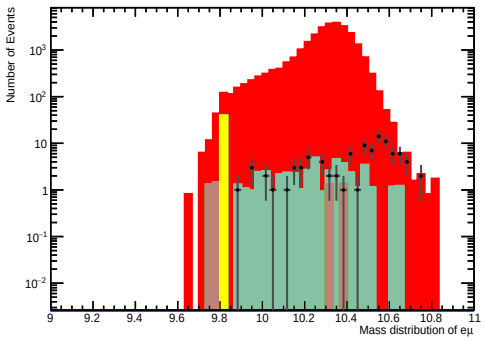

Figure 4.27: Mass distribution of $e^{\pm}\mu^{\mp}$ in Data $\Upsilon(4S)On$ after all selection criteria are applied. PID selectors e=5 and μ=17 are used in this selection.

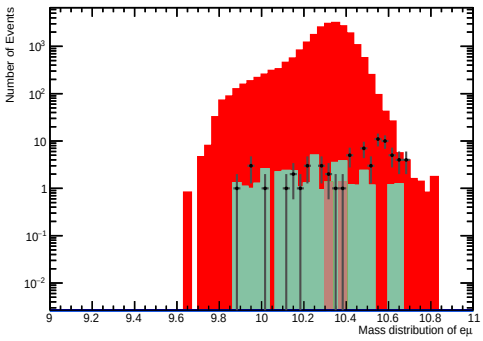

Figure 4.28: Mass distribution of $e^{\pm}\mu^{\mp}$ in Data $\Upsilon(4S)On$ after all selection criteria are applied. PID selectors e=5 and μ=18 are used in this selection.

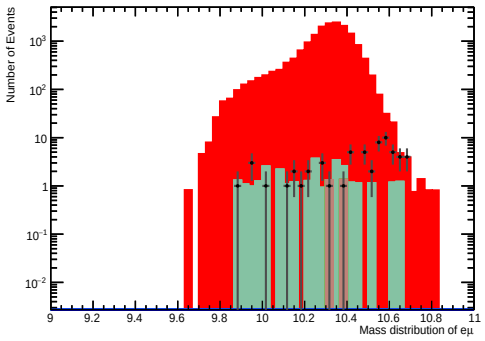

Figure 4.29: Mass distribution of $e^{\pm}\mu^{\mp}$ in Data $\Upsilon(4S)On$ after all selection criteria are applied. PID selectors e=5 and μ=19 are used in this selection.

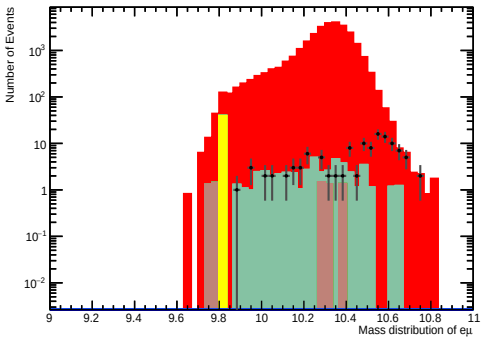

Figure 4.30: Mass distribution of $e^{\pm}\mu^{\mp}$ in Data $\Upsilon(4S)On$ after all selection criteria are applied. PID selectors e=5 and μ=23 are used in this selection.

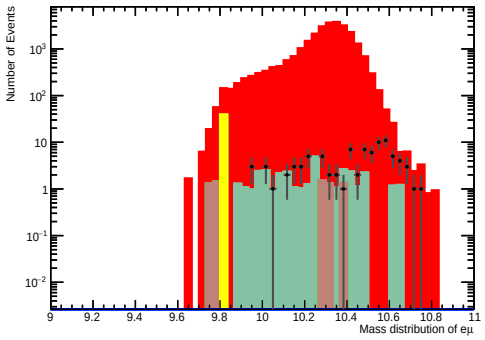

Figure 4.31: Mass distribution of $e^{\pm}\mu^{\mp}$ in Data $\Upsilon(4S)On$ after all selection criteria are applied. PID selectors e=9 and μ=17 are used in this selection.

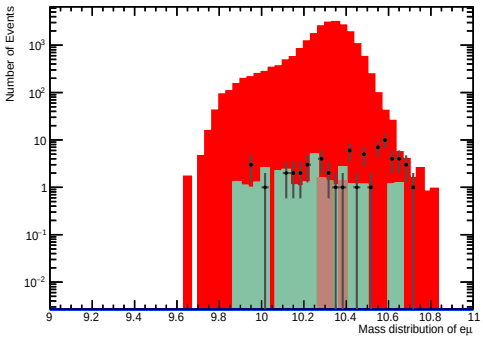

Figure 4.32: Mass distribution of $e^{\pm}\mu^{\mp}$ in Data $\Upsilon(4S)On$ after all selection criteria are applied. PID selectors e=9 and μ=18 are used in this selection.

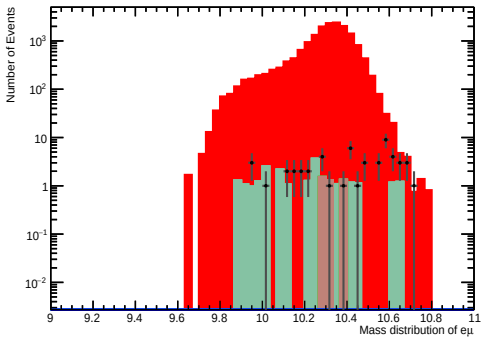

Figure 4.33: Mass distribution of $e^{\pm}\mu^{\mp}$ in Data $\Upsilon(4S)On$ after all selection criteria are applied. PID selectors e=9 and μ=19 are used in this selection.

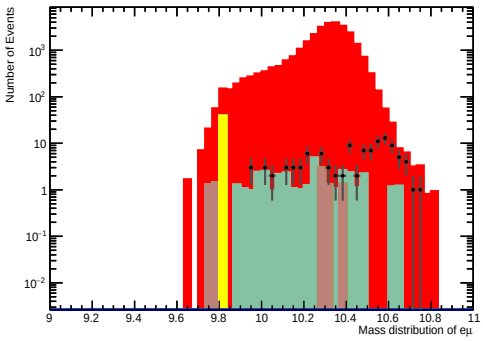

Figure 4.34: Mass distribution of $e^{\pm}\mu^{\mp}$ in Data $\Upsilon(4S)On$ after all selection criteria are applied. PID selectors e=9 and μ=23 are used in this selection.

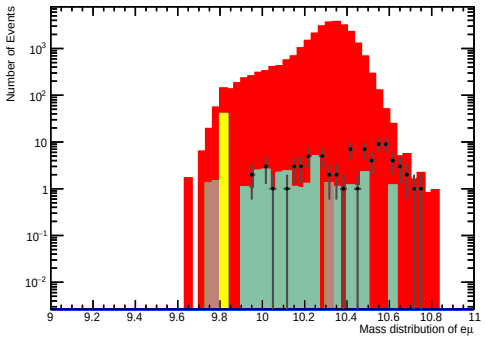

Figure 4.35: Mass distribution of $e^{\pm}\mu^{\mp}$ in Data $\Upsilon(4S)On$ after all selection criteria are applied. PID selectors e=10 and μ=17 are used in this selection.

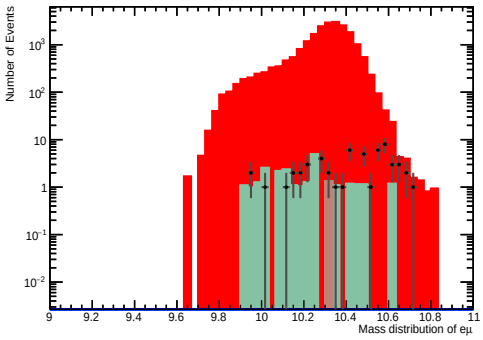

Figure 4.36: Mass distribution of $e^{\pm}\mu^{\mp}$ in Data $\Upsilon(4S)On$ after all selection criteria are applied. PID selectors e=10 and μ=18 are used in this selection.

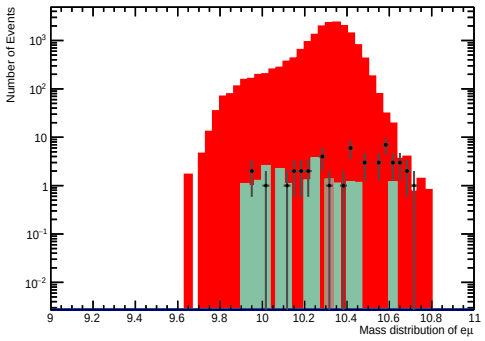

Figure 4.37: Mass distribution of $e^{\pm}\mu^{\mp}$ in Data $\Upsilon(4S)On$ after all selection criteria are applied. PID selectors e=10 and μ=19 are used in this selection.

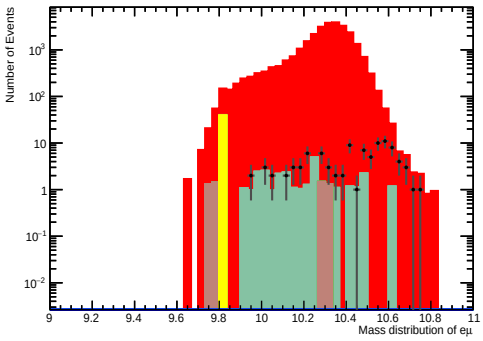

Figure 4.38: Mass distribution of $e^{\pm}\mu^{\mp}$ in Data $\Upsilon(4S)On$ after all selection criteria are applied. PID selectors e=10 and μ=23 are used in this selection.

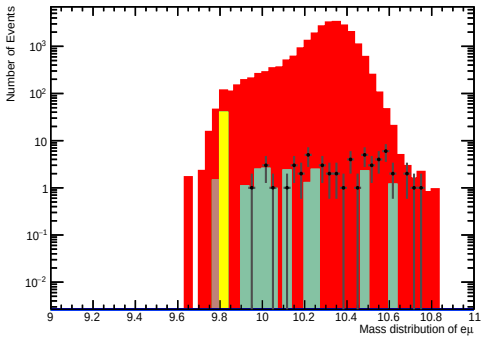

Figure 4.39: Mass distribution of $e^{\pm}\mu^{\mp}$ in Data $\Upsilon(4S)On$ after all selection criteria are applied. PID selectors e=11 and μ=17 are used in this selection.

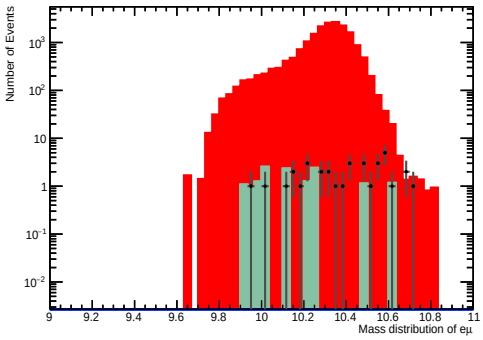

Figure 4.40: Mass distribution of $e^{\pm}\mu^{\mp}$ in Data $\Upsilon(4S)On$ after all selection criteria are applied. PID selectors e=11 and μ=18 are used in this selection.

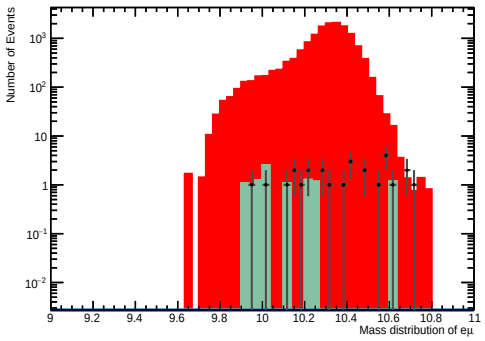

Figure 4.41: Mass distribution of $e^{\pm}\mu^{\mp}$ in Data $\Upsilon(4S)On$ after all selection criteria are applied. PID selectors e=11 and μ=19 are used in this selection.

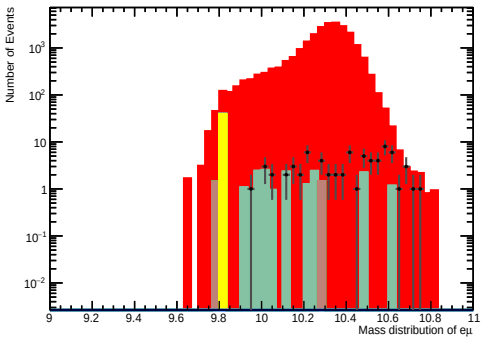

Figure 4.42: Mass distribution of $e^{\pm}\mu^{\mp}$ in Data $\Upsilon(4S)On$ after all selection criteria are applied. PID selectors e=11 and μ=23 are used in this selection.

Table 4.12: Different levels of efficiency and rejection can be achieved with different PID selectors after all selection requirements applied. The second coloumn shows the N_{DATA} survived in the 3 % unblinded sample luminosity. The third coloumn shows the original number of background events survived in Υ(4S) dataset of luminosity 78.31 fb^{-1}. The fourth coloumn shows the different surviving background processes for a particular selector combination. The actual number of survived events are given here for $\mu^+\mu^-$, Bhabha, and generic Υ(3S) MC of luminosity 68.55 fb^{-1}, 10.44 fb^{-1} and 61.44 fb^{-1} respectively.

PID Selectors	ϵ_{SIG}	$\mathbf{N}_{DATA}$ 3 % Unblinded Sample	$\mathbf{N}_{BG}$ Data $\Upsilon(4S)$ On	**Survived BG events** real numbers
e=5, μ= 17	0.3314 ± 0.0015	2	94	$\mu^+\mu^-$: (39 events), Bhabha:(1 event) Generic $\Upsilon(3S)$: (2 events)
e=5, μ= 18	0.2687 ± 0.0015	1	68	$\mu^+\mu^-$: (31 events), Generic : (2 events)
e=5, μ= 19	0.2093 ± 0.0015	1	59	$\mu^+\mu^-$: (24 events), Generic $\Upsilon(3S)$: (2 events)
e=5, μ= 23	0.3472 ± 0.0015	2	115	$\mu^+\mu^-$: (40 events), Generic $\Upsilon(3S)$: (5 events)
e=9, μ= 17	0.3336 ± 0.0015	2	94	$\mu^+\mu^-$: (29 events), Bhabha:(1 event) Generic $\Upsilon(3S)$: (5 events)
e=9, μ= 18	0.2706 ± 0.0014	1	68	$\mu^+\mu^-$: (24 events), Generic $\Upsilon(3S)$: (3 events)
e=9, μ= 19	0.2109 ± 0.0013	1	51	$\mu^+\mu^-$: (18 events), Generic $\Upsilon(3S)$: (2 events)
e=9, μ= 23	0.3496 ± 0.0015	2	105	$\mu^+\mu^-$: (29 events), Bhabha:(1 event) Generic $\Upsilon(3S)$: (6 events)
e=10, μ= 17	0.3269 ± 0.0015	2	76	$\mu^+\mu^-$: (25 events), Bhabha:(1 event) Generic $\Upsilon(3S)$: (3 events)
e=10, μ= 18	0.2651 ± 0.0014	1	54	$\mu^+\mu^-$: (21 events), Bhabha:(1 event)
e=10, μ= 19	0.2065 ± 0.0013	1	44	$\mu^+\mu^-$: (16 events), Generic $\Upsilon(3S)$: (1 event)
e=10, μ= 23	0.3426 ± 0.0015	2	94	$\mu^+\mu^-$: (25 events), Bhabha:(1 event) Generic $\Upsilon(3S)$: (4 events)
e=11, μ= 17	0.2889 ± 0.0014	2	53	$\mu^+\mu^-$: (16 events), Bhabha:(1 event) Generic $\Upsilon(3S)$: (1 event)
e=11, μ= 18	0.2342 ±0.0014	1	34	$\mu^+\mu^-$: (12 events) (Optimal PID)
e=11, μ= 19	0.1827 ± 0.0012	1	26	$\mu^+\mu^-$: (9 events), Generic $\Upsilon(3S)$: (1 event)
e=11, μ= 23	0.3026 ± 0.0014	2	69	$\mu^+\mu^-$: (16 events), Bhabha:(1 event) Generic $\Upsilon(3S)$: (4 event)

Chapter 5

Systematic Uncertainties

During the running of the BaBar experiment, the detector simulation has been continuously improved to obtain background and signal MC samples as similar as possible to data. However there are still some discrepancies and many studies have been performed to have a good estimation of these discrepancies to be accounted as systematic errors.

For this analysis, we consider systematic uncertainties by taking the ratio of data/MC yields for the τ-pair in three different e-μ mass sidebands. In our systematic analysis, we reversed two major cuts (lepton momentum cut and angle between 2 tracks) to get abundant events of τ-pairs. We studied the systematics error in these two cuts by shifting the cut value from its default value, to account for potential systematic differences between the MC and data. For the background samples, the number of selected events is not too large and statistics uncertainties dominate over the systematic ones. We used $\Upsilon(4S)$ data to estimate the continuum background. Both $\Upsilon(4S)$ and $\Upsilon(3S)$ data were taken with same detector configuration and after updrate in IFR. Morover $\Upsilon(4S)$ has an abundant luminosity to keep the statistical uncertainty lower. Determing background from data is known as data driven background. After applying all selection criteria, no background events were survived from generic Υ(3S) MC in our analysis as we explained earlier in analysis, chapter 4. However, to estimate a contribution from the same, we use loosen PID selectors (so that some generic Υ(3S) MC events could survive). The uncertainty in those loosen PID survived events are considered as the systematic uncertainty for background events.

The uncertainties in these quantities are summarized in Table 5.4 for Y(3S) data..

5.1 Signal Selection Efficiency

The branching fraction $\mathcal{BF}$ is determined from the signal yield N_{SIG} according to $\mathcal{BF} = \frac{N_{Data} - N_{BG_{\Upsilon(4S)}}}{\varepsilon_{SIG} \times N_{\Upsilon}}$ where ε_{SIG} is the signal selection efficiency and N_{Υ} is the number of collected Υ(3S) decays. The uncertainties in these quantities are summarized in Table 5.1.

5.1.1 Systematic Uncertainty in the Sidebands

To determine the uncertainty, we are using controlled sample of tau's in the "Side Bands" where two major selection criteria are reversed. Reversed selection is applied in the cuts "angle between two tracks" and "lepton momentum plane". Full set of Υ(3S) data of luminosity 27.96 fb^{-1} constitutes a control samples which do not contain signal events. Figure 5.1 shows the data/MC difference in the side bands in the control sample. There is a very small disgreement between the data/MC, which originates due to the systematic uncertainty in particle identification, tracking, kinematics, trigger selection criteria etc. In the control samples, we have taken the ratio of $\frac{N_{Data} - N_{BG}}{N_{\tau-pairs}}$ yields for the 3 different side bands by varying the range of mass distribution. The nominal correction factor of 1.007 $\pm$ 0.007 is determined by taking the yield ratio over the range (6-8) GeV, which is closest to the signal region, where the agreement with MC and data is excellent. Taking the quadrature sum of error in ratio (0.010) and the difference between data and MC (0.0072), giving an uncertainty of 0.012 which is 1.2%. This procedure determines that the selection efficiency of Signal MC is having a good agreement to the corresponding efficiency for data, and a very nominal correction factor of 1.007 need to be applied to the signal MC. Table 5.1 provides the number of events in three side bands of data, simulated MCs and τ-pairs in control sample.

5.1.2 Systematic Uncertainties in the Reversed Cuts

We also measure the shift in efficiency of two specific cuts that used to be reversed in the control sample. The shift is calculated from event counting. The default cut is applied at 0.010 on the radius of a circle formed in the lepton momentum planes. Applying shifts on default cut as 0.010 $\pm$ 0.0015 provides a new upper and lower bound at 0.0115 and 0.0085 in the cut. Table 5.2 provides the number of events and efficiencies for the default cut and shifts in the lepton momentum cut for signal MC

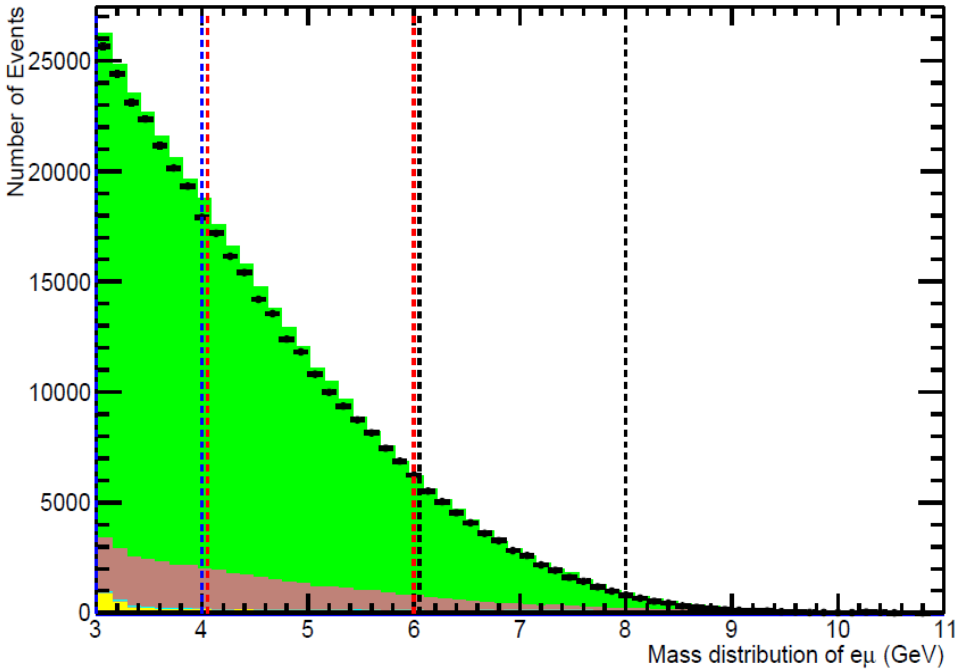

Figure 5.1: The signal efficiency is determined by comparing data and MC yields for a portion of the sideband of the for τ-pair in mass distribution of eμ.

and data selected as $\mu-$pairs. To see the level of agreement between data selected as $\mu-$ pairs, we also count events in simulated background MC in $\mu-$pairs.

Table 5.1: The number of events and efficiencies by varying the range over 3 side bands for data(3S), Background MCs and $\tau-$pairs in the control samples. Order of other non tau BGs Generic $\Upsilon(3S)$, $\mu^+\mu^-$, Bhabha, uds, $c\bar{c}$.

	Blue Side Band 3-4 GeV	**Red Side Band** 4-6 GeV	**Black Side Band** 6-8 GeV
$\frac{N_{DATA-N_{BG}}}{N_{\tau-pairs}}$	$\frac{174050-(17143+262+1472+7+262)}{157931}$ $=\frac{155166}{157931}$	$\frac{186227-(19074+354+93+5+95)}{170089}$ $=\frac{166606}{170089}$	$\frac{47774-(4798+340+0+2+2)}{42325}$ $=\frac{42632}{42325}$
R $\pm$ σ_R	0.9825 $\pm$ 0.0029	0.9795 $\pm$ 0.0032	1.0072 $\pm$ 0.010

Table 5.2: The number of events and efficiencies for the default cut of equation 4.3 and shifts in the lepton momentum cut for signal MC, Background MC and data selected as $\mu-$pairs. The shift was applied on the default value as 0.010 ± 0.0015 on equation 4.3.

Cut Values	**Signal** MC ($e\mu$)	**Efficiency** $\varepsilon_{e\mu}$	**Background** MC ($\mu\mu$)	**Efficiency** $\varepsilon_{\mu\mu}$	**Data3Son** as ($\mu\mu$)	**Efficiency** ε_{DATA}
Default Value 0.010	24127	0.234243	37965	0.00046	27540	0.000028
(0.010 + 0.0015) shift: 0.0115	24232	0.235262	38295	0.00047	27697	0.000028
(0.010 - 0.0015) Shift: 0.0085	23938	0.232408	37424	0.00046	27294	0.000027

We measure $\varepsilon^{0.0115-0.010}_{0.010-0.0085}$ by varying over the values as mentioned in Table 5.2; provides the relative change (0.001526/0.234243)= 0.0065 which is 0.65 % in MC signal. We also measure $\varepsilon^{0.0115-0.010}_{0.010-0.0085}$ for data selected as μ-pairs provides a relative change (0.0000010/0.000028) = 0.036 which is 3.6 %. Finally, we can measure the uncertainty between data and MC which is 0.036-0.0065 = 0.029 which is 2.9 %. Figure 5.2 shows the shift in cut applied on the radius of a circle formed on the lepton momentum planes for data and MC signal.

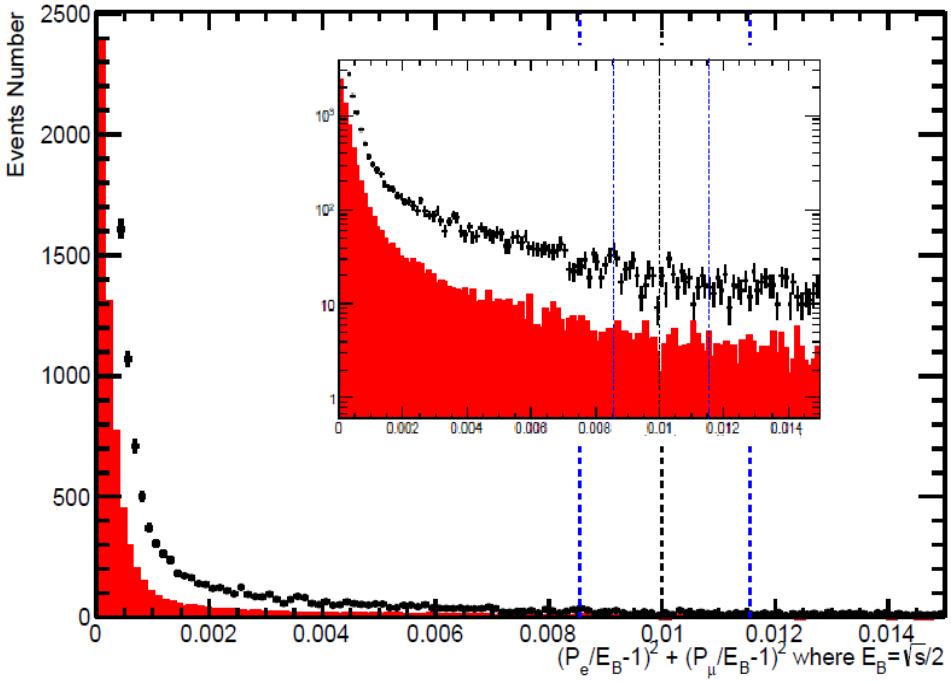

Figure 5.2: Relative uncertainty in efficiency is taken as the difference due to shift in lepton momentum cut which is 0.0065 in between signal MC and data. The red histogram is the Signal MC while the histogram in black line with error bars represents Υ(3S) DATA selected as μ-pairs. This data were preselected with BGFEMu (Filter criterion were explained ealier in chapter 4.

The other shift is applied on the cut "angle between two lepton tracks". The shift is calculated from event counting. The default value in the cut at 179° ± 0.1 provides a new upper and lower bound at 179.1° and 178.9°. Table 5.3 provides the number of events and efficiencies for the default cut and shifts in the cut "angle between two lepton tracks" for signal MC and data selected as $\mu-$pairs where the data was preselected with BGFEMu filter. To see the level of agreement between data selected

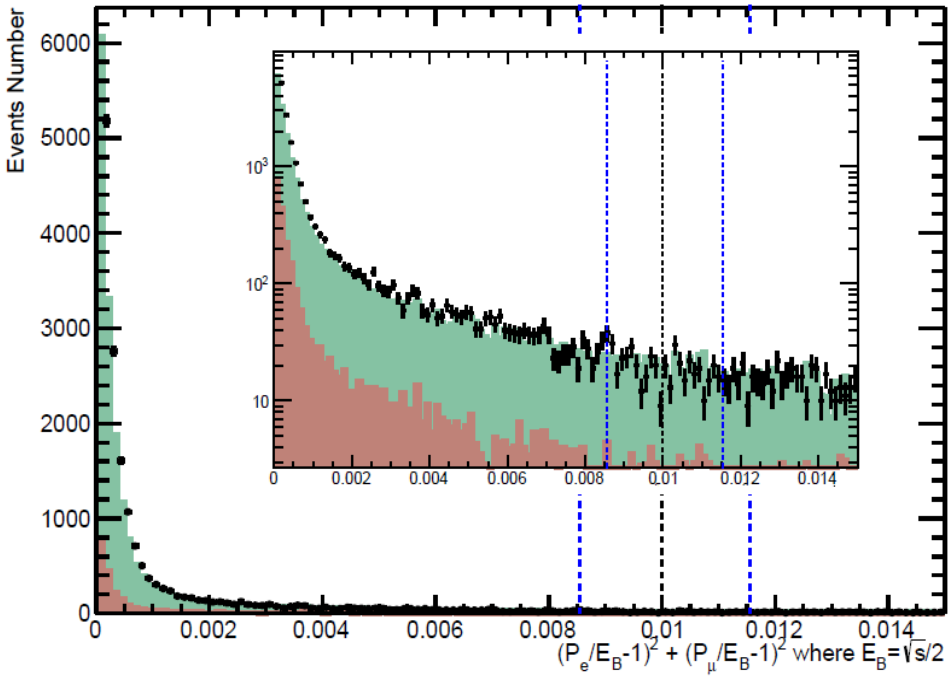

Figure 5.3: The agreement in data with other background MCs due to shift in lepton momentum cut. Uncertainty between data and background MC ($\mu\mu$) is 0.036-0.022 = 0.014 which is 1.4 %. The sea-green and tan coloured histogram represent the background MC $\mu\mu$ and generic Υ(3S) MC selected as μ-pairs respectively while the histogram in black line with error bars represents Υ(3S) data selected as μ-pairs.

as $\mu-$pairs we also count events in simulated background MC in $\mu-$pairs.

Table 5.3: Number of events and efficiencies for the default cut and shifts in the cut "angle between two lepton tracks" for signal MC, Backgound MC and data selected as $\mu-$pairs.

Cut Values	**Signal** MC ($e\mu$)	**Efficiency** $\varepsilon_{e\mu}$	**Background** MC ($\mu\mu$)	**Efficiency** $\varepsilon_{\mu\mu}$	**Data3Son** as ($\mu\mu$)	**Efficiency** ε_{DATA}
Default Value (179)	24127	0.234243	37965	0.00046	27540	0.0000281
(179 + 0.01) Shift: 179.1	24051	0.233505	37481	0.00046	27195	0.0000277
(179 − 0.01) (Shift: 178.9)	24179	0.234748	38454	0.00047	27824	0.0000283

We measure $\varepsilon^{179.1-179}_{179-178.9}$ by varying over the values as mentioned in Table 5.3; provides the relative change (0.000538/0.234243)= 0.002297 which is 0.23 % in MC signal. We also measure $\varepsilon^{179.1-179}_{179-178.9}$ for data selected as μ-pairs provides a relative change 0.00000035/0.000028)= 0.013 which is 1.3 %. Finally we can measure the uncertainty between the data and signal MC which is 0.013-0.002 = 0.011. Figure 5.4 shows the shift in cut applied on the angle between two lepton tracks between Υ(3S) data and signal MC when data is selected as $\mu\mu$ rather than eμ. We also check the distribution of the angle between two lepton tracks on Υ(4S) On resonance data preselected as BGFMuMu events and scaled to the Υ(3S) luminosity and compared with Υ(3S) continuum and resonance MC shown in Figure 5.5. Note that there is a small shift (0.05°) in the peaks most likely related to the boost in the MC not being exactly the same as in the data. These small shifts in the peak are within the systematic errors assigned to the systematic shifts that we use for the angle cut systematic uncertainty estimate.

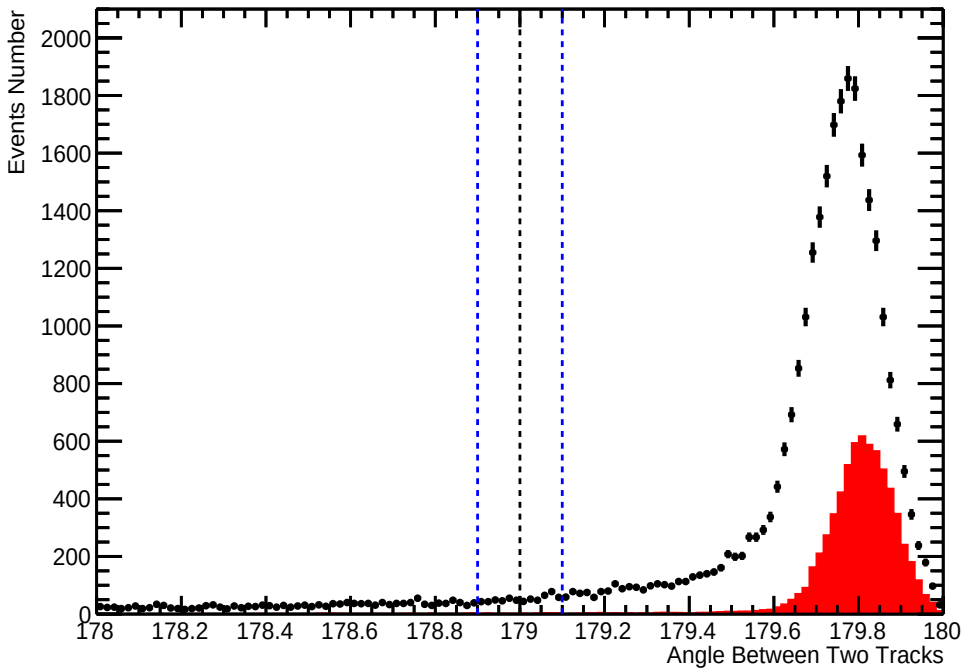

Figure 5.4: Relative uncertainty in efficiency is taken as the difference due to shift in "angle between two lepton tracks" cut which is 0.010 in between signal MC and data. The red histogram is the Signal MC while the histogram in black line with error bars represents Υ(3S) data selected as μ-pairs.

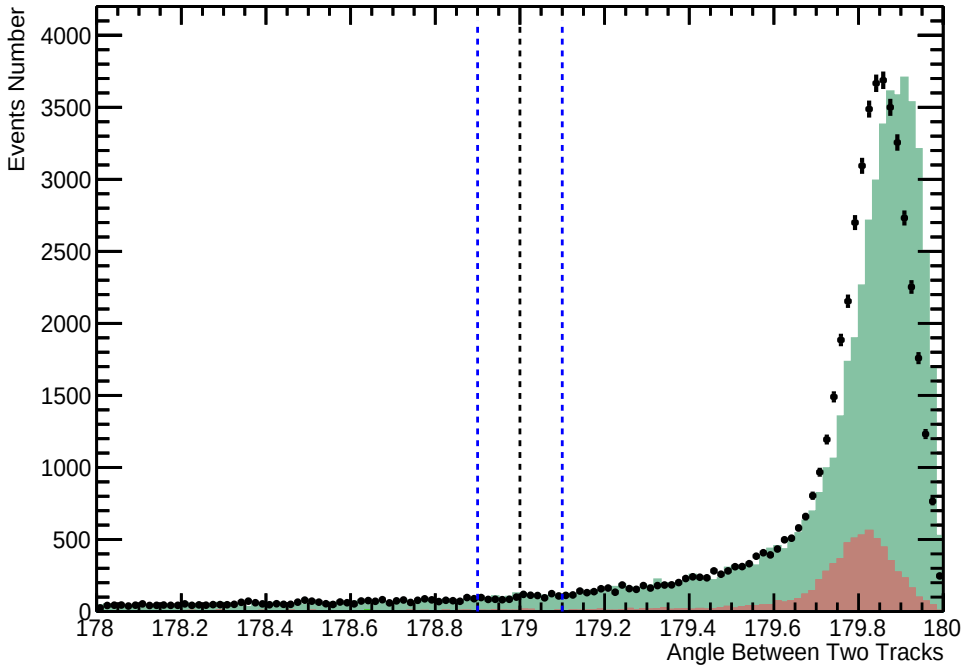

Figure 5.5: Shown is the angle between two lepton tracks on Υ(4S)On resonance data preselected as BGFMuMu events and scaled to the Υ(3S) luminosity and compared with Υ(3S) continuum and resonance MC. The sea-green and tan coloured histogram represent the background MC $\mu\mu$ and generic Υ(3S) MC selected as μ-pairs respectively while the histogram in black line with error bars represents Υ(4S) data.

5.1.3 Statistical Uncertainty in Signal Efficiency

Due to the finite statistics, there is a statistical uncertainty in the signal efficiency too. The uncertainty in ε_{SIG} is given by $\sqrt{\frac{\varepsilon(1-\varepsilon)}{n}}$. This procedure gives a statistical uncertainty of 0.0013.

5.1.4 Number of Collected Υ(3S) Decays

The number of collected Υ(3S) DATA decays for 3 % unblinded sample is $(4.06\pm0.04)\times10^6$ and for blinded luminosity is $(117.70 \pm 1.18) \times 10^6$, giving a 1.0 % uncertainty. These values [81] have been determined by Chris Hearty, David Hutchcroft and Grant McGregor.

5.2 Uncertainty in Background Estimate

By using the optimized PID selector, for electron and muon, no background event survived from generic Υ(3S) SP collection. Thus, we estimate the equivalent continuum background and its uncertainty using Υ(4S) dataset which is 0.42 ± 0.07. The actual number of events survived in Υ(4S) dataset of luminosity of 78.31 fb^{-1} is 34. However to estimate a contribution from the generic Υ(3S), we use loosen PID selectors (LHtight = 5 for electron and bdtLoose=17 for muon). The actual number of survived background events in generic Υ(3S) MC (within 61.44fb^{-1}) is 4, which provides an equivalent background of 0.060 ± 0.030 in the luminosity of the unblinded sample and 1.80 ± 0.88 in the luminosity of the to be unblinded sample. Uncertainty in the total estimated background for the unbinded sample luminosity is thus calculated by taking the quadrature sum of events seen in loosen PID selection and error measured in Run6 which is 0.42 ± 0.07. In the same way, we calculate the total uncertainty in the projected luminosity which is 12.2 ± 2.3, taken as the quadrature sum of error in Υ(4S) data and error seen in Υ(3S) MC using loosen PID selection. Figure 5.6 shows the number of events survived in Υ(4S) Data after applying all selection criteria.

5.3 Summary

Table 5.4 shows a summary of various systematic uncertainties that will be included into the final results for upper limit estimation. The total uncertainty in signal MC is determined summing in quadrature from all the contributions.

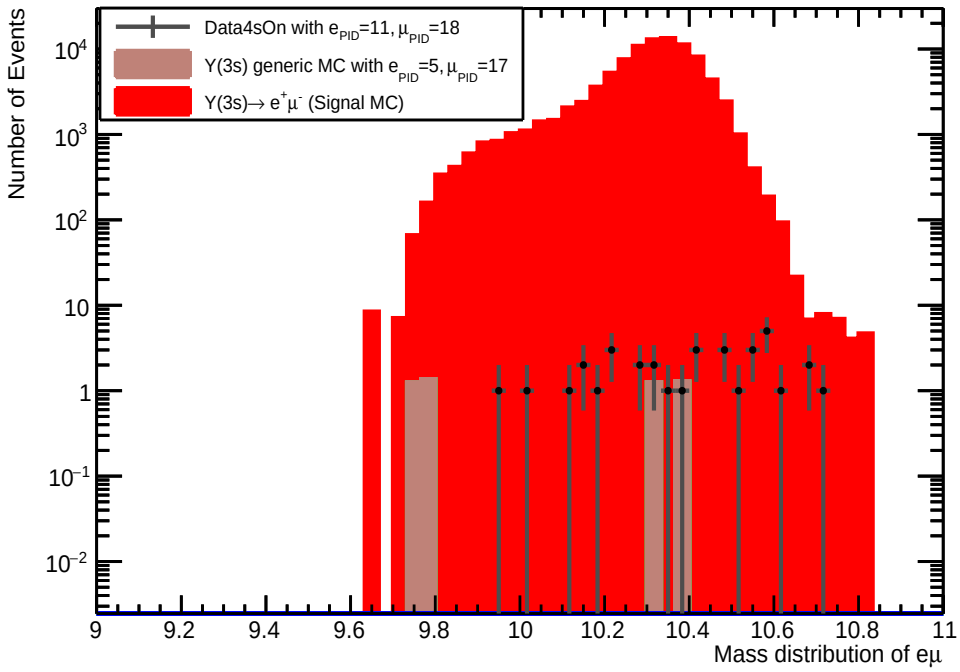

Figure 5.6: Mass distribution of eμ at Υ(4S) dataset (histogram in black lines with error bars). Actual number of survived events in 78.31 fb^{-1}, using PID selector, SuperTight=11 for electron and BDTTight=18 for muon is 34, While the histogram in tan colour represents Υ(3S) generic MC for loosen PID selectors (LHtight=5 for electron and bdtLoose=17 for muon). The actual number of events survived for the later is 4 within 61.44 fb^{-1} luminosity.

Table 5.4: Different parameter, value and uncertainty by source in signal efficiency, number of $\Upsilon(3S)$ decays and background estimation.

Parameter	**Value**	**Uncertainty by source (Relative value)**
ε_{SIG}		Lepton Momentum cut: 0.0068 (2.9 %) Back to back cut: 0.0026 (1.1 %) All other cuts (from sidebands) 0.0028 (1.2%) MC statistics: 0.0003 (0.13 %)
	0.2342	$\pm$ 0.0078 (3.3 %)
N_Υ		
Pre-blinded sample	4.06×10^6	$\pm$ 0.04 $\times$ 10^6 (0.98 %)
Data sample	117.7×10^6	$\pm$ 1.2 $\times$ 10^6 (1.02 %)
BG estimated from $\Upsilon(4S)$On		
Pre-unblinded sample	0.42	$\pm$ 0.07 (16.6 %)
Data sample	12.2	$\pm$ 2.3 (18.9 %)

Chapter 6

Result and Discussion

In this chapter, the results of the search for lepton flavor violation in $\Upsilon(3S) \rightarrow e^{\pm}\mu^{\mp}$ decays are presented. After including all the systematic uncertainties, the extracted signal yields for the eμ decay channel in the 3 % unblinded sample is consistent with expected backgrounds estimated from Run6 Υ(4S) data. A summary Table 5.1 is provided on the previous chapter 5 (Systematic Uncertainties) for the calculated values of signal efficiency, background estimation and number of $\Upsilon(3S)$ decays after all selection criteria applied were to the analysis. The branching fraction $\mathcal{BF}$ is calculated using the following equation:

$$\mathcal{BF} = (N_{Candidate} - N_{BG})/\varepsilon_{SIG} \times N_{\Upsilon(3S)}. \tag{6.1}$$

The signal yield in $\Upsilon(3S)$ data and background in the numerator of equation 6.1 are asymmetric and Poisson distributed events in nature. We use a Poisson calculator [82] to determine the Poisson confidence intervals [0.17, 3.29] at 68% confidence level which provides an uncertainty of $1^{+2.29}_{-0.73}$ in the upper and lower bound for the observed event. Using the upperbound value of the observed data, we calculate the central value of the $\mathcal{BF}$ which is 6.0×10^{-7}.

The uncertainty in $\mathcal{BF}$ for its central value can be calculated using the error propagation method as described in Equations 6.2 and 6.3. Equation 6.2 provides the statistical uncertainty of the upper and lower bounds of $\mathcal{BF}$, while equation 6.3 provides the systematic uncertainty on it. The calculated uncertainty in $\mathcal{BF}$ is $6.0 \pm \begin{pmatrix} 24 \\ 8.7 \end{pmatrix}_{STAT} \pm \begin{pmatrix} 0.8 \\ 0.8 \end{pmatrix}_{SYST} \times 10^{-7}$.

$$(\sigma_{BF})^2_{STAT} = (\frac{\delta_{BF}}{\delta_{N_{Candidate}}})^2(\sigma_{N_{Candidate}})^2 \tag{6.2}$$

$$(\sigma_{BF})^2_{SYST} = (\frac{\delta_{BF}}{\delta_{N_{BG}}})^2(\sigma_{N_{BG}})^2 + (\frac{\delta_{BF}}{\delta_{\varepsilon}})^2(\sigma_{\varepsilon})^2 + (\frac{\delta_{BF}}{\delta_{N_{\Upsilon}}})^2(\sigma_{N_{\Upsilon}})^2 \tag{6.3}$$

Clearly, this is consistent with BF = 0, so we set an upper limit (UL) at 90 % confidence level (CL) on $\mathcal{BF}$ by using a calculator program developed by Roger Barlow [83]. Table 6.1 shows the calculated UL for the 3 % unblinded sample and projected luminosity of $\Upsilon(3S)$ Data.

Table 6.1: Summary results of $\mathcal{BF}$ of ($\Upsilon(3S) \to e^{\pm}\mu^{\mp}$) mode. Displayed are the 90% confidence level upper limit in 3 % blinded sample and projected luminosity of Υ(3S) Data.

Measurements	**Upper Limit**	**Confidence Level (%)**
($\Upsilon(3S) \to e^{\pm}\mu^{\mp}$) (3 % unblinded sample)	$< 3.65 \times 10^{-6}$	90
($\Upsilon(3S) \to e^{\pm}\mu^{\mp}$) (projected)	$< 2.27 \times 10^{-7}$	90

6.1 Conclusions and Summary

In this thesis we present the search for the lepton flavour violating decay in $\Upsilon(3S) \to e^{\pm}\mu^{\pm}$ with the data taken by BaBar detector at the SLAC PEP-II e^+e^- asymmetric collider at a centre-of-mass energy of 10.36 GeV. According the Standard Model and the neutrino mixing parameters, branching fractions are estimated well below 10^{-14}, but many models of new physics allow for branching fractions values close to the present experimental sensitivity. There has been considerable interest in Charge Lepton Flavour Violation (CLFV) decays of the μ and τ leptons and B and K mesons, both in experimental searches and theoretical predictions for the branching ratios in various beyond standard model (BSM) scenarios. However, CLFV in the Υ sector remains relatively unexplored. Thus $\Upsilon(3S) \to e^{\pm}\mu^{\pm}$ is a promising channel to search for evidence of new physics as it has yet to be probed directly in experiments and the indirect limits are relatively weak. The analysis was performed in a blind way to avoid any experimenter bias.A data control sample collected at the Υ(3S) resonance (0.93

fb^{-1}), corresponding to roughly 3% of the full Υ(3S) sample, is used in a preliminary unblinded analysis to validate the analysis procedure and evaluating the systematic errors before looking at the signal data. Once the analysis was completed, with selection cuts and systematic errors finalized, the blind analysis took place as part of an internal review by the BaBar collaboration. It is only after an internal committee has reviewed and approved of the analysis then the results became unblinded. Following submission of this dissertation for examination, the BaBar Collaboration approved the unblinding of this analysis and the results of that unblinding are included in the Appendix. We present the branching fraction both in pre-blinding sample and data sample after the unblinding was approved.

The final search was conducted using a data sample in which 118 million $\Upsilon(3S)$ mesons were produced, corresponding to an integrated luminosity of 27 fb^{-1}. The tracking system, the calorimeter and the particle identification (PID) of BABAR, allow an extremely powerful rejection of background events for this analysis. For this analysis MC simulated events play a decisive role for estimating the signal efficiency and study the possible sources of background. However in our analysis, we use the data driven background as no signal is expected in data collected at the Υ(4S) since the LFV branching fractions are strongly suppressed, or in data collected away from the Υ resonances. For the ($\Upsilon(3S) \rightarrow e^{\pm}\mu^{\mp}$) channel, the signature consists of an electron and a muon each with CM momentum close to the CM beam energy. The electron and muon are emitted back-to-back in the CM frame. Thus with appropriate kinematic selection criteria we were able to eliminate most of the backgrounds. Another big fraction of the background is removed using the particle identification.

Two individual calculators (Barlow calculator and CLs method) were used to estimate the final upper limit. Both of the calculators were based on a modified frequentist analysis method. In the Barlow method confidence levels are estimated with a series of MC experiments where the efficiency and background are smeared by Gaussian distributions, thereby taking into account any experimental systematic uncertainties. The CLs method uses the likelihood ratio of a discriminant variable as test-statistics to compute the confidence level of two different hypotheses: the signal + background hypothesis and the background only one. For estimating the limit, the method uses the ratio of these two confidence levels and avoids statements concerning regions where the signal + background hypothesis cannot be discriminated against the background only one. In the BaBar review process, prior to unblinding, it was decided to use the CLs method would be used to determine a limit if no signal was

seen.

Finally this dissertation presents the results of the search for the LFV decays in $\Upsilon(3S) \rightarrow e^{\pm}\mu^{\mp}$. Several kinematic selection criteria and optimized PID selection are used to extract the signal yield. We find that 1 event survives in the 3 % unblinded sample with an expected background of 0.42 $\pm$ 0.07 events predicted. We measure the branching fraction $\mathcal{BF}$ of $(\Upsilon(3S) \rightarrow e^{\pm}\mu^{\mp}) < 3.66 \times 10^{-6}$ for the 3% unblinded luminosity. With the unblinded sample we also project a limit of $\mathcal{BF}$ in the luminosity of 27.02 fb^{-1} which is $< 2.27 \times 10^{-7}$ at 90 % CL in the absence of signal. After unblinding, 15 signal events survive in the data sample with 12.2 +/- 2.3 background events expected and we set a 90 % CL upper limit of $\mathcal{BF}(\Upsilon(3S) \rightarrow e^{\pm}\mu^{\mp}) < 3.6 \times 10^{-7}$.

From the discussion in Chapter 2, the theoretical constraint on this process from the upper limit on the branching fraction of $\mu \rightarrow 3e$ is 5 $\times 10^{-4}$. Our result is several orders of magnitude stronger that this limit. This result can be used to place constraints on $\frac{g_{NP}^2}{\Lambda_{NP}^2}$ of new physics processes that include lepton flavour violation such as those shown in Figures 2.4 and 2.5 in chapter 2.

These results represented here are the first reported experimental upper limit on $\Upsilon(3S) \rightarrow e^{\pm}\mu^{\mp}$.

6.2 Potential Future Studies

We will soon submit this result for publication in Physical Review and this measurement will be then a good reference for the future measurement and comparison. The branching fractions of $(\Upsilon(nS) \rightarrow e^{\pm}\mu^{\mp})$ (n= 1, 2) still remain unmeasured and could be a potential future project. In addition to this, the Belle II experiment at the SuperKEKB electron-positron collider in Japan, which is currently being commissioned, will commence data-taking in 2018. It is an experiment that is similar to BaBar but will ultimately collect roughly 100 times the integrated luminosity compared to BaBar. It will primarily study rare decays of B mesons and other processes with precision, in order to search for physics beyond the Standard Model of Particle Physics. If it collects significantly more luminosity at the $\Upsilon(3S)$ than BaBar collected, it can potentially improve the measurement of the $(\Upsilon(nS) \rightarrow e^{\pm}\mu^{\mp})$ branching fraction sensitivity by an order of magnitude.

Appendix A

Appendix

A.1 Unblinded Data Sample

As we mentioned in chapter 4, we employed blind analysis technique to make sure that the measurement is performed without looking at the answer to eliminate experimenters bias, At the BaBar collaboration, the blind analysis is undergo an internal review, With the approval of the analysis by review committee the results are unblinded. The internal review has done after submitting this dissertation for supervisory committee review. We got the unblinded result later on. All necessary plots and results are added in this appendix for further insight. We describe the direct search for LFV Υ(3S) decays in a sample of $(117.7 \pm 1.2) \times 10^6$ Υ(3S) decays corresponding to an integrated luminosity of 27.02 fb^{-1} collected at $\sqrt{s} = 10.36\ GeV$ henceforth denoted as data sample. This result is intended to publish in Physical Review Letter.

A.2 (N-1) Selection Plots for Data Sample

The pre-selection and user defined selection procedure remains exactly the same as we described in chapter 4. (N-1) plot means all cuts applied except that on the variable plotted are given below:

Figure A.1 depicts the (N-1) cut on the radius of circle in the lepton momentum planes for data sample overlay with MC backgrounds, while figure A.2 shows same data sample overlay with backgrounds estimated from R6 data.

Figure A.3 shows the distribution of angle between 2 tracks in (N-1) cut presentation for the data sample overlay with MC backgrounds, while Figure A.4 shows same

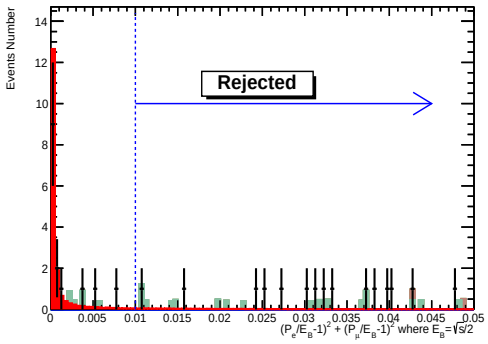

Figure A.1: Radius squared of the circle in the lepton momentum planes in (N-1) cuts in the data sample. The dashed blue line indicates that selection criteria is applied on 0.01 at x-axis to eliminate the background events. The sea green histogram shows μ-pair production and the brown and red histogram represents the generic Υ(3S) MC and signal MC respectively.

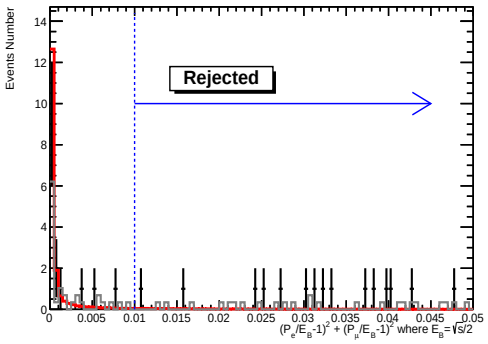

Figure A.2: Radius of the circle in the lepton momentum planes in (N-1) cuts in data sample. The dashed blue line indicates that selection criteria is applied on 0.01 at x-axis to eliminate the background events. The grey histogram is the Υ(4S)On resonance data scaled to the data sample (histogram in black line with error bars), and the red histogram represents the signal MC.

data sample overlay with backgrounds estimated from R6 data.

Figure A.5 shows the distribution of energy deposited at EMC by the muon track in (N-1) cut presentation for the data sample overlay with MC backgrounds, while Figure A.6 shows same data sample overlay with backgrounds estimated from R6 data.

After including all selection requirements, signal efficiencies determined from signal MC is $0.2342 \pm 0.0013_{stat}$ as mentioned earlier. After unblinding the data sample, we select 15 candidates for an estimated background of 12.2±2.3. This background event number is the equivalent number scaled to the luminosities of data sample. We use the Run 6 $\Upsilon(4S)$ dataset to estimate the continuum backgrounds as no $\Upsilon(4S) \rightarrow B\bar{B}$ decays pass the selection criteria and any potential signal from the 4(S) would be highly suppressed compared to the 3(S). The MC samples are only used as a cross check on backgrounds at various stages of the analysis.

The eμ mass distribution after including all selection requirements in the data sample shown in Figure A.7 overlay with background MCs while Figure A.8 shows

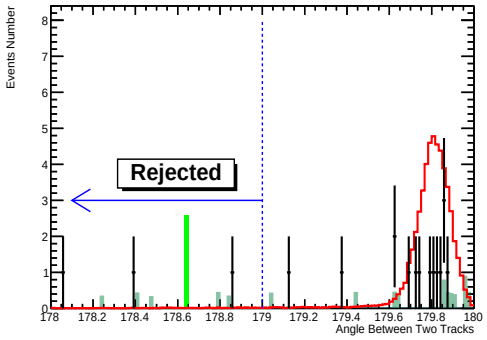

Figure A.3: The distribution of angle between 2 tracks in (N-1) cut presentation for the data sample overlay with MC backgrounds. The sea-green histogram is μ-pair production, the green histogram is τ-pair and the red histogram represents the signal MC.

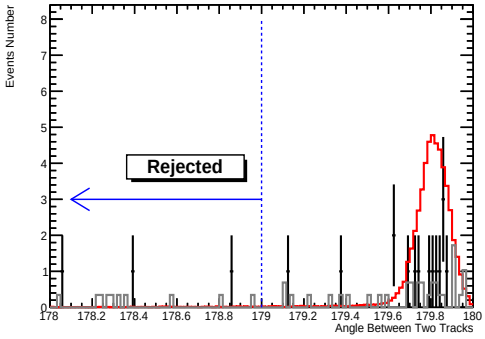

Figure A.4: The distribution of angle between 2 tracks in (N-1) cut presentation for the data sample overlay with MC backgrounds. The grey histogram is the Υ(4S)On resonance data that scaled to the data sample (histogram in black line with error bars), and the red histogram represents the signal MC.

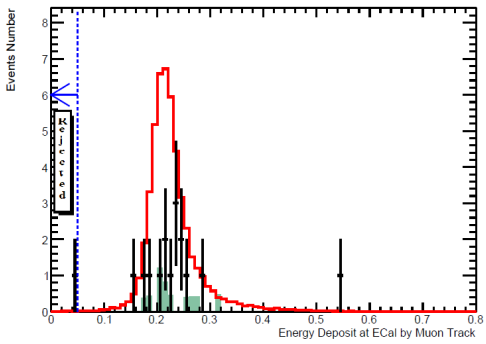

Figure A.5: Distribution of energy deposited at EMC by the muon track in the luminosity of data sample. The broken blue line indicates that selection criteria is applied at 50 MeV in the x-axis. The sea-green histogram is μ-pair production, and the red histogram represents the signal MC.

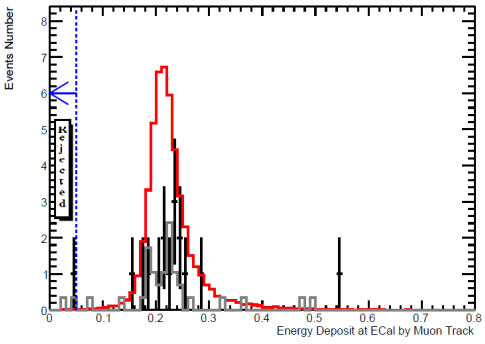

Figure A.6: Distribution of energy deposited at EMC by the muon track in the luminosity of data sample. The grey histogram is the Υ(4S)On resonance data that scaled to the data sample (histogram in black line with error bars), and the red histogram represents the signal MC.

same data sample overlay with backgrounds estimated from R6 data.

No events from Bhabha, τ-pairs, $c\bar{c}$ and uds MC sample passed the selection. The number of the Bhabha MC generated events is much lower than the data because the MC is not expected accurately to describe data. The remaining contribution in MC-determined background only arises from μ-pair events, which are kinematically very similar to the signal events so further kinematic discrimination between signal and background processes is not considered.

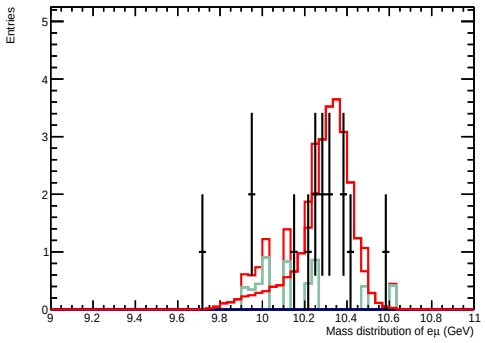

Figure A.7: Mass distribution of $e^{\pm}\mu^{\mp}$ after all selection criteria are applied in data sample. The sea-green histogram is μ-pair production, and the red histogram represents the signal MC.

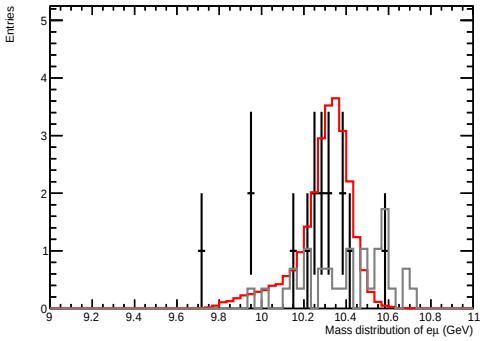

Figure A.8: Mass distribution of $e^{\pm}\mu^{\mp}$ after all selection criteria are applied in data sample. The grey histogram is the Υ(4S)On resonance data that scaled to data sample (histogram in black line with error bars), and the red histogram represents the signal MC.

The total number of generated events, the pre-selected events passing through BGFEMu and survived events passing through the user defined selections are already summerzied chapter 4 for the main simulated background MCs, Signal MC, and Data sample. Systematic uncertainty studies remain the same for the data sample as explained in chapter 5.

A.3 Result

Using equation A.1 for the data sample we measure the uncertainty in $\mathcal{BF}$ as given in equation A.2.

$$\mathcal{BF} = \frac{N_{Candidate} - N_{BG}}{\varepsilon_{SIG} \times N_{\Upsilon(3S)}} \tag{A.1}$$

$$\mathcal{BF}(\Upsilon(3S) \to e^{\pm}\mu^{\mp} = 1.0 \pm 1.4(\text{STAT}) \pm 0.8(\text{SYST})) \times 10^{-7} \tag{A.2}$$

Note that We are following the convention of quoting the statistical uncertainty as the error on the $N_{Candidate} = 15$ and including the uncertainty on the background in the systematic error as mentioned in A.2. This is consistent with no signal and we set an upper limits (UL) at 90% confidence level (CL) on $\mathcal{BF}$ by using the frequentist method developed by Roger Barlow [83] and using the CLs method [84]. Prior to unblinding it was decided to quote the limit from the CLs method as our final result as it is designed to handle large downward fluctuations in backgrounds. Table A.1 shows the calculated UL for data sample. These results represented here are the first reported experimental upper limits on $\Upsilon(3S) \to e^{\pm}\mu^{\mp}$.

Table A.1: Summary results of $\mathcal{BF}$ of ($\Upsilon(3S) \to e^{\pm}\mu^{\mp}$) mode. Displayed are the 90% confidence level upper limits in 3 % blinded sample and Data sample from this analysis.

Measurements	**Observed** Upper Limits	**Expected** Upper limits
($\Upsilon(3S) \to e^{\pm}\mu^{\mp}$) (3% unblinded sample) Barlow method	$< 3.7 \times 10^{-6}$	$< 2.7 \times 10^{-7}$
($\Upsilon(3S) \to e^{\pm}\mu^{\mp}$) (3%unblinded sample) CLs method	$< 3.0 \times 10^{-6}$	$< 2.2 \times 10^{-6}$
($\Upsilon(3S) \to e^{\pm}\mu^{\mp}$) (Data sample) Barlow method	$< 3.6 \times 10^{-7}$	$< 2.3 \times 10^{-7}$
($\Upsilon(3S) \to e^{\pm}\mu^{\mp}$) (Data sample) CLs method	$< 3.6 \times 10^{-7}$	$< 2.8 \times 10^{-7}$

A.4 Conclusion

Following submission of this dissertation for examination, the BaBar Collaboration approved the unblinding of this analysis and the results of that unblinding are included in the Appendix A. The fully unblinded result using the full 27.02 fb^{-1} is: $\mathcal{BF}(\Upsilon(3S) \to e^{\pm}\mu^{\mp} = 1.0 \pm 1.4(\text{STAT}) \pm 0.8(\text{SYST})) \times 10^{-7}$. This is consistent with zero and we set a 90 % CL upper limit of $\mathcal{BF}(\Upsilon(3S) \to e^{\pm}\mu^{\mp}) < 3.6 \times 10^{-7}$.

Bibliography

[1] Y. Fukudae et al.(Super-Kamiokande Collaboration), Evidence for Oscillation of Atmospheric Neutrinos, Phys. Rev. Lett. 81 (8) 1562-1567, 1998.

[2] Q. R. Ahmad et al. (SNO Collaboration), Measurement of the Rate of $\nu_e + \mathrm{d} \rightarrow \mathrm{p} + \mathrm{p} + \mathrm{e}^-$ Interactions Produced by ^{8}B Solar Neutrinos at the Sudbury Neutrino Observatory. Phys. Rev. Lett. 87 (7) 2001.

[3] W. Love et al. (CLEO Collaboration), Search for Lepton Flavor Violation in Upsilon Decays,Phys. Rev. Lett. 101, 201601, 2008.

[4] B. Aubert et al. (BABAR Collaboration), Search for the Lepton-Flavor Violating Decays,BABAR-CONF-08/020,2008.

[5] M. N. Achasov, K. I. Beloborodov, A.V. Bergyugin et al., Phys. Rev. D 81, 057102 (2010), (SND Collaboration).

[6] Ablikim. M.et al. 13L PRD 87 112007 (BES III Collaboration).

[7] G. Aad et al. Phys. Rev. D 90, 072010 (2014).

[8] M. Gell-Mann, "A Schematic Model of Baryons and Mesons." Physics Letters. 8 (3): 214-215, (1964)

[9] G.Aad et al. (ATLAS Collaboration), Observation of a new particle in the search for the Standard Model Higgs boson with the ATLAS detector at the LHC, Phys.Lett. B 716 (2012) 1-29.

[10] S. Chatrchyan et al. (CMS Collaboration), Observation of a new boson at a mass of 125 GeV with the CMS experiment at the LHC, Phys. Lett. B 716 (2012) 30.

[11] CERN, the European Organization for Nuclear Research, http://home.cern.

[12] D. Griffith, Introduction to Elementary Particles, WILEY-VCH Verlag GmbH and Co. KGaA, 2004.

[13] B. Aharmim et al. (SNO Coll.), Phys. Rev. C 72, 055502 (2005).

[14] N. Arkani-Hamed, A. G. Cohen, E. Katz, and A. E. Nelson. The littlest Higgs. JHEP, 07:034, 2002, hep-ph/0206021.

[15] Anna Rossi. Supersymmetric seesaw without singlet neutrinos: Neutrino masses and lepton-flavour violation. Phys. Rev., D66:075003, 2002, hep-ph/0207006.

[16] K. S. Babu and Christopher Kolda. Higgs-mediated $\tau \rightarrow 3\mu$ in the supersymmetric seesaw model. Phys. Rev. Lett., 89:241802, 2002, hep-ph/0206310.

[17] J. Pati and A. Salam, Phys. Rev. D10 (1974), 275.

[18] F. Halzen and Alan D. Martin, Quarks and Leptons: An Introductory Course in Modern Particle Physics, JOHN WILEY and SONS,1984.

[19] W. N. Cottinghm and D. A. Greenwood, An Introduction to the Standard Model of Particle Physics, Cambridge University Press, 1998.

[20] Donald H. Perkins, Introduction to High Energy Physics, Cambridge, 2000.

[21] C. Patrignani et al. (Particle Data Group),Review of Particle Physics, Chin. Phys. C, 40, 100001 (2016)

[22] S. L. Glashow, Partial-symmetries of weak interactions, Nuclear Physics, Volume 22:579-588,1961.

[23] S. Weinberg et al. Phys.Rev.Lett.19:1264-1266,1967.

[24] A. Salam, Elementary Particle Theory (Nobel Symp. No. 8), ed. N. Svartholm, Stockholm, 1968.

[25] W. Jonathan, "Neutrino 'flip' wins physics Nobel Prize". BBC News. Retrieved 6 October 2015.

[26] NASA Science, "Dark Energy, Dark Matter", NASA Science: Astrophysics. 5 June 2015.

[27] R. Essig, P. Schuster, and N. Toro Phys. Rev. D 80, 015003 2009.

[28] L. Accardo et al. (AMS Collaboration) Phys. Rev. Lett. 113 121101 2014.

[29] J. P. Lees et al.(BABAR Collaboration),Search for a dark photon in e^+e^- collisions at BABAR, Phys. Rev. Lett. 113 201801 (2014).

[30] J. P. Lees et al.(BABAR Collaboration), Search for invisible decays of a dark photon produced in e^+e^- collisions at BABAR, arXiv:1702.03327.

[31] J. P. Lees et al.(BABAR Collaboration), Search for a muonic dark force at BABAR, Phys. Rev. D 94 011102 (2016).

[32] J. P. Lees et al.(BABAR Collaboration), Search for Low-Mass Dark-Sector Higgs Bosons, Phys. Rev. Lett. 108 211801 (2012).

[33] D. Griffiths, Introduction to Elementary Particles. New York: John Wiley and Sons (1987).

[34] W.-M. Yao et al. (Particle Data Group), J. Phys. G 33, 1 (2006).

[35] Bellgardt, U. et al., Nucl.Phys. B 299 , 1-6 SIN-PR-87-09 (1988).

[36] G. Abbiendi et al., Eur.Phys.J. C16 (2000) 185-210, 49 pp.

[37] S. Nussinov, R. D. Peccei, and X. M. Zhang, Phys. Rev. D 63, 016003 (2000).

[38] Thomas Gutsche, Juan C. Helo, Sergey Kovalenko, and Valery E. Lyubovitskij, Physical Review D, 83, 115015 (2011).

[39] C. Patrignani et al. (Particle Data Group), Chin. Phys. C, 40, 100001 (2016)

[40] B. Aubert et al., The BABAR detector, Nucl. Instrum. Meth., A 479:1116, 2002.

[41] PEP-II,An Asymmetric B Factory. Conceptual Design Report, SLAC-418, LBL-PUB-5379, 1993.

[42] BABAR Collaboration, BABAR detector image gallery, (1999), avaliable at http://www.slac.stanford.edu/BFROOT/www/Detector/Images/Images.html.

[43] T. Bohringer et al. Observation of Υ, $\Upsilon\prime$ and $\Upsilon\prime\prime$ at the Cornell Electron Storage Ring, Physical Review Letters 44 (17): 1111 (1980). (CUSB Collaboration)

[44] BABAR Collaboration, Accelerator and detector performance data, (2009), avaliable at http://www-public.slac.stanford.edu/babar/perfdata.html.

[45] J. P. Lees et al.(BABAR Collaboration), Time-Integrated Luminosity Recorded by the BABAR Detector at the PEP-II e^+e^- Collider, Nucl. Instrum. Meth, A 726:203-213, 2013.

[46] S. Banerjee, B. Pietrzyk, J. M. Roney and Z. Was,Tau and muon pair production cross sections in electron-positron annihilations at $\sqrt{s} = 10.58\ GeV$, Phys. Rev. D77, 054012(2008).

[47] Quinn, H. et al. (BABAR Collaboration), The BABAR Physics Book,SLAC Report: SLAC-R-504 (2010).

[48] The BABAR Detector, SLAC National Accelerator Laboratory, available at https://www.slac.stanford.edu/BFROOT/www/doc/workbook/detector/detector.html.

[49] B. Aubert et al. (BABAR Collaboration), The BABAR Detector, Nucl. Instr. Meth. A479, 1 (2002).

[50] C. Bozzi et al. The BABAR silicon vertex tracker. Nucl. Instrum. Meth., A435:2533, 1999.

[51] B. Aubert et al. (BABAR Collaboration), Technical Design Report, SLAC-REP-372 (1995).

[52] K. E. Alwyn, Tau lepton studies at BABAR (a PhD thesis), Manchester University (2009).

[53] P. Coyle et al., Particle Identification Methods in High Energy Physics, Nucl. Instr. Methods A343, 292 (1994).

[54] Brian R. Martin, Nuclear and Particle Physics (an Introduction), John Wiley & Sons Ltd. (p128, p130), 2006.

[55] U. Amaldi, Fluctuations in Calorimetry Measurements, Physica Scripta 23, 409-423, 1981.

[56] H. Ahmed, In Situ Light Jet Energy Calibration Using Semileptonic Top Quark Decay with the ATLAS Experiment (a PhD thesis), University of Alberta Library, p39, 2009.

[57] R.J. Barlow et al., Nucl. Instr. Methods A420 (1999) 162.

[58] F. Anulli et al., The muon and neutral hadron detector for BABAR, Nucl. Instrum. Meth., A409:542546, 1998.

[59] W. Menges et al., The BABAR muon system upgrade, IEEE Nucl. Sci. Symp. Conf. Rec., 5:14701474, 2006.

[60] M. Andreotti, et al. (BABAR LST Group), A Barrel IFR with Limited Streamer Tubes, BABAR Internal Report, unpublished, 2003.

[61] The BABAR Detector: Upgrades, Operation and Performance, NIM A 729 615-701, 2013.

[62] Joshua R Klein and Aaron Roodman, Blind analysis in nuclear and particle physics,Annual Review of Nuclear and Particle Science, 55(1):141-163, 2005.

[63] S. Agostinelli et al., Geant4 - a simulation toolkit, Nucl. Instr. Methods A506, 250-303 (2003).

[64] R. Brun and F. Rademakers, ROOT: An object oriented data analysis framework, Nucl. Instrum. Meth. A A389, 81 - 86 (1997).

[65] BABAR collaboration, Long Term Data Analysis, available at: https://bbr-wiki.slac.stanford.edu/bbr_wiki/index.php/Long_Term_Data_Analysis.

[66] A. Bevan, B. Golob, T. Mannel, S. Prell, and B. Yabsley, et al., Physics of the B-Factories, 2013.

[67] S. Jadach, B. F. L. Ward and Z. Was, Comput. Phys. Commun. 130, 260 (2000).

[68] S. Jadach, W. Placzek and B. F. L. Ward, Phys. Lett. B390, 298 (1997).

[69] D. J. Lange, Nucl. Instrum. Methods A462, 152 (2001).

[70] B. Aubert et al. (BABAR Collaboration), Nucl. Instrum. Methods A479, 1 (2002).

[71] S. Jadach, B. F. L. Ward, and Z. Was, Phys. Rev. D 63, 113009 (2001).

[72] Jadach S, Placzek W, and Ward B. F. L, Phys. Lett. B 390 298 (1997).

[73] D. J. Lange, Nucl. Instrum. Methods Phys. Res., Sect. A462, 152 (2001).

[74] I. Narsky, arXiv:physics/0507143v1 [physics.data-an] (2005).

[75] B. Hooberman, M. Battaglia, Y. Kolomensky, and S. Banerjee, Search for the Charged Lepton-Flavor Violating Decays $\Upsilon(nS) \to e\tau/\mu\tau$ (n = 2,3), BaBar Analysis Document 2108, Version 15 (2008).

[76] https://bbr-wiki.slac.stanford.edu/bbr_wiki/index.php/Physics/PID/PID_Selector_List

[77] Piti Ongmongkolkul et al., Particle Identification Using Error Correction Output Code Multiclass Classifier, BABAR Analysis Document 2199, Version 03

[78] Thomas G. Dietterich and Ghulum Bakiri. Solving Multiclass Learning Problems via Error Correcting Output Codes. Journal of Artificial Intelligence Research, 2:263-286, 1995.

[79] C. O. Vuosalo, A. V. Telnov, K. T. Flood, Muon Identification Using Decision Trees, BABAR Analysis Document 1853, Version 3.

[80] I. Narsky, Optimization of Signal Significance by Bagging Decision Trees, arXiv:physics 0507157.

[81] Phys. Rev. Lett. 104, 151802.(2010).

[82] http://statpages.info/confint.html#Poisson

[83] R. Barlow, ScienceDirect 149, 2 (2002), pp 97-102.

[84] A. L. Read, "Presentation of search results: The CL(s) technique", J.Phys. G28 (2002) 2693-2704.; Glen Cowan, Kyle Cranmer, Eilam Gross, Ofer Vitells, "Asymptotic formulae for likelihood-based tests of new physics," Eur.Phys.J. C71 (2011) 1554, Erratum: Eur.Phys.J. C73 (2013) 2501.